

## 2 Linac-Ring Design

**Author list:** I. Ben-Zvi, S. Berg, M. Blaskiewicz, S. Brooks, A. Fedotov, Y. Hao, A. Hershkovich, H. Huang, Y. Jing, V.N. Litvinenko, C. Liu, Y. Luo, W. Meng, M. Minty, F. Meot, B. Parker, V. Ptitsyn, V. Ranjbar, T. Roser, J. Skaritka, O. Tchoubar, P. Thieberger, D. Trbojevic, N. Tsoupas, J. Tuozzolo, E. Wang, G. Wang, H. Witte, Q. Wu, C. Xu, W. Xu, A. Zaltsman

**Acknowledgments to:** E. Aschenauer, K. Brown, C. Brutus, W. Fischer, D. Gassner, H. Hahn, W. Jackson, A. Kisilev, R. Lambiase, G. Mahler, B. Martin, G. McIntyre, R. Michnoff, K. Mirabella, T. Miller, C. Montag, R. Palmer, S. Peggs, R. Petty, I. Pinayev, T. Rao, J. Sandberg, K. Smith, S. Tepikian, R. Than

### 2.1 The Linac-Ring Design Concept

#### 2.1.1 Accelerator Concept, Layout and Major Components

The Linac-Ring accelerator design of the electron-hadron collider has been developed fully satisfying the eRHIC physics goals. As described in Chapter 1 two stages of the LR design have been considered: the Nominal design with the luminosity reaching  $\sim 1 \times 10^{33} \text{ cm}^{-2} \text{ s}^{-1}$  and the Ultimate design that pushes the luminosity to  $10^{34} \text{ cm}^{-2} \text{ s}^{-1}$  level.

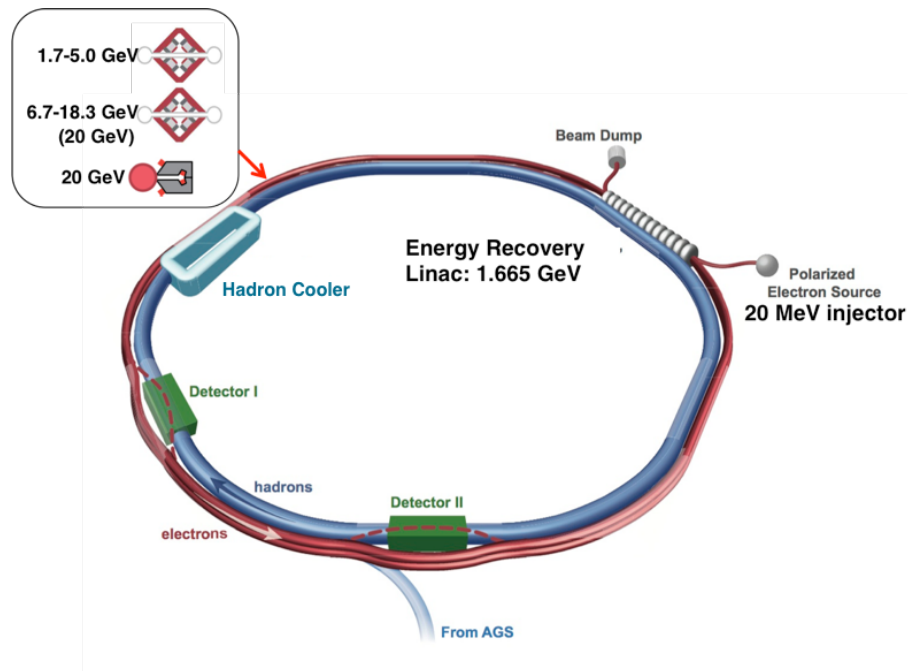


**Figure 2-1:** The layout of the eRHIC collider.

The key goal of the eRHIC accelerator design has been to achieve the required high-energy, high-luminosity performance at a realizable machine construction cost. For the hadron part of the machine, eRHIC takes advantage of the existing RHIC accelerator complex, including the full suite of injector systems for polarized protons and fully-stripped heavy ions. The new electron

accelerator is achieved through a cost-effective design, taking advantage of significant recent advances in accelerator technology.

As shown in Figure 2-1, the LR eRHIC design uses one of the RHIC hadron beams (the clockwise-moving “blue” beam), with a high energy electron beam counter-rotating in the same tunnel, and collisions occurring in two intersection regions occupying the present experimental areas of the STAR (IR6) and PHENIX (IR8) detectors. The full range of RHIC hadron beams is thus available for eRHIC, up to 250 GeV for polarized protons and 100 GeV/u for Au ions.

The accelerated electrons originate in a new, high-current polarized source and are accelerated to 20 MeV for injection into a 1.665 GeV Energy Recovery Linac (ERL). Using recirculating rings inside the RHIC tunnel the electrons make multiple passes through the ERL, gaining 1.665 GeV of energy with each pass. The electrons can be extracted at any energy above 3.3 GeV into a high energy transport beamline which brings them into collision with the hadron beam at either IR6 or IR8. The spent electron bunch is then recirculated back through the ERL, returning its energy to the superconducting RF structure of the linac, after which the decelerated electrons are dumped. Thus, each electron bunch participates in only one collision crossing with the hadron beam, and the process repeats itself for each succeeding bunch. The electron bunches are accelerated and brought into collision with the hadron beam at a frequency of 9.4 MHz. As described below, the luminosity goals are achieved with an electron beam current of 26 mA (Nominal design) or 50 mA (Ultimate design) and tightly focused (small emittance) beams for both the hadrons and electrons.

The major eRHIC accelerator components are:

- The 20 MeV injection complex, located at the IR2 area of the RHIC tunnel. It includes a high-current polarized beam injector and 20 MeV linear accelerator. A beam dump for disposing of the decelerated beam is also located in this area.
- The 1.665 GeV Energy Recovery Linac (ERL) is located along the IR2 straight section. The ERL is 185 m long and consists of a string of superconducting 647 MHz cavities. The use of energy recovery technology in the main accelerator linac is essential to reach a high value (50mA) of the electron average current. To compensate for synchrotron radiation losses two alternative schemes are being considered. One of them employs additional RF cavities (1.3 GHz) to replenish the beam energy loss, while the second scheme uses main linac cavities for this purpose.
- Two vertically stacked recirculation beamlines run around the RHIC tunnel circumference, outside of the hadron ring. The optics of each of the beamlines is based on a Fixed Field Alternating Gradient (FFAG) lattice, which is capable of transporting beams of different energies within a common vacuum chamber. The first FFAG beamline transports electrons with energies from 1.7 GeV to 5.0 GeV. The second FFAG beamline is used to pass beams in the 6.7-20 GeV range. The magnetic structure of both beamlines is based on permanent magnets. The main idea behind using the FFAG lattice approach and the permanent magnet technology is to lower machine construction and operation costs.
- A spreader and a combiner are placed either side of the ERL for proper distribution and matching of the electron beams of different energies between the ERL and FFAG beamlines. Both the spreader and the combiner have 12 arms used to transport beams of particular energies. The arms also are used for optics matching and path length correction (to make one turn transport completely isochronous and achromatic). 12 arms are required for acceleration to 20 GeV. For acceleration up to 10 GeV only 6 arms are used.
- A cooling device in the IR10 region of the RHIC tunnel achieves cooling of the proton and ion beams. In the Ultimate design the device will employ the Coherent Electron Cooling technique

for efficient cooling in longitudinal and transverse planes. In the Nominal design the possibility of electron cooling is being considered.

- The electron-hadron collisions occur in two interaction regions (IR6 and IR8 RHIC areas). In the spreader area electrons are extracted from the FFAG beamline into a high energy electron transport beam line which runs around of the circumference of the RHIC tunnel and delivers electron beam to the experimental detector(s). The interaction regions include superconducting magnets and provide strong focusing to achieve the  $\beta^*=5$  cm for both beams. The electron and hadron beams are brought into the collision with a 10 mrad crossing angle. Crab cavities are employed to prevent loss of luminosity due to the crossing angle.

The present RHIC accelerator uses superconducting magnets to circulate hadron beams in two rings of 3834 m circumference. The wide energy reach of RHIC provides a natural opportunity to operate eRHIC over a wide range of center-of-mass collision energies. Existing proven accelerator technologies, exploited in RHIC and its injectors to produce and preserve proton beam polarization, will provide the highly polarized proton beam required for the eRHIC experiments. Modifications of the present RHIC machine for the eRHIC era include new quadrupole and dipole magnets in two interaction regions with experimental detectors and additional Siberian Snakes for acceleration of polarized  $^3\text{He}^{+2}$ . Also, a cooling device will be added with the purpose of producing small transverse and longitudinal beam emittances.

### 2.1.2 Design Beam Parameters and Luminosities

Based on the fact that electrons, accelerated by the linear accelerator, collide with the protons (or ions) accelerated and stored in the circular machine, the eRHIC collision scheme is called the “linac-ring” scheme. This scheme has been chosen for eRHIC because of several clear advantages it brings in luminosity and electron polarization. On the luminosity side the “linac-ring” scheme overcomes one of the fundamental luminosity limitations of the “ring-ring” scheme from circulating electron beam quality deterioration caused by many repeating beam-beam interactions. Unlike the electron beam circulating in a storage ring, the electron beam from a linac passes through the collision point(s) only once. Hence, a beam-beam interaction of much higher strength can be allowed, paving the way to higher luminosity. The luminosity of the “linac-ring” scheme can be written as a function of the hadron beam parameters:

$$L = f_c \xi_h \frac{\gamma_h}{\beta_h^*} \frac{ZN_h}{r_h} H_{hg} H_p ,$$

where  $r_h = Z^2 e^2 / Mc^2$  is the hadron classical radius,  $\xi_h$  is the hadron beam-beam parameter,  $\beta_h^*$  is the hadron beta-function at the interaction point,  $N_h$  is the hadron bunch intensity,  $\gamma_h$  is the hadron relativistic factor and  $Z$  is the hadron charge.  $f_c$  is the collision frequency, which is the same as the bunch repetition rate.

The geometric loss factor  $H_{hg}$  arises from luminosity loss due to the hour-glass effect and the crossing angle. With a 10 mrad crossing angle at the eRHIC collision points, the crab-crossing technique has to be employed to prevent luminosity loss.

The  $H_p$  parameter represents the luminosity enhancement resulting from the pinching of the electron beam size at the collision point caused by the hadron beam focusing force.

The design luminosity and choice of beam parameters are influenced by both physical limits and practical considerations. Some of these limitations, such as the maximum limits for the hadron beam-beam and space-charge parameters for hadrons come from operational and experimental observations at RHIC or other hadron colliders. Others, like the choice of  $\beta^*$  or the polarized electron beam current, are defined by the limits of accelerator technology. Considerations of the operational cost of the machine limit the electron beam power loss caused by synchrotron radiation.

The major limits assumed for the beam and accelerator parameters are:

- Polarized electron average current:  $I_e \leq 50$  mA
- Hadron space-charge tune shift:  $\Delta Q_{sp} \leq 0.06$  (with space charge compensation for the Ultimate design)
- Hadron beam-beam parameter:  $\xi_h \leq 0.015$
- Electron synchrotron radiation power:  $P_{SR} < 2.5$  MW

Table 2-1 and Table 2-2 list the beam parameters and design luminosities. The listed values of peak luminosity assume the following H-factors:  $H_{hg}=0.84$  and  $H_p=1.26$ .

**Table 2-1:** Beam parameters for highest luminosity of e-p collisions for LR designs.

	LR Nominal design		LR Ultimate design	
	e	p	e	p
Energy [GeV]	10	250	8.3	250
CM energy [GeV]	100		91	
Bunch frequency [MHz]	9.4		9.4	
Bunch intensity [ $10^{10}$ ]	1.7	20	3.3	30
Beam current [mA]	26	277	50	415
rms norm.emittance h/v[ $\mu$ m]	36.7/36.7	0.5/0.5	16.5/16.5	0.27/0.27
rms emittance h/v [nm]	1.9/1.9	1.9/1.9	1.0/1.0	1.0/1.0
beta*, h/v [cm]	12.5/12.5	12.5/12.5	7/7	7/7
IP rms beam size h/v [ $\mu$ m]	15.3/15.3		8.4/8.4	
IP rms ang. spread h/v [ $\mu$ rad]	120/120	120/120	120/120	120/120
max beam-beam parameter	1.2	0.004	4.1	0.015
e-beam disruption parameter	20		36	
max space charge parameter	1.4e-4	0.006	8.6e-4	0.058
rms bunch length [cm]	0.3	16.5	0.3	5
Polarization [%]	80	70	80	70
Peak luminosity [ $10^{33}$ cm <sup>-2</sup> s <sup>-1</sup> ]	1.0		14.4	

**Table 2-2:** Beam parameters for highest luminosity of e-Au collisions for LR designs.

	LR Nominal design		LR Ultimate design	
	e	Au	e	Au
Energy [GeV]	10	100	8.3	100
CM energy [GeV]	63		58	
Bunch frequency [MHz]	9.4		9.4	
Bunch intensity [ $10^{10}$ ]	1.7	0.2	3.3	0.2
Beam current [mA]	26	219	50	219
rms norm.emittance h/v[ $\mu$ m]	29/29	0.16/0.16	24/24	0.16/0.16
rms emittance h/v [nm]	1.5/1.5	1.5/1.5	1.5/1.5	1.5/1.5
beta*, h/v [cm]	12.5/12.5	12.5/12.5	7/7	7/7
IP rms beam size h/v [ $\mu$ m]	13.6/13.6		10.2/10.2	
IP rms ang. spread h/v [ $\mu$ rad]	109/109	109/109	146/146	146/146
max beam-beam parameter	1.2	0.0053	1.5	0.01
e-beam disruption parameter	20		29	
max space charge parameter	1.5e-4	0.039	6e-4	0.058
rms bunch length [cm]	0.3	16.5	0.3	11



Polarization [%]	80	0	80	0
Peak luminosity [ $10^{33} \text{cm}^{-2} \text{s}^{-1}$ ]	2.5		8.0	

The eRHIC bunch frequency is 9.4 MHz is equal to the bunch frequency of the present RHIC hadron beam. This choice of bunch frequency not only allows us to avoid modifications of the RHIC injection system but also suits eRHIC detector requirements.

The eRHIC accelerator design employs transverse and longitudinal cooling of hadron beams. The transverse cooling helps to reach the high peak luminosity by reducing the transverse beam size and is essential for achieving the small angular spread at the interaction points, which is required for efficient detection of collision products propagating at small angles to the hadron beam. The longitudinal cooling shrinks the bunch length to the scale of  $\beta^*$  in order to maximize the  $H_{hg}$  factor. Also, the crab-crossing system benefits from the shorter hadron bunch length in terms of the required voltage and, hence, the cost of the system. Both transverse and longitudinal cooling will be used to counteract beam emittance growth and related particle losses produced by intra-beam scattering, extending the luminosity lifetime and maximizing the average luminosity. Normally the cooling process will be activated during the store, after the hadron beam has been accelerated. In addition, the hadrons may be pre-cooled at the injection (down to the space charge limit), since smaller transverse emittances would improve the polarization preservation through the acceleration ramp.

The eRHIC hadron bunch intensity in Nominal design is similar to that used in RHIC operation (up to  $N_h = 2 \cdot 10^{11}$  for protons). At a given bunch intensity the eRHIC hadron bunch is much denser than the RHIC bunch due to cooling. For Ultimate design the strong cooling will be implemented and the proton intensity will be increased to at least  $3 \cdot 10^{11}$  protons per bunch, thus improving the luminosity by one order of magnitude, exceeding  $10^{34} \text{cm}^{-2} \text{s}^{-1}$ .

## 2.2 Electron Accelerator

### 2.2.1 Electron Injector and Dump

#### *High current polarized electron gun*

eRHIC will require a highly polarized electron source with high average current, short bunch length and low emittance. The current state-of-the-art polarized electron sources deliver either a high peak current, low average current beam such as the case at SLAC ( $>5\text{A}$ ) or a high average current, low peak current beam as produced at JLab (4 mA). eRHIC will require a very high average current (up to 50 mA) with a bunch charge up to 5.3 nC, with low emittance and a long cathode lifetime.

GaAs was selected as a photocathode because it is well established and widely used as a source of polarized electrons. The current state of the art single GaAs based electron sources cannot deliver the required 50 mA current due to ion back-bombardment and surface heating induced by very high laser power. Therefore, a novel approach to the design of the eRHIC electron source is required. To achieve the high beam current, two R&D projects are carrying out in both MIT-bates and BNL.

In the MIT-bates source design, a single large area cathode is used in the gun. The new feature of the installation is annular shape of the beam. A ring-shaped laser beam will be formed with an axicon lens and focused on the cathode surface. The laser will not illuminate the central area of the cathode, where the most of the damage is concentrated. The active cathode cooling will be implemented using Fluorinert as a cooling agent. This liquid has virtually zero conductivity and very good electrical strength. The working voltage of the cathode is 120 kV while the cathode gradient is 0.8 MV/m. With better design of the cathode and anode geometry, the gradient on the

cathode could be higher such as 2MV/m. A polished field shield to prevent a field emission surrounds the cathode assembly. The anode is disconnected from the ground potential and could be biased to 1 kV in order to reflect the ions produced outside the cathode-anode gap and trapped in the electron beam. With the concept of eliminating the ion back and keeping the cathode temperature below 50 C, the cathode lifetime will only depends on the residual gas poisoning. Thus, the cathode in the gun maybe capable to operate with very long lifetime. The large cathode area also helps to run the beam at high average current, possible to 26mA.

In order to run the eRHIC-required beam, the DC gun geometry should be optimized and charged to higher voltage such as 200kV. The gradient on the cathode should be above 2MV/m. The annular beam laser shaping also need investigate. Large cathode fast exchange mechanism needs to investigate as well.

In order to run the eRHIC-required beam, the DC gun geometry should be optimized and charged to higher voltage such as 200kV. The gradient on the cathode should be above 2MV/m. The annular beam laser shaping also need investigate. Large cathode fast exchange mechanism needs to investigate as well.

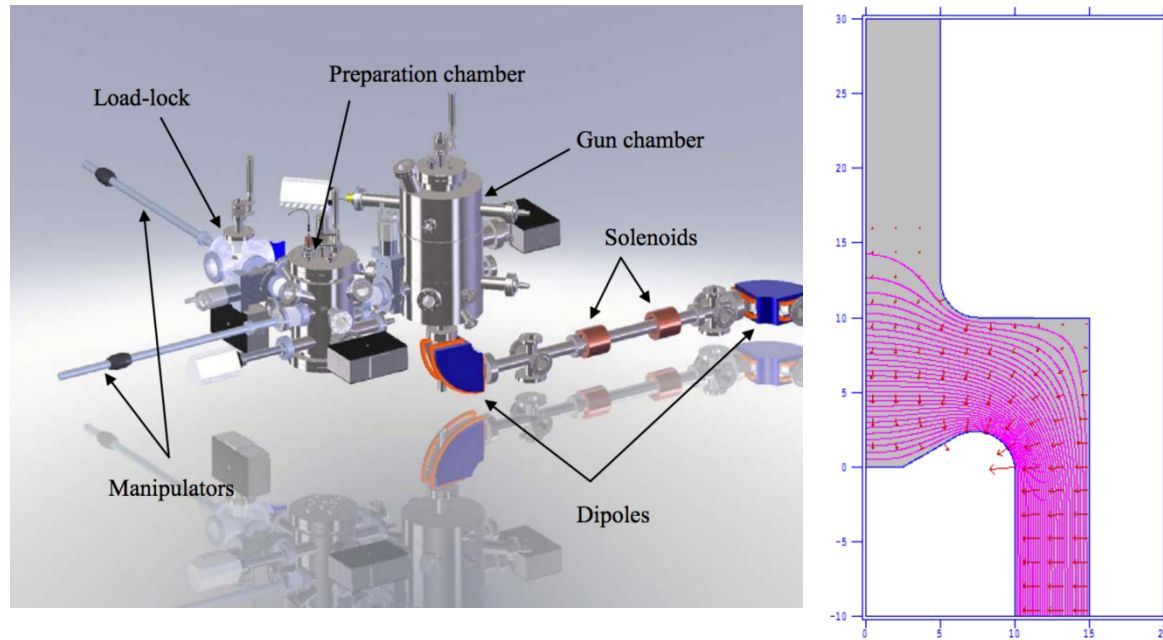


**Figure 2-2:** Left plot: MIT-bates gun and beamline design. Right plot: DC gun geometry and electric field simulated by Superfish.

In BNL concept, assuming each cathode can run 2.5 mA average current with long lifetime, combining the beams from 20 individual cathodes could achieve 50 mA beam.

A conceptual layout of the Gatling gun is shown in Figure 2-3. Twenty lasers deliver sequenced beam pulses to a circular array of photo cathodes. The cathodes are located on the surface of a cathode shroud charged to 220 kV. The repetition frequency of a single cathode is 450 kHz, due to the multiplexing of 20 cathodes producing electron pulses with bunch lengths of 1.5 ns. Solenoids placed within the anode provide focusing. A series of fixed dipole magnets first bend the off-axis electron bunches toward the gun's center axis. Then the bunches are kicked into alignment with the gun's center axis by the rotating magnetic field of the combiner magnet that bends the electron bunches of all the cathodes onto a common axis. The repetition frequency of the funneled bunches is 9.4 MHz for the total average current reaches~ 50 mA. The cathode also has a cooling channel; capable to maintain the cathode is room temperature with high power laser illumination. Compare to MIT-bates scheme, BNL using large emission area to slow down the cathode degrade

from ion back bombardment, while MIT direct avoid laser shining on the ion back bombardment activate area.

BNL has establish collaborations with institutions having extensive experience in the development of polarized electron beams from single photo cathode guns, The e-RHIC polarized source development program shall evaluate different gun designs and configurations and work with collaborating institutions to evaluate performance parameters from the different available e-gun designs, Maximum beam current, bunch charge, charge lifetime and charge intensity, bunch length polarization, vacuum sensitivity and cathode damage mechanisms are being studied and evaluated for use as an e-RHIC photocathode source. It is anticipated that existing design configurations will be optimized to achieve e-RHIC parameters. The relationship between cathode quantum efficiency, vacuum level and beam current vs. laser beam intensity are well understood. One method to maximize source performance using a minimum of two guns can be to establish a conservative charge life time to achieve required beam currents. The specific gun design will be optimized to provide acceptable cathode cooling and vacuum pumping whilst eliminating field emission. In one gun as the cathode quantum efficiency is depleted, laser beam intensity will be increased to maintain constant beam current over a period of time until damage mechanisms reach thresholds that limit further stable performance. At this point a second gun of comparable design will be activated and constant beam performance established. During this period the cathode for the first gun shall be exchanged with a freshly prepared cathode. As long as charge lifetime is long enough to allow efficient cathode exchange single cathode guns may provide acceptable beam current for e-RHIC. The primary emphases of the e-RHIC source development program and collaborations shall be to establish these key performance parameters with existing e-gun designs and then to optimize these gun designs to achieve e-RHIC beam parameters. The emphases of Cathode development at BNL shall be the development and implementation of semi-automated methods to mass produce and store larger quantities of cathodes and in XHV compatible mechanisms to handle and exchange, and maintain pristine cathodes in quantities necessary to fulfil the demand of the e-RHIC source. Along with single cathode gun development, Multi-cathode development shall also continue as an avenue to develop the necessary cathode manufacturing and handling methods that will be unique to the e-RHIC source. The multi-cathode funneling gun prototype is an ideal testing mechanism to evaluate and demonstrate high quality cathode mass production methods providing a means to test up to 20 cathodes at a time. All the experience gained in past years in the development of the funneling gun is relevant and immediately applicable to advance equipment and processes development for high current single cathode guns. The multi cathode e-gun test system has been established in the physics department of Stoney Brook University. In this system diagnostics evaluate electron source performance of one or more cathodes using the e-beam funneling principle to place the beam trajectories onto a common axis. The balance of this article shall present the design, status and plans for the polarized source developmental program that will discuss cathode preparation, laser systems, e-beam funneling and beam diagnostics to demonstrate high-average-current polarized electron beams that will allow the evaluation and optimization of polarized gun designs for e-RHIC.

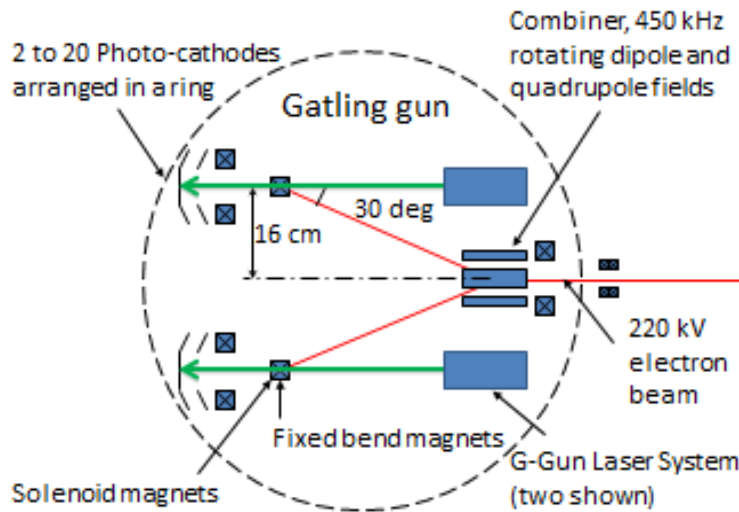


**Figure 2-3:** Gatling gun concept design.

Gatling gun vacuum chamber is very complex. It is very challenge to maintain low  $10^{-12}$  torr vacuum due to very large outgassing area. Operate the gun with stable beam and uniform bunch-to-bunch qualities such as bunch charge as well as polarization are also challenge. In such complex system with relatively small cathode, generating each cathode with 2.5mA average current beam also is a question.

#### Cathode Preparation

The high current high polarization electron gun for eRHIC requires the preparation of GaAs photocathodes. During the preparation in the preparation chamber, the photocathode is heat cleaned up to  $580^{\circ}\text{C}$  for cleaning the surface. Once the sample has cooled to room temperature, a monolayer of Cesium and Oxygen lowers the vacuum level for electrons to come out when the sample is illuminated with laser. This process is known as “Activation” and has to be performed under extreme vacuum conditions (less than  $-11$  Torr pressure). The quantum efficiency of the bulk GaAs cathodes (number of electrons produced per photon) for 650nm wavelength of laser is 8% which is acceptable and reproducible. The system is capable to go to extreme vacuum regime in a consistent basis. There is a long manipulator attached to the system for transportation of photocathode from the preparation chamber to the gun. Currently the chamber can hold two photocathode at any given time. This setup is used to perform the proof of principle experiment where only two cathodes will be used in the gun. The transfer line is vacuum isolated from the gun and from the preparation chamber with all metal valves. Each cathode preparation, from heat cooling to activation, takes approximately 4.5 hours. Superlattice GaAs, which is capable to produce highly polarized electron beam, will be used in the near future to investigate the charge lifetime during multicathode operation in the gun.

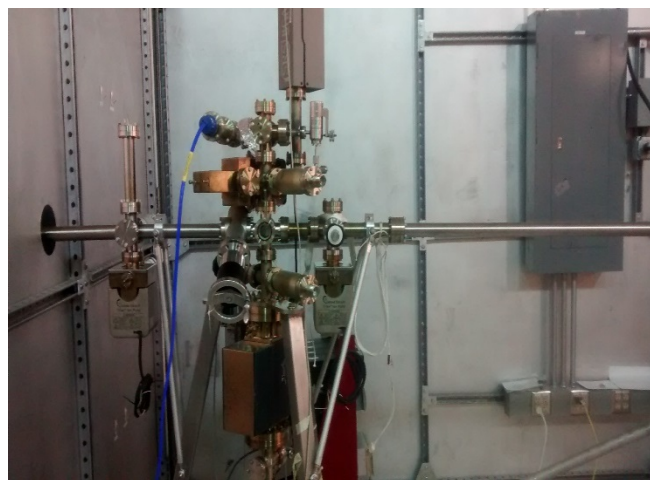
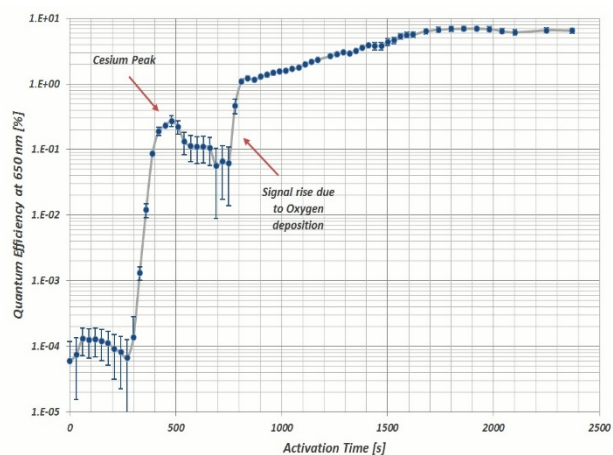
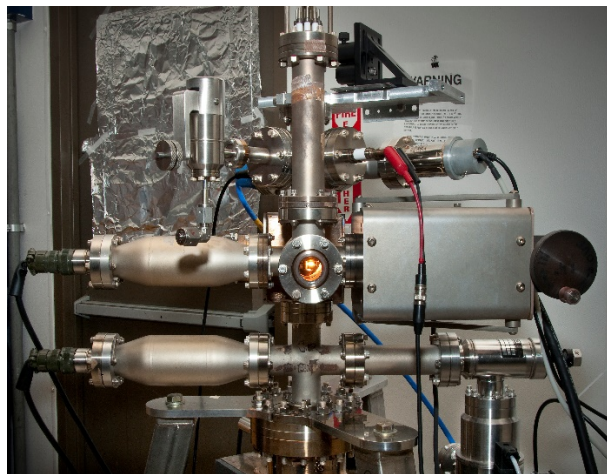


**Figure 2-4:**

In order to operate 20 cathodes in the gun, a combined preparation and storage chamber would be involved. This vessel (called the “Grand Central”) would be able to process 4 cathodes simultaneously and then subsequently store them before putting them in the gun for operation. However, automation of activation would be an important research area to be pursued. Mass activation of more than one cathode in one chamber is also to be investigated.

#### Laser for Gatling gun at BNL

At BNL, we are working to build a high average polarized current Gatling gun for eRHIC. In this Gatling gun, 20 GaAs photocathodes will be installed, and high-power lasers with reduced repetition rate will be used to drive cathodes and produce modest polarized beam current. Then, electron beam will be combined through a RF revolving combiner to achieve high average current sufficient for eRHIC application.

To produce highly polarized beam, laser pulses at 780 nm are required to drive photocathode. However, to demonstrate the Gatling principal, a cw green laser at 532 nm is chopped to generate two low repetition-rate pulses, and used to drive GaAs cathodes and produce un-polarized beam. As shown in Figure 2-5 two pulses are generated through modulation of a cw green laser at a repetition rate of 10 Hz, alternately shining on two different photocathodes. Because



the total average power is a few mill Watts and the quantum efficiency with the GaAs cathode is 1%, it is expected that micro amp beam current will be generated.

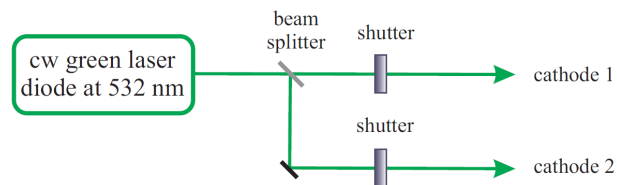


**Figure 2-5:** Two pulses are generated through modulation of a cw green laser, and alternately used to drive two cathodes.

To produce highly polarized beam, an Erbium (Er)-doped high-power fiber laser system at 1560 nm will be built and light at 780 nm will be generated through second harmonic generation (SHG). The significant advantages with the fiber laser include high-average output power, diffraction-limited beam profile, low point instability, and maintenance-free operation. In this Er-doped fiber laser, a master oscillator power amplifier is designed to produce high output. The seed is a gain-switched diode laser with 1560 nm central wavelength, 605 kHz repetition rate and 3.5 ns pulse duration, and the laser power is boosted to about 3 W through two pre-amplifier stages. In the main amplifier, a 60 W pump diode at 976 nm and 30-meter Erbium-doped photonic crystal fiber will be used to generate 20 W average output power. Through SHG, 8 W average power at 780 nm will be produced, and used to drive GaAs cathode and generate highly polarized beam. Also, it is technically feasible that 20 Er-doped lasers will be built to drive 20 cathodes, respectively, and generate up to 50 mA of polarized e-beam through the beam combiner.

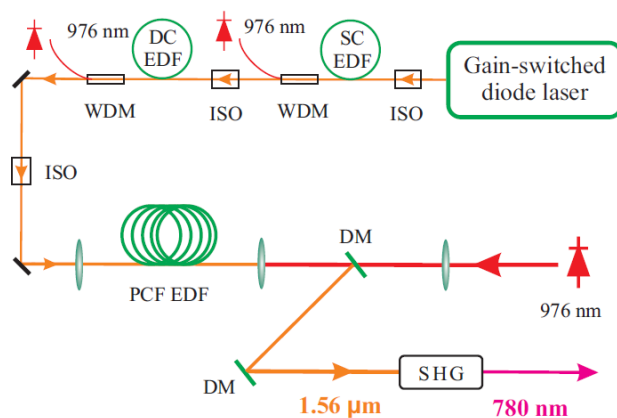


**Figure 2-6:** Er-doped fiber laser system. EDF, Er-doped fiber, SC, single-clad, DC, double-clad, PCF, photonic crystal fiber, SHG, second harmonic generation, IOS, isolator, WDM, wavelength division multiplexing, and DM, dichroic mirror.

## e- Beam Funneling

Figure 2-3 depicts the Gatling gun concept that utilizes the funneling of electron beams from twenty photo cathodes through several magnetic elements to combine into a single beam.

- Cathode Solenoid – As the electron beam leaves the cathode, it first passes through a solenoid with a fixed magnetic field. Each of the twenty solenoids are wired in series and will be powered by a single power supply windings in each solenoid provide individual trimming.
- First Bend Magnet – Following the solenoid, each beam has a fixed field bending magnet. This directs the beam radially inward into the aperture.



- **Combiner Magnet** – This magnet contains both dipole and quadrupole functions. The magnetic direction of these two functions electrically rotates to align with the direction of beam after the first bend magnet. The rotation is accomplished by individually powering ten dipole windings and ten quadrupole windings with a co sinusoidal current distribution around the magnetic direction.

#### *Low Frequency Operation*

In the initial development of the Gatling Gun, two electron beams are combined at a very low frequency of approx. 1.0 Hz. This allows operation at a greatly reduced cost. Figure 2-7 shows the combiner magnet wired for low frequency operation.

- **Cathode Selection** – The cathodes can be selectively energized using mechanical shutters.
- **Superposition of Combiner Magnet Functions** – The two rotating fields, dipole and quadrupole, as well as two non-rotating fields for horizontal and vertical correction, are all created using superposition of fields.
- Ten low frequency bipolar power supplies are used to power the ten dipole windings with superimposed values of current.

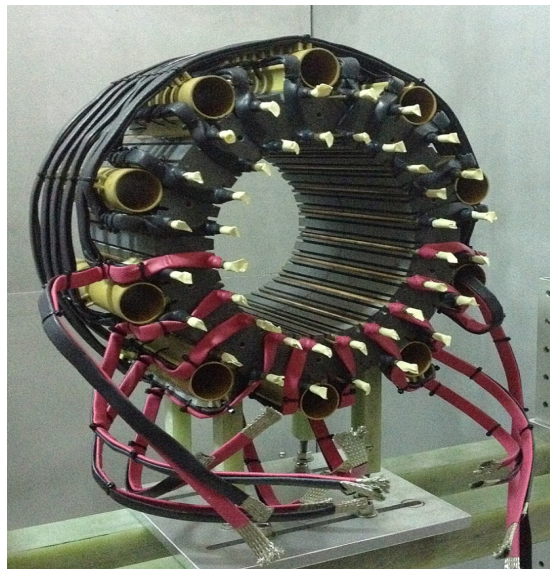


**Figure 2-7:** Combiner magnet.

#### *High Frequency Operation*

Operation for eRHIC requires electron bunches at a frequency of 9 MHz. That means that each of the ten dipole and ten quadrupole circuits will operate at  $9,000 \text{ kHz} / 20 = 450 \text{ kHz}$ . With a peak current requirement of 80 amps in the dipole circuit, the magnet cannot be driven directly.

Figure 2-8 depicts a circuit configuration for one winding pair. Each winding is connected in series with the winding directly opposite it with litz wire. In this schematic, R represents, not only the winding resistance, but also the core losses and litz wire losses. C1 and C2 form a capacitive transformer which is used both to resonate with the magnet and to impedance match the network to the coax cable which will deliver the power from the power amplifier (PA). A current transformer (CT) is used to monitor the amplitude and phase of the magnet current. This signal is

an input to a control system that regulates the current at the magnet at the required peak amplitude and maintains the phase difference from each winding pair to the next at 18 degrees.

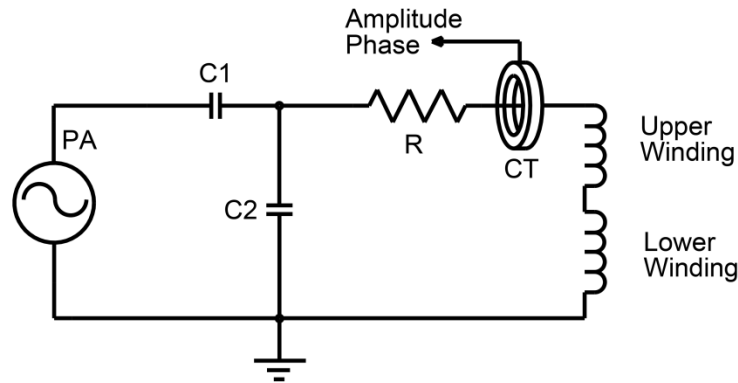


**Figure 2-8:** High frequency circuit.

#### e-Beam Source Diagnostic, and Diagnostic Development

Electron beam diagnostics to be installed in the e-beam source development facility will be used to characterize the gun performance. Beam position monitors will measure average beam positions and can be enhanced to measure bunch-to-bunch position variations. The facility can also be used for BPM pick-up prototyping and electronics testing. There is the possibility of aiding in the development and testing of the high-time resolution BPM for eRHIC. The beam profile monitors utilizing YAG screens will be used for low-power beam transverse measurements. Future developments can achieve higher resolution capabilities to measure detailed transverse beam uniformity. Methods can be tested to measure high current beam profiles. Current and charge measurements can be made using commercial integrating current transformers and fast current transformers, future developments can provide bunch-to-bunch intensity variation monitoring. Other possible measurements include absolute energy, energy spread and emittance at low energies and in the longer term, polarimeter development. The systems mentioned previously can be utilized in the beam diagnostics beam line for the MIT style polarized e-source and any other DC electron gun development here at C-AD. For example; experience gained with a multi cathode e-beam source diagnostics can also be applied to improve measurements made when characterizing the LEReC gun.

#### *20MeV polarized electrons injector*

The eRHIC electron injector has to produce up to 50 mA polarized electron beam with longitudinal and transverse beam parameters defined in Table 2-3. Figure 2-9 presents a lay out of the 20 MeV electron injector. It consists of an electron gun based on MIT-bates high current gun, 112MHz bunching cavities and a 3<sup>rd</sup> harmonic cavity, a drift space for ballistic bunch compression and a 647 MHz booster linac.

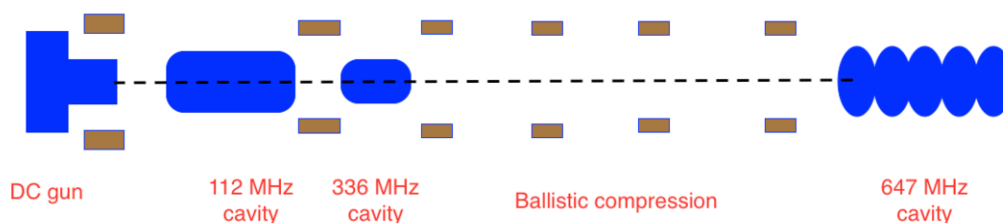


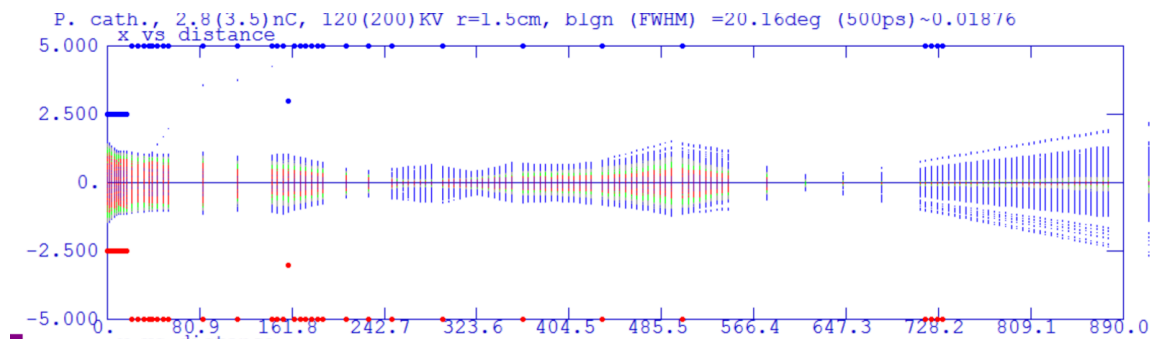
**Figure 2-9:** The layout of 20 MeV eRHIC injector beamline.

GaAs photocathode. The MIT-bates high current DC gun is adopted as the electron source for beam optics designing. The gun operates at 220kV with the 1.6MV/m cathode gradient. Long bunches are extracted from the gun to match the surface charge limitation( $<5\text{A/cm}^2$ ) and reduce the beam quality degradation due to space charge limit.

**Table 2-3:** eRHIC injector nominal design.

Parameters for Nominal design	
Energy, MeV	20
Bunch charge, nC	2.8
Bunch frequency, MHz	9.38
Average beam current, mA	26
Min normalized rms transverse emittance, $\mu\text{m}$	18
Max normalized rms transverse emittance, $\mu\text{m}$	72
rms bunch length, mm	3
rms energy spread, %	$< 1$

In nominal design, the bunch charge is 2.8 nC. The beam radius on cathode is 1.5 cm which allows to have sufficient area to generate annual beam. With a focusing solenoid at gun exit, the beam first waist is located at the center of the 112 MHz cavity. It also is used for space charge compensation. The 112 MHz SRF cavity pre-boosts the beam energy to 1.3 MeV and provides a chirp on the bunch. Then a normal conducting 3rd harmonic cavity (336 MHz) linearized the bunch longitudinal energy spread. A three meters ballistic compression drift line is applied to shorten the bunch duration to 5 mm. Multiple solenoids are placed on the beamline to maintain the beam size along the beamline. Both energy spread modification cavities are of the quarter wave resonator type. The bunch is under-compression at the entrance of the first booster cavity. The boost cavity use single 5 cell 647 MHz SRF cavity which is function as boosting the bunch energy to 20 MeV and also de-chirping the bunch reducing the energy spread to 0.1%. This cavity is same as the main linac cavities but has to deliver an RF power of 520 kW. The beam from the booster linac is then transported and injected into the main FFAG-ERL. The beam dynamics simulation of the injector beam line is done by parmela.



a) Electron beam envelop in injector

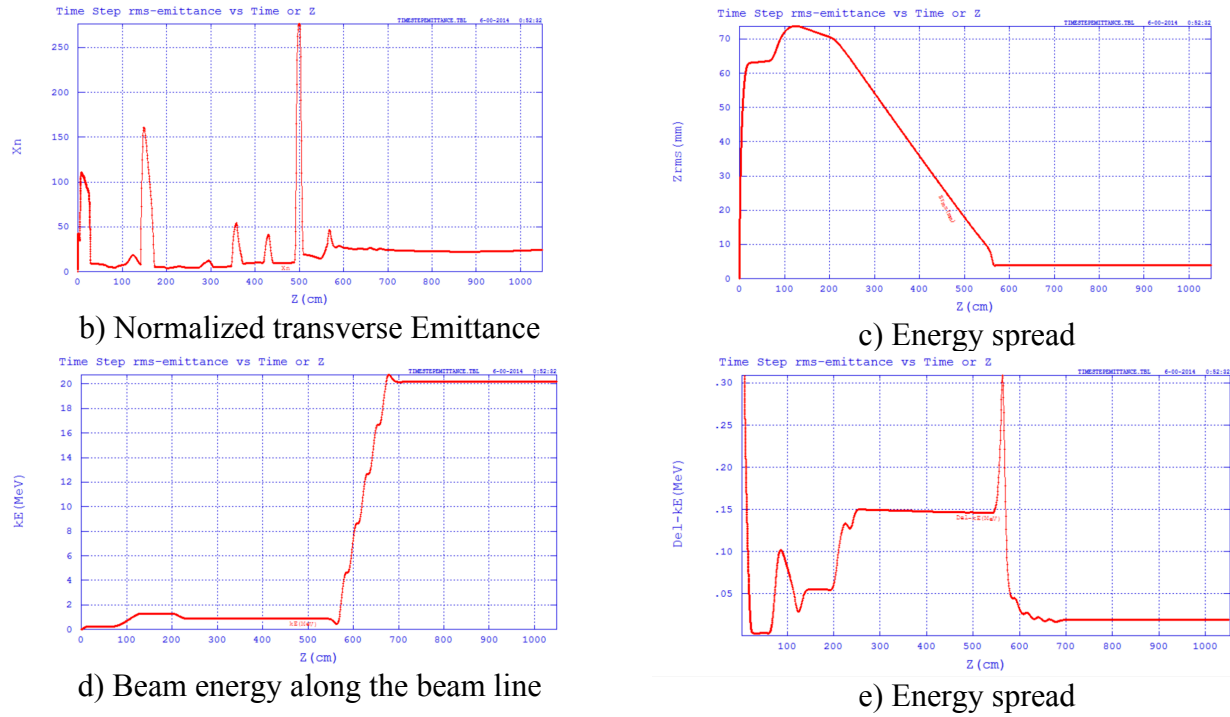


**Figure 2-10:** The eRHIC injection preliminary simulation results by Parmela.

At the exit of the injection, the following goals are achieved. The RMS transvers normalized emittance is 22.5 mm-mrad. The energy is 20 MeV. The RMS energy spread is 0.1%. More optimizations on bunch length are needed. Recent, the RMS bunch length of 3.5 mm has achieved.

The IP2 area of the RHIC tunnel is large enough to place, side-by-side, two 20 MeV injectors, if cost considerations allow it. Such an arrangement would minimize the loss of average luminosity caused by limited cathode lifetime and the necessity to replace the cathodes. An expected cathode lifetime at the design current is about ? h.

### Beam Dump

A dump beamline transports the decelerated 12 MeV beam from the main ERL to the beam dump. The beamline consists of a dipole magnet, which is a part of the spreader, and two rastering quadrupoles, which disperse the beam over the beam dump surface. The aperture of the dump beamline is large enough to transport the decelerated beam with an energy spread of 2 to 3 MeV.

The beam dump has to be able to absorb a 600 kW heat load from the 12 MeV electron beam. The beam dump of the Cornell ERL Injector has been taken as the basis for the eRHIC dump because of the similarity of the beam parameters [1]. It is made of aluminum instead of copper to reduce neutron production. The dump consists of two sections: the body and an outer shell, containing the cooling water. The interior shape is designed to distribute the scattered electrons as uniformly as possible around the cooled surface.

## 2.2.2 SRF Energy Recovery Linac

The FFAG-based Energy-Recovery-Linac (ERL) will accelerate an electron beam to 20 GeV after 12 passes through a SRF linac, so linac energy is 1.67 GeV.

### Linac Configuration

The superconducting RF ERL concept allows recovery of the beam power spent for acceleration of particles by recirculating them after collisions back through the linac at an RF phase offset by 180 degrees with respect to the accelerating phase. Thus the ERL's RF systems will have to provide the power necessary to maintain stable amplitude and phase of the electromagnetic field inside the SRF cavities and to compensate for any parasitic energy losses incurred by the beam (due to synchrotron radiation, resistive wall and higher order modes). The maximum amount of parasitic beam power loss is set to 3 MW, which in turn limits the beam current at 20 GeV to 6 mA. The linac will be installed in the 200-meter long IP2 straight section of the RHIC tunnel. Parameters of the main SRF linac are listed in Table 2-4.

**Table 2-4:** Linac configuration.

<b>Energy gain [GeV]</b>	1.67
<b>RMS Bunch length [mm]</b>	3
<b>Bunch repetition frequency [MHz]</b>	9.38
<b>No. of RF buckets per RHIC revolution</b>	120
<b>Main linac RF frequency [MHz]</b>	647.4
<b>No. of SRF cavities</b>	80
<b>No of main cryomodule</b>	20
<b>Total active length [m]</b>	92
<b>Total linac length [m]</b>	175.68
<b>Filling factor</b>	0.53
<b>Real estate gradient [MV/m]</b>	9.48
<b>Number of Quad and BPM</b>	10?

Figure 2-11 shows the configuration of one main linac cryomodule. There are four 647 MHz 5-cell cavities in one cryomodule to provide 83 MeV of energy gain. Each cavity has 6 ridge waveguide HOM dampers, and there is one room temperature beam line absorber on each side of the cryomodule. The cryomodule parameters are listed in Table 2-5.

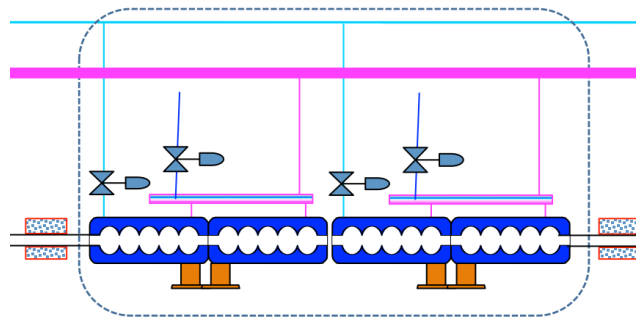


**Figure 2-11:** One 650 MHz cryomodule configuration.

**Table 2-5:** 647 MHz 5-cell cavity cryomodule.

<b>Energy gain [MeV]</b>	83
<b>Number of cavity</b>	4
<b>Accelerating gradient [MV/m]</b>	18
<b>RF coupler per cavity</b>	1
<b>Operation temperature [k]</b>	1.9

<b>Cavity intrinsic Q factor at operating gradient</b>	3E10
<b>Peak resonant frequency detuning due to microphonics [Hz]</b>	12
<b>Qext of FPC</b>	2.7E7
<b>RF power per cavity [kW]</b>	16
<b>Number of ridge waveguide per cavity</b>	6
<b>Number of RT beam line absorber</b>	2
<b>Maximum HOM power per cavity for nominal design [kW]</b>	2.8
<b>Maximum HOM power per cavity for ultimate design [kW]</b>	7.8
<b>Length of cryomodule with RT absorber [m]</b>	8.78

The beam energy loss will be compensated by a separate set of cavities operating at 1.3 GHz, second harmonic of the main RF frequency. The space of 10 m in the middle of main linac is accommodated for the energy loss compensation cavities. However, the beam simulation studies are underway to explore the possibility of eliminating these cavities. Figure 2-12 shows the configuration of energy compensation linac. The parameters for second harmonic cavity linac are listed in Table 2-6.

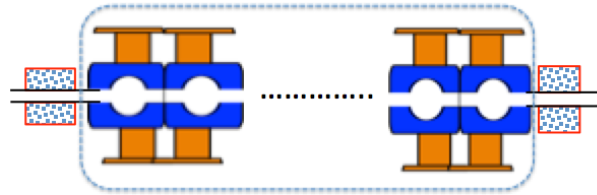


**Figure 2-12: Energy compensation linac configuration.**

**Table 2-6: 2<sup>nd</sup> harmonic cavity cryomodule.**

<b>Maximum Energy loss [MW]</b>	<b>3</b>
<b>Frequency [MHz]</b>	<b>1294.9</b>
<b>Number of cell</b>	<b>1</b>
<b>Number of cavity</b>	<b>14</b>
<b>Maximum Accelerating gradient [MV/m]</b>	<b>12.9</b>
<b>RF coupler per cavity</b>	<b>2</b>
<b>RF power per cavity [kW]</b>	<b>115</b>
<b>Qext of FPC</b>	<b>1E4~5E7</b>
<b>Operation temperature [k]</b>	<b>1.9</b>
<b>Cavity intrinsic Q factor at operating gradient</b>	<b>3E10</b>
<b>Peak resonant frequency detuning due to microphonics [Hz]</b>	<b>12</b>
<b>Number of RT beam line absorber</b>	<b>2</b>
<b>Maximum HOM power per cavity for nominal design [kW]</b>	<b>2.8</b>
<b>Maximum HOM power per cavity</b>	<b>7.8</b>



for ultimate design [kW]	
Length of cryomodule with RT absorber [m]	9.81

### Design of 5-cell 647 MHz cavity

The optimization of the high current SRF cavity is to maximize the HOM damping capability of the cavity while keep the fundamental mode performance. HOM damping optimization includes two aspects: one is to reduce the HOM power by minimize the loss factor, the other is to reduce the impedance to dipole modes to maximize the BBU threshold current. The frequency of the eRHIC SRF linac cavity was decided to be 647.4 MHz (69 harmonics of RHIC bunch frequency) to accommodate the existing SRF facilities [CAD note: frequency choice]. Figure 2-13 (top) shows Superfish model of the 5-cell 647 BNL4 cavity. The field profile of the fundamental mode by Superfish is shown in Figure 2-13 (bottom). The fundamental mode's performance of BNL4 cavities is listed in Table 2-7.

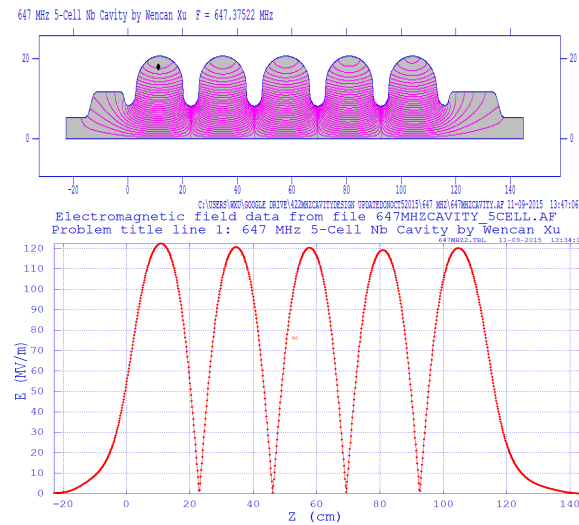


**Figure 2-13:** BNL4 cavity configuration (top) and fundamental mode field profile (bottom).

**Table 2-7:** RF parameters of the BNL4.

Parameters	647 MHz 5-cell cavity
Frequency [MHz]	647.4
Number of cells	5
Geometry factor [ $\Omega$ ]	273
(R/Q)/Cavity [ $\Omega$ ]	502
E <sub>peak</sub> /E <sub>acc</sub>	2.27
B <sub>peak</sub> /E <sub>acc</sub> [mT/MV/m]	4.42

Coupling factor		2.8
[%]		
Cavity length		1.72
[m]		

An average monopole mode HOM power generated by a single bunch travelling through a cavity is proportional to the bunch charge  $Q_b$ , beam current  $I_b$ , and the longitudinal loss factor  $k_s$ . The loss factor depends on the bunch length, as shown in Figure 2-14. The loss factor is 2.55 V/pC for a 3mm (rms) bunch length. With the nominal eRHIC beam parameters (7 passes at the maximum beam current of 26 mA ERL, 3 nC per bunch) for an intermediate energy, where the HOM power is maximal, an average value of monopole mode HOM power in one BNL4 cavity is 2.78 kW per cavity. However, the HOM power may change due to multibunch effects.

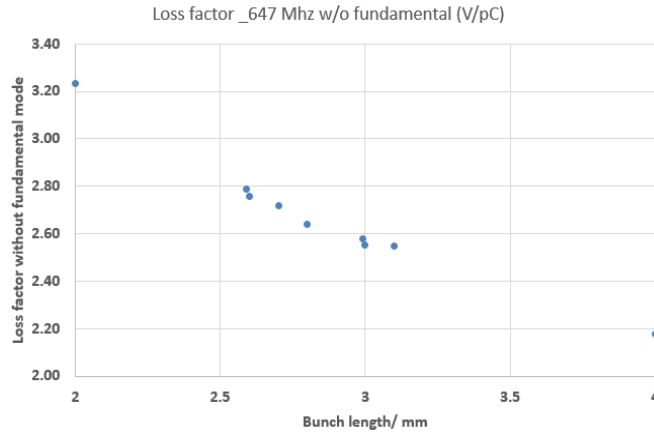


**Figure 2-14:** Integrated loss factors of BNL4 cavity.

Beam-Break-Up (BBU) threshold current is inversely proportional to the transverse mode impedance ( $R_d/Q * Q_{ext}$ ), so minimization of the transversal impedance was another effort during the cavity design. Figure 2-15 shows the dipole modes' impedance of BNL4 cavity. BBU code simulation shows that the threshold current of BNL4 cavity for eRHIC has at least a factor of 4 above the operation beam current, for a zero frequency spread due to fabrication (usually it is around a few MHz spread) in the HOM spectrum.

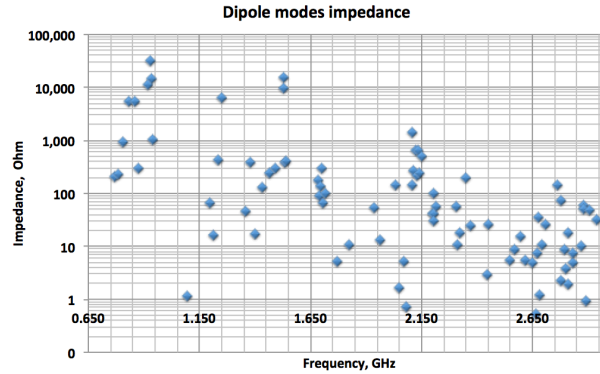


**Figure 2-15:** Dipole modes Impedance.

#### Prototype of the 5-cell 647.4 MHz cavity

In eRHIC design, the electron beams will collide with different proton energies from 40 GeV to 250 GeV, which corresponds to a frequency shift up to 174 kHz for 647 MHz cavity. ANSYS simulation shows that the cavity's tuning sensitivity is 84 kHz/mm, so the tuning range requirement for BNL4 cavity is 2 mm. With a 4 mm thickness of Nb sheet, the cavity can be tuned up to 2.0 mm without exceeding the yield strength of Nb: 7000 psi, which is shown in Figure 2-16. The Lorentz detuning factor of this cavity is  $0.6 \text{ Hz}/(\text{MV/m})^2$ . With middle lateral support, the frequency of the first mechanical mode is 107.2 Hz, which is a longitudinal mode.

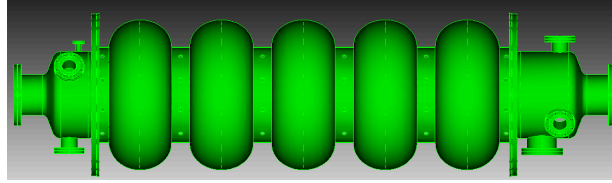


**Figure 2-16:** Prototype BNL4 cavity.

The BNL4 cavity will be prototyped with frequency scaled to 650 MHz. One niobium cavity will be fabricated for cavity performance study, and one copper cavity will be fabricated for HOM damping study.

#### Linac Optics

The goal of the linac optics is to minimize the beta function in the linac for all passes. In the eRHIC design, it was preferred to exclude quadrupoles from the linac to minimize the total length of the linac and leave more space for the spreader-combiner sections.

When quadrupoles are excluded, the only free parameters are the initial optical functions at injection energy of the lowest energy pass. The optical functions of consecutive passes are connected by this rule:

$$\beta_n(s = L) = \beta_{n+1}(s = 0); \alpha_n(s = L) = -\alpha_{n+1}(s = 0)$$

After optimization of the initial optical functions, the beta function of the linac through 16 accelerating passes is shown in Figure 2-17, and the optics of the decelerating passes are the mirror image of the same figure.

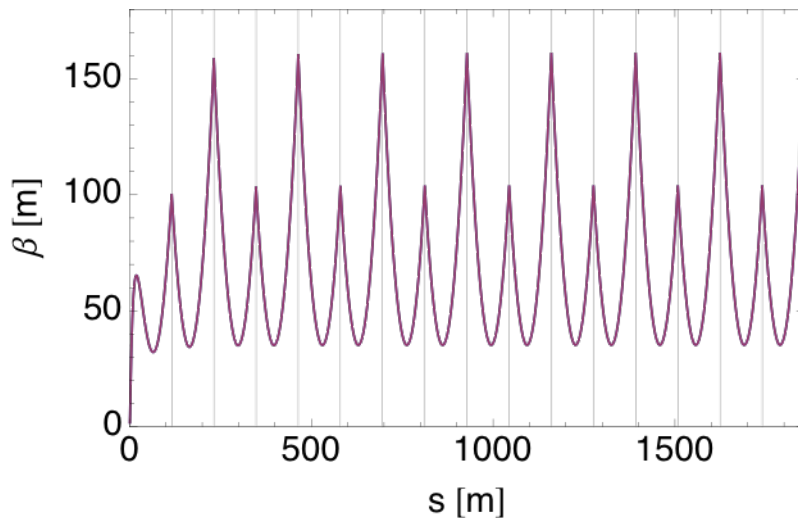


**Figure 2-17:** The beta function in the linac for 16 passes. The horizontal and vertical optics are identical. The grid lines separate the optics of each pass.

## 2.2.3 Time structure

### *Electron-Hadron Frequency Synchronization*

The eRHIC hadron beams are not ultra-relativistic, hence at the fixed closed orbit circumference the revolution frequency of hadron beam depends noticeably on its energy. In order to have the hadron and electron repetition rates synchronized in wide range of hadron energies the machine design has to incorporate a capability of varying the circumference of either hadron or electron beam transport lines. In eRHIC the hadron circumference control will be realized by radial shifts of the hadron closed orbit in hadron ring arcs. The radial orbit offsets of  $\pm 1.3$  cm would provide up to 16 cm hadron circumference variation range allowing the electron-hadron synchronization in the energy range 100-250 GeV/u.

To make the synchronization at lower hadron energies the harmonic switching method is used. Switching of the ERL RF harmonic number (the ratio of the RF frequency to the revolution frequency) down by one unit allows operating with hadron energies 43-46 GeV. And when switching to even lower RF harmonics some of lower proton energies can be accessed.

### *Bunch pattern*

In eRHIC  $N$ -pass (where  $N \leq 12$ ) ERL, there are  $2N$  bunches passing through a linac cross-section in one collision period (107 ns). The frequency of the RF cavity is  $f_{rf} = 647.5$  MHz, which is 69 harmonics of the collision frequency of 9.38 MHz. Therefore, there are 69 accelerating crests and 69 decelerating troughs available to accommodate  $N$  accelerating and  $N$  decelerating bunches.

The bunch pattern of the beam in the linac is determined by the path length of the recirculating passes, i.e. the time of flight from the end of the linac to the entrance of the linac for each energy. To ensure energy recovery process, the highest (collision) energy pass should have path length  $L_{he} = \left(M - \frac{1}{2}\right) \lambda_{rf}$ , where  $M$  is an integer and  $\lambda_{rf}$  is the wavelength of the cavity. Since the highest energy pass is realized as an individual transport beamline there is a relative freedom in choosing  $M$ , limited only by width of the RHIC tunnel. The lower energy passes in the eRHIC design all have the same path length  $L_{le} = K \lambda_{rf}$ . This path length accounts for the length of beam trajectory through a FFAG beam line as well as through the spreader and the combiner. Since the FFAG beamlines as well as the highest energy beamline are all placed inside the RHIC tunnel, their path lengths are close to the RHIC circumference 3834 m. The hadron revolution frequency satisfies  $f_{hrev} = f_{rf}/R$ , where  $R=8280$  is integer to guarantee the synchronization of both beams at collision point. New ERL pass length parameters can be defined as:  $k = R - K$  and  $m = R - M$ .

Figure 2-18 shows the desired bunch pattern for the 5-pass ERL in the ultimate design, i.e. top energy 8.5 GeV, where the current is maximum in the linac. This pattern is determined by the parameters  $k = 1$ ;  $m = -4$ . The pattern repeats every 69 RF periods, which corresponds to 9.38 MHz collision frequency.

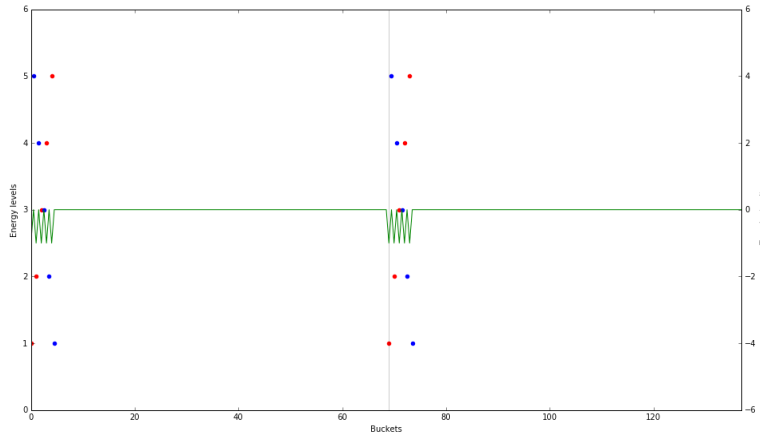


**Figure 2-18:** The bunch pattern for 5 passes ERL. The pattern repeats every 69 RF buckets. The red dots represent the accelerating bunches and blue dots represent the decelerating bunches. The green line indicates the voltage transient effect in the cavity.

This bunch pattern is optimized with the consideration of several beam dynamics effects and technical challenges, which include

- Ionization and ion effects,
- Single bunch information detection on the beam separation,
- Cavity HOM power generation by the beam,
- Voltage transient in the cavity.

The ion effects [Sec. 2.2.9] suggest that an electron bunch train gap should be implemented to counteract the ion accumulation and ion induced instability. In the meantime, the electron train gap also allows a special diagnostic bunch to be injected for easier beam diagnostics. Figure 2-19 illustrates the bunch pattern with train gap of 7 collision periods.

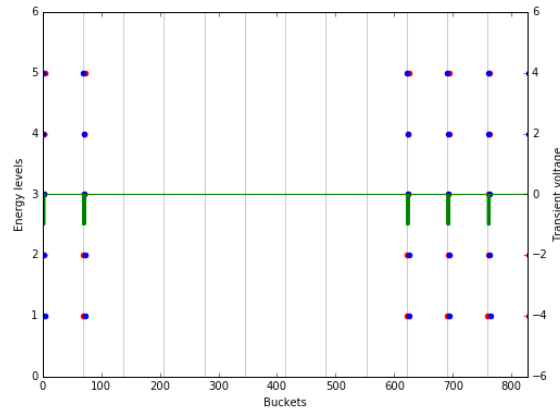


**Figure 2-19:** The bunch pattern in presence of the electron train gap. The grid lines repeat with collision frequency 9.38 MHz.

The key feature of bunch pattern is minimizing the voltage transient of the beam. The stored energy in the cavity is modulated by electron beam with the same pattern. The fast fluctuation cannot be compensated by the power coupler of the cavity due to its slow response time, therefore the energy variation creates the voltage transient in the cavity (green line in Figure 2-18). The unit of the transient voltage is the relative voltage variation caused by the bunch passing through the cavity, which gives:

$$\frac{dV}{V} = \frac{1}{2} \frac{dE}{E} = \frac{qV}{2 \frac{V^2}{\omega(R/Q)}} = \frac{q\omega(R/Q)}{2V}$$

In the 5-pass case, the bunch charge  $q$  has highest design value. The chosen bunch pattern is designed to minimize the energy difference between the regular bunch and the diagnostic bunch.

With the pass length parameters optimized for 5 pass case, the pass length of each energy recovery passes will be determined accordingly. Therefore, when eRHIC is operated as 12-pass ERL (20 GeV top energy), the transient effect will be less than optimum. However, in such high energy mode, the bunch charge of the electron beam is also decreased by one order of magnitude to maintain the same synchrotron radiation power. The transient effect is less pronounced due to the low bunch charge. Figure 2-20 shows the bunch pattern for the 12-pass ERL.

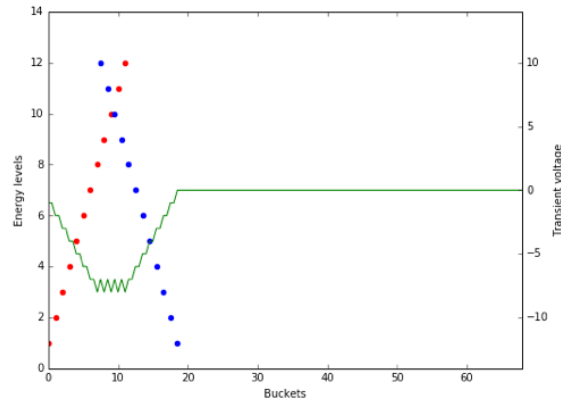


**Figure 2-20:** The bunch pattern for 12 passes ERL. The pattern repeats every 69 RF buckets. The red dots represent the accelerating bunches and blue dots represent the decelerating bunches. The green line indicates the voltage transient effect in the cavity.

The HOM power generated by the beam also strongly depends on the bunch pattern in the linac. The bunch pattern will generate different HOM power than that predicted with a single bunch. The left most data point in Figure 2-21 indicates the HOM power calculated from the pattern in Figure 2-18. Although this bunch pattern choice does not yield the minimum HOM power, it still produce about 15% lower HOM power than that of single bunch.

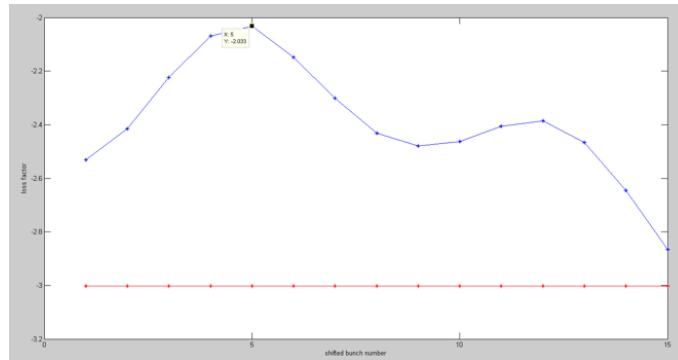


**Figure 2-21:** The HOM power of multi bunch pattern as function of the separation between the acceleration bunches and the deceleration bunches.



## 2.2.4 FFAG Lattice

### *Introduction*

The revival of scaling Fixed Field Alternating Gradient (S-FFAG) accelerators in the recent two decades is very evident, previously independently developed by Keith R. Symon, Tihro Okhawa, and Andrei Kolomenski [2],[3], [4] in the 1950s. They have a very large momentum acceptance with beams accelerated within a constant magnetic field that varies across the aperture according to the scaling law  $B(r) \sim B_0(r/r_0)^k$ , where  $k$  should be as large as possible ( $k \sim 150$ ). S-FFAGs have mostly been built in Japan: initially with the proof of principle (POP) proton accelerator at KEK, followed by the 150 MeV proton accelerator (presently at the Kyushu University), the 150 MeV accelerator at Osaka University, and many smaller size electron S-FFAGs built for different applications such as food processing. Although S-FFAGs have the advantages of fixed magnetic fields, zero chromaticity and fixed tunes, synchrotrons are still the dominant accelerators in spite of their requirement of pulsed magnets. This is mostly due to significantly smaller aperture requirements: a few cm in synchrotrons compared to  $\sim 1$  m for S-FFAGs, where large aperture magnets have to accommodate the orbit offsets. D. Trbojevic came to the concept of non-scaling FFAGs (NS-FFAGs) [5] by trying to reduce the required aperture of the S-FFAG by following the synchrotron light source lattice designed for minimum beam emittance. There was a publication by C. Johnstone a few months earlier about a FODO cell NS-FFAG [6]. Light sources require the smallest possible beam emittance, obtained by the minimizing the dispersion action  $\langle H \rangle$  integral [7]. This corresponds to searching for the smallest value of the dispersion function at the largest bending element. The connection to aperture size becomes evident from the definition of dispersion: the orbit offset:

$\Delta x = D_x \delta p/p$ , where  $D_x$  is the dispersion function, while  $\delta p/p$  is the momentum offset. If the dispersion is of the order of a few centimeters ( $\sim 3$ -4 cm) the orbit offsets will be  $\pm 15$ -20 mm for  $\delta p/p = \pm 50\%$  or a total energy range of 3 times for relativistic particles. An additional important novelty in the NS-FFAG is that the magnetic field is a linear function across the aperture in contrast to the non-linear radial field variation required in S-FFAGs. All magnets are linear combined function magnets. Abandoning the scaling law makes the tunes vary with energy, as well as the chromaticity. The time of flight is a parabolic-shaped function of energy. The minimum horizontal beta function is found at the middle of the bending element, as it is in the light source lattices, and this is the place where the orbit offsets are smallest, being the minimum of the dispersion function. The largest orbit offsets are in the focusing element together with the maximum of both the horizontal betatron function and dispersion function. The first NS-FFAG proof of principle machine was built and tested at Daresbury Laboratory [8].

### *Basic eRHIC NS-FFAG arc cells*

There are two NS-FFAG beam lines: one for the low-energy range 1.685 – 5.015 GeV with three passes, and a second one for the high-energy range from 6.685 – 20.0 GeV, with nine passes, making a total of twelve passes through the linac during acceleration. The basic cell is a doublet with combined function magnets made of displaced focusing and defocusing quadrupoles (Figure 2-22, Figure 2-23). The combined function magnets can be made of displaced quadrupoles as their displacement relative to the beam is very small due to the large bending radius  $\sim 320$  m.

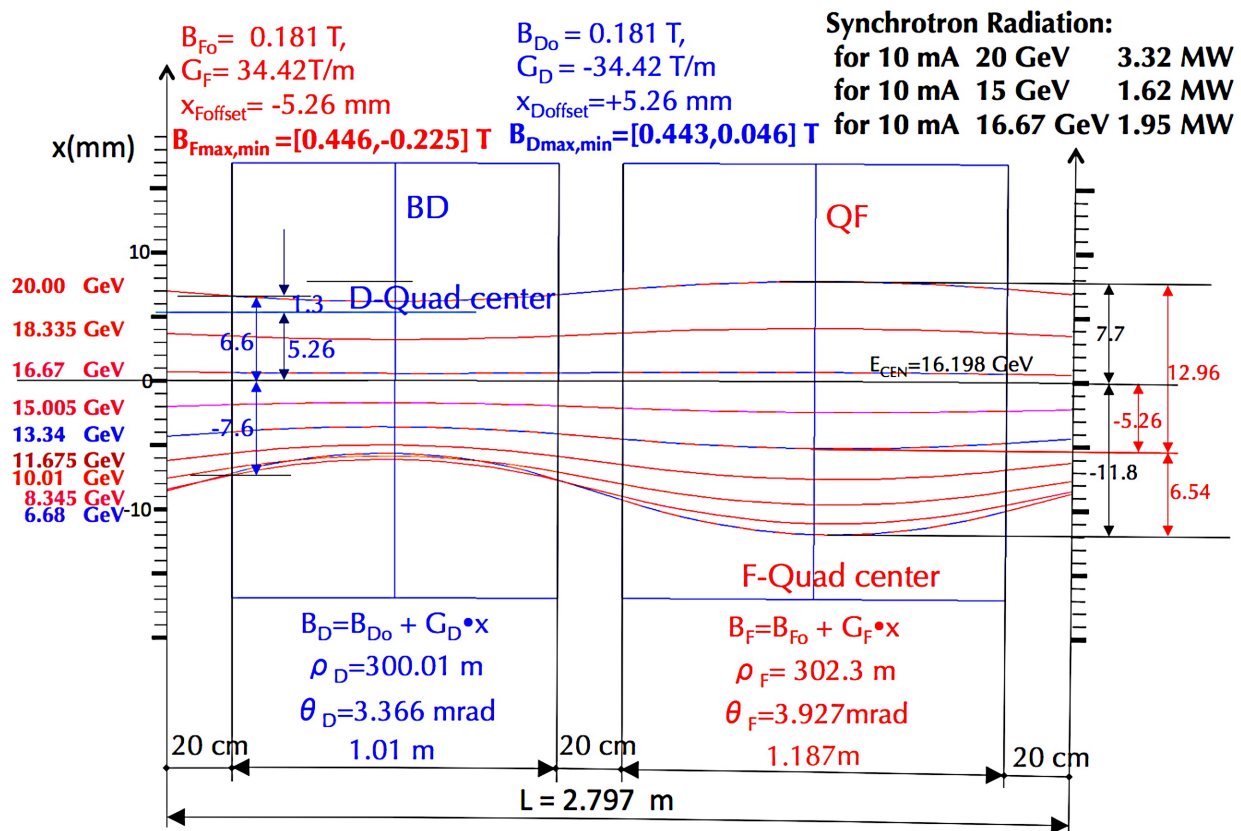
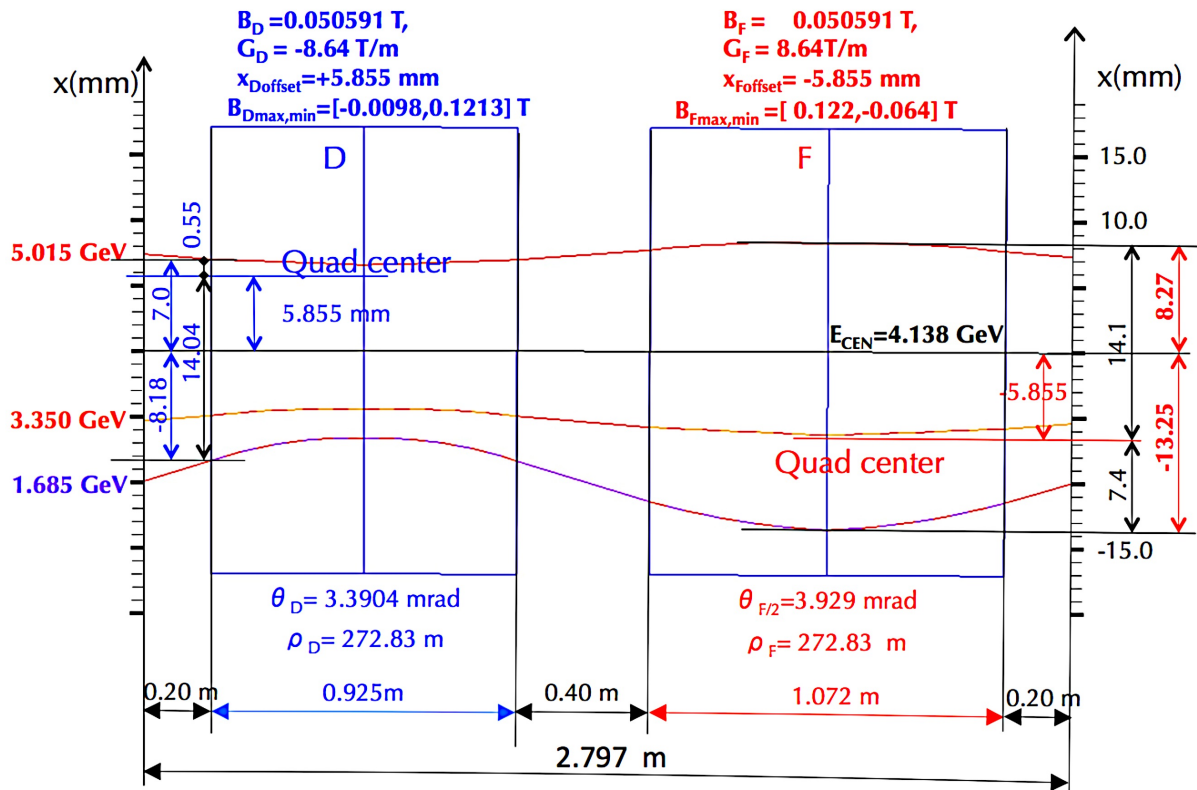


Figure 2-22: Magnets and magnified orbits in the basic cell of the high-energy beam line.



**Figure 2-23:** Magnets and magnified orbits in the basic cell of the low-energy beam line.

The tune variation as a function energy for the eRHIC low and high-energy NS-FFAG cell is shown in Figure 2-24. Contrary to the S-FFAG where the tunes vs. energy-momentum are constant, in the NS-FFAG they vary significantly. Orbits are stable within a range between the half and full integer.

The time of flight for the two NS-FFAG beam lines is shown in Figure 2-25. The dependence function is a parabolic shape with a largest difference of  $\sim 7$  cm for the six arcs, to be corrected with the spreaders-combiners separately for each energy.

The electron beam emits synchrotron radiation whenever it is bent in the magnets. The synchrotron radiation loss power is proportional to  $\sim B^2 E^2$ . A first reaction during the basic cell design is to make the orbit circular for the highest electron energy. But as the highest energy beam passes the NS-FFAG only once, while all other energies pass the same magnets twice: first during acceleration and the second time during deceleration, it is clear that optimization needs to be done quite differently.

As it could be noticed in Figure 2-22 the orbits in the basic cell are further apart in the focusing element.

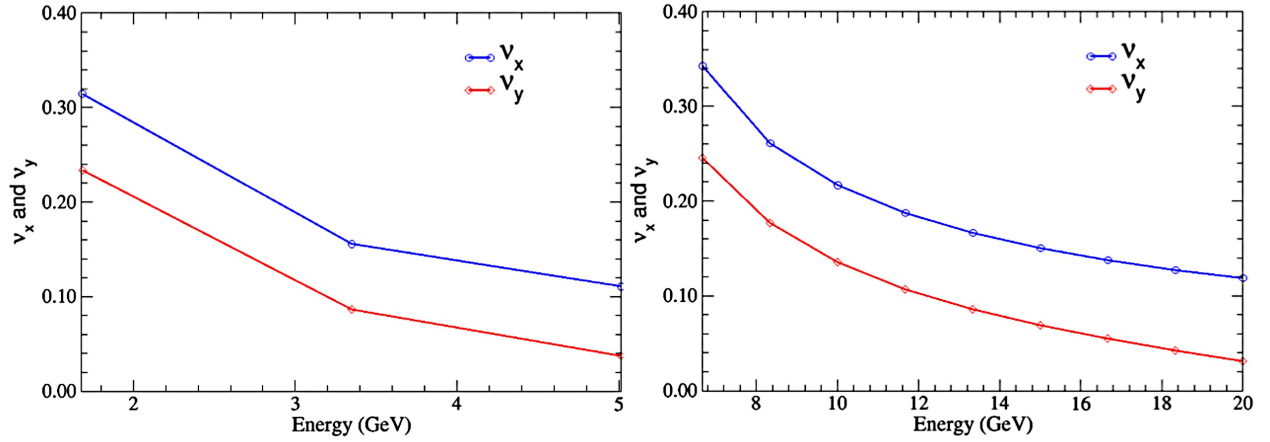


**Figure 2-24:** Tune dependence on energy for the low and high-energy cells.

It is desirable to have the smallest magnetic field for the highest energies in the focusing element as the magnetic field could be presented as  $B_F = B_{Fo} + G_F * x_{max}$ . The smaller the gradient  $G_F$  the smaller the effect of the largest orbit offsets on synchrotron radiation loss is. This indicates that it is preferable to have longer focusing than the defocusing magnet as the maximum if the magnetic field of the defocusing magnet is at the radially inward part of the orbits as:  $B_D = B_{Do} + G_D * x_{max}$  as the  $G_D$  has a negative sign. The optimized synchrotron radiation for all energies is shown in Figure 2-26.

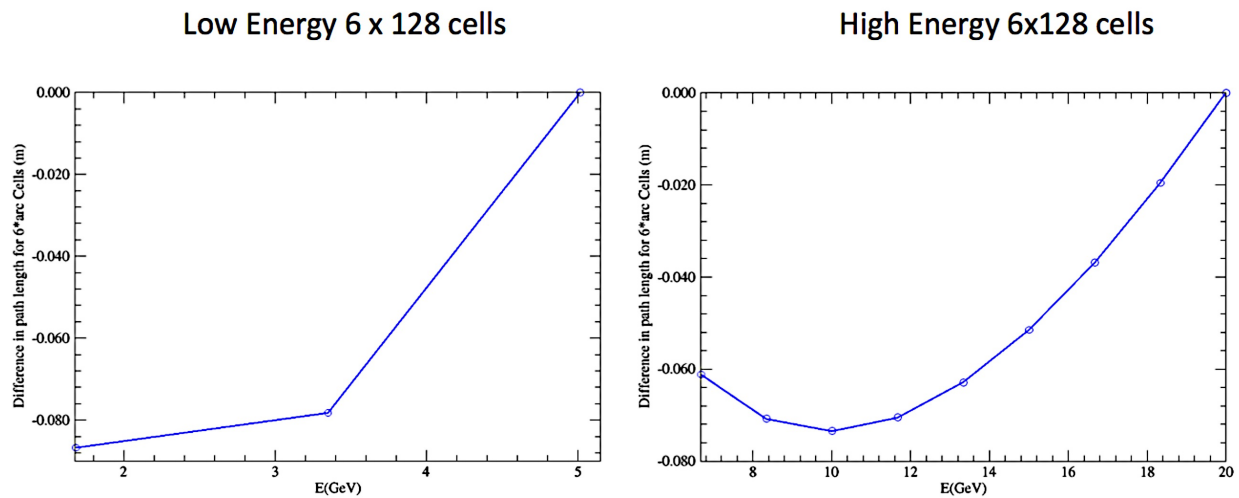


**Figure 2-25:** A difference in orbit time of flight or path length in the six FFAG arcs, for the low energy 1.685-5.015 GeV (left figure), and the high energy 6.8-20 GeV (right figure), the point of comparison was chosen arbitrarily at the highest energy.

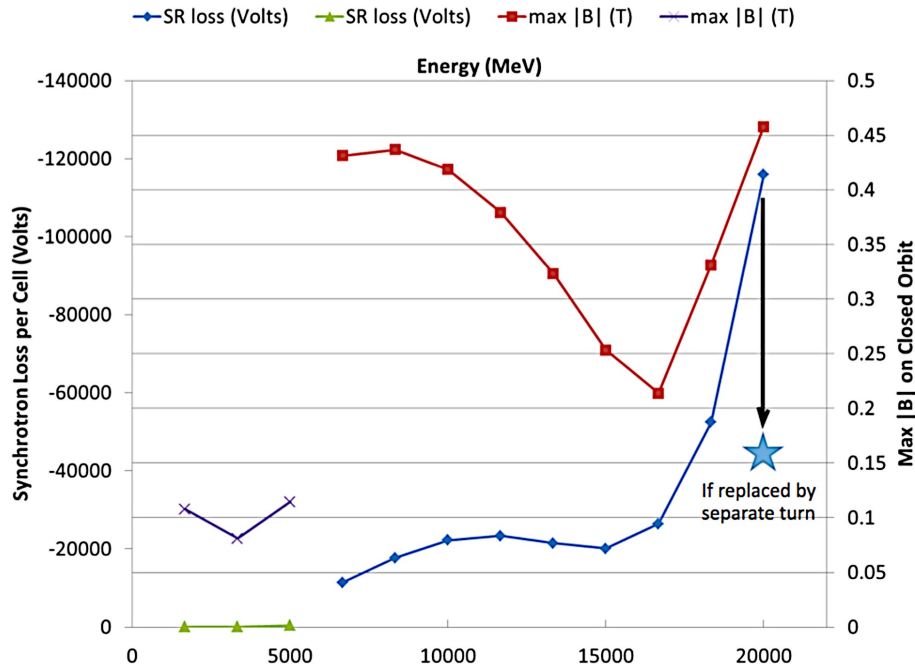


**Figure 2-26:** Synchrotron radiation loss for all energies.

### *Matching the NS-FFAG arcs with straight sections and bypasses*

There was a previous conceptual proposal for a racetrack Recirculating Linac Accelerator (RLA) using the NS-FFAG [9] for muon acceleration with Halbach permanent magnets. In that proposal the two straight sections were partially matched to the NS-FFAG arcs. A very successful matching of the NS-FFAG arcs to the straight sections, for all electron beam energies, has been developed for eRHIC by Stephen Brooks as shown in Figure 2-27 and Figure 2-28.

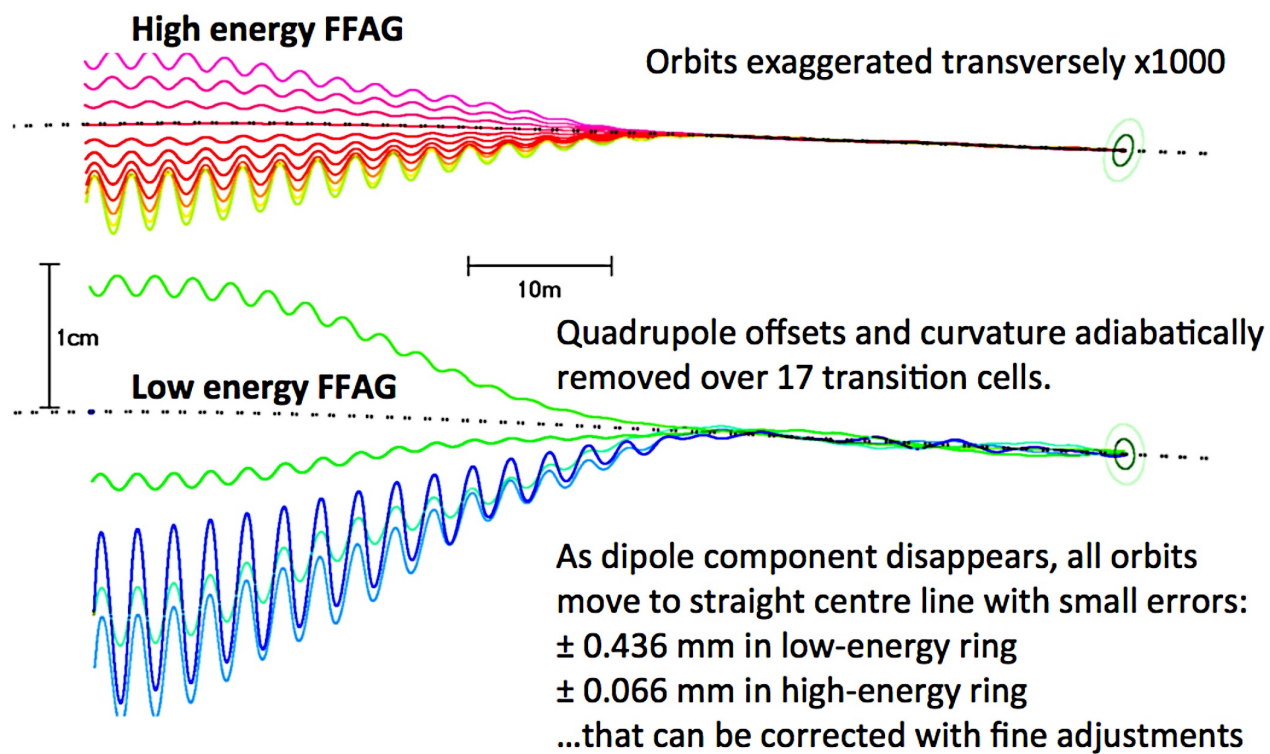


**Figure 2-27:** Matching the NS-FFAG arcs to the straight sections.

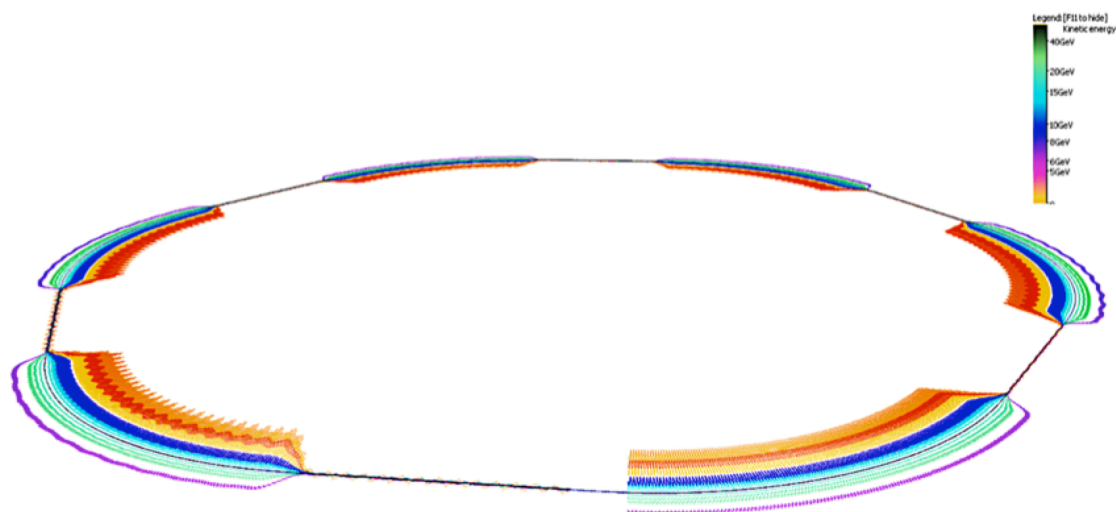


**Figure 2-28:** Straight sections and arcs' orbits magnified x1000.



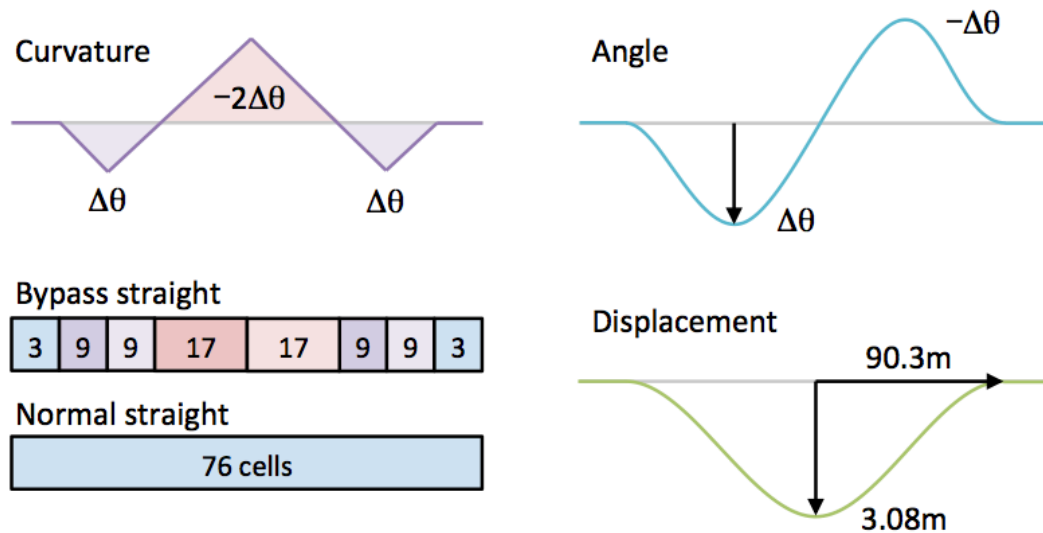


Figure 2-29: Principle of the bypass around the detectors.

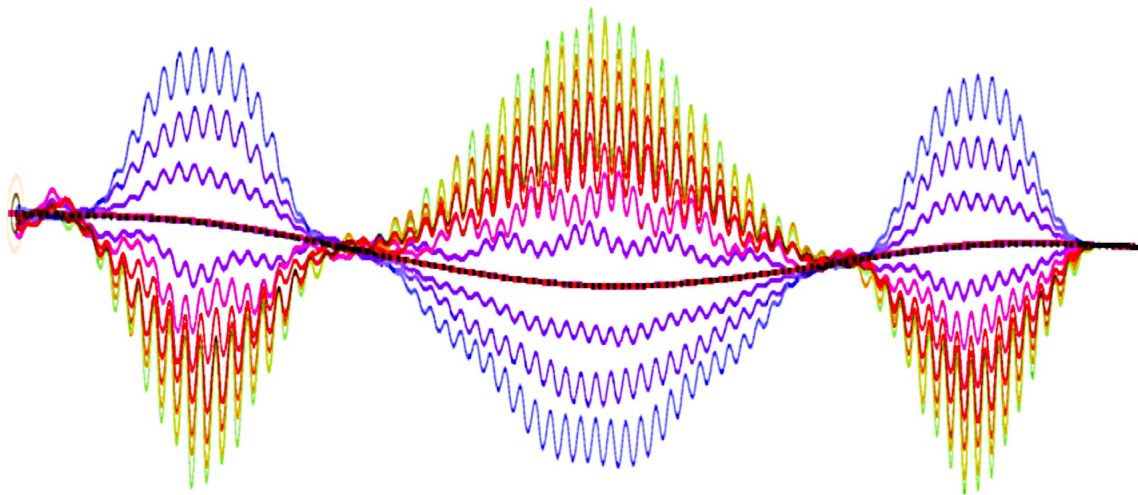


Figure 2-30: Details of the magnified x1000 orbits in the bypass around detectors in eRHIC.

The two NS-FFAG beam lines, placed in the existing RHIC tunnel, follow the curvature of the existing superconducting hadron beam line. The RHIC tunnel has six ~200-meter long straight sections the lines have to match. The straight section design provided the basis of the bypass design of the NS-FFAG beam lines around detectors (Figure 2-29, Figure 2-30), as only the highest energy is taken away to collide with hadrons, leaving the other energies in the FFAGs that must bypass the detector.

### *High energy transport beamline*

High energy beam transport (HEBT) line realizes transport of the electron beam at collision energy. The electron beam is transferred into the HEBT line from a corresponding speared arm. The beamline then runs around RHIC circumference and intersects the collision points at eRHIC detectors locations. Thus, the interaction region electron beamlines are parts of the HEBT line. The



total length of the HEBT line is defined by energy a bunch pattern. Using the design bunch pattern described in section 2.2.3, the HEBT line must be 3.5 RF wavelength (1.62 m) longer than the hadron circumference. Present arc lattice of the HEBT line is assumed to be similar to the lattice of storage ring described in Chapter 3.

The eRHIC NS-FFAG magnets will use permanent magnet material. There was previous experience with permanent magnets used for the anti-proton storage ring placed in the Main Injector at Fermi National Laboratory. They had used passive temperature compensation of the permanent magnet with a material with opposite temperature dependence 10. We have a couple of different approaches to the permanent magnet design: iron-dominated magnets with permanent magnet material SmCo or NdFeB designed by Wuzheng Meng (Figure 2-31) and Holger Witte (Figure 2-31, Figure 2-32), and Halbach type designs by Nick Tsoupas and Stephen Brooks (Figure 2-33 and Figure 2-34). Magnets are required to have an open aperture in the horizontal plane due to synchrotron radiation. In the case of Halbach magnet design this was accomplished by breaking the symmetry in both vertical and horizontal planes and displacing the Halbach elements in such a way that the 12 pole is reduced to a minimum. In the case of iron dominated magnets the permanent magnet material was placed in two different ways relative to the iron that allow an open horizontal plane as shown in Figure 2-31.

**Figure 2-31:** Two hybrid magnet designs – a combination of the iron dominated magnet with the permanent magnet: one of the left (from Wuzheng Meng) where the permanent magnet is shown by lighter blue color, and one on the right side of the picture (from Holger Witte) where the permanent magnet blocks are located on the top of the iron.

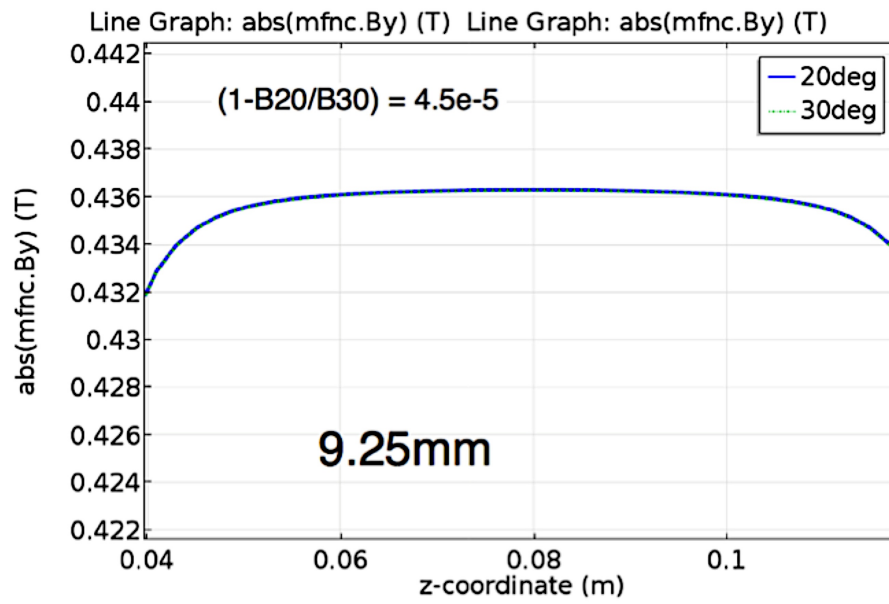


**Figure 2-32:** Holger Witte hybrid magnet design is able to compensate temperature very effectively, as shown in the figure where the 10 degrees difference 20C and 30C magnetic fields overlap.

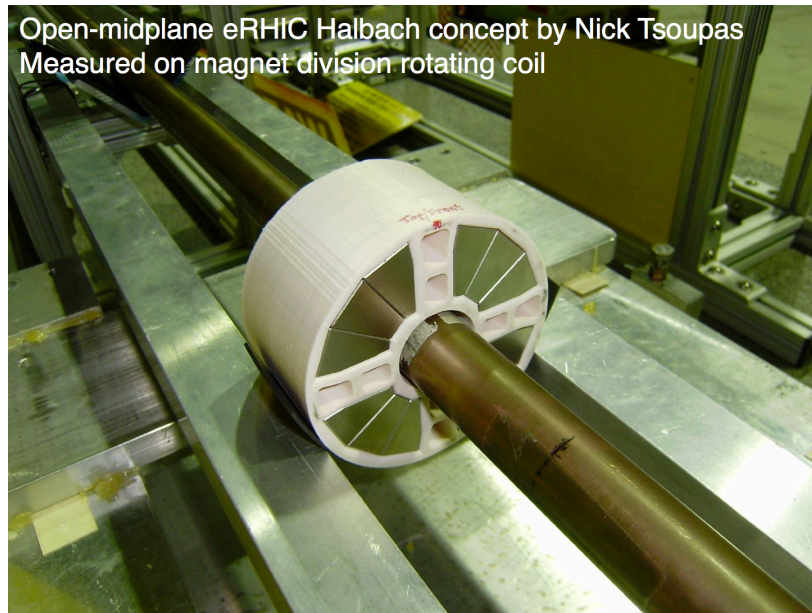


**Figure 2-33:** Magnetic measurements of the Halbach type magnet considered for eRHIC (from Nick Tsoupas, Stephen Brooks, and Animesh Jain).

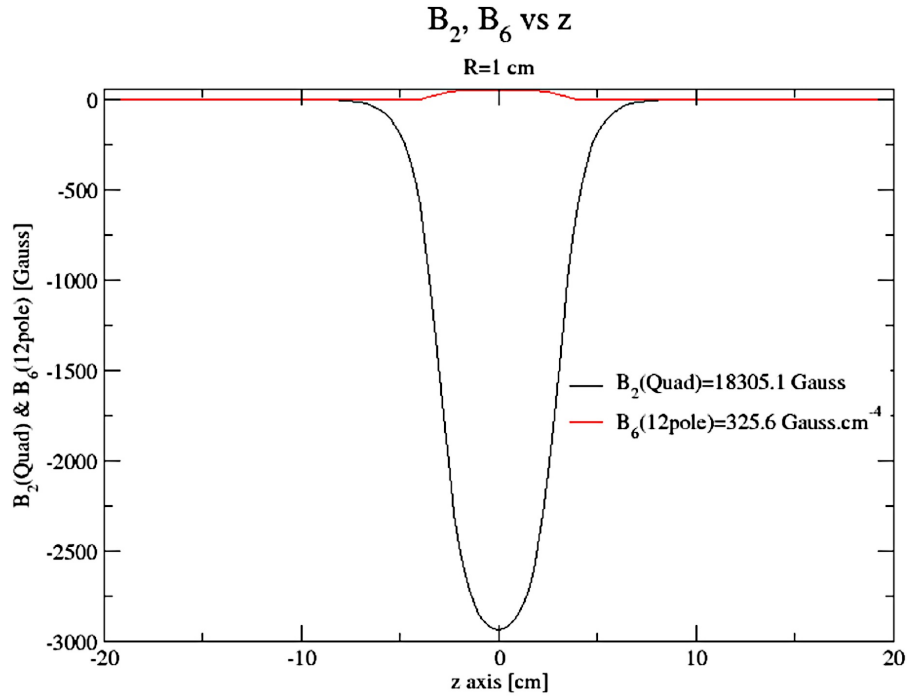


**Figure 2-34:** Three-dimensional magnetic field obtained by “OPERA” for the Halbach magnet (from Nick Tsoupas).

## 2.2.6 Splitter and Combiner

### Introduction

The splitter section of the eRHIC is a set of 12 beam lines to transport the beam bunches from the exit of the ERL to the entrance of the FFAG arcs. Each beam line transports the electron bunches with specified energy. The merger section of the eRHIC transports the beam bunches from the exit of the FFAG arcs to the entrance of the ERL. Figure 2-35 is a schematic diagram of the Splitter and Merger sections.

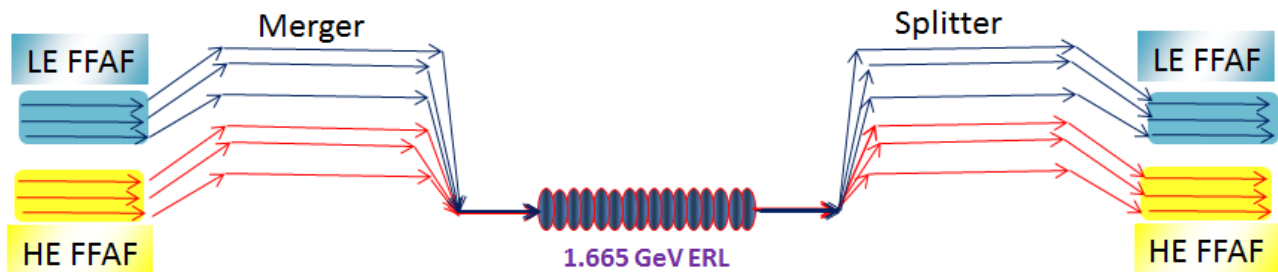


**Figure 2-35:** Schematic diagram of the splitter/merger . The merger is a set of 12 beam lines that merges the electron bunches from the FFAG arcs to the ERL. The splitter is a set of 12 beam lines that separates the

electron bunches exiting the ERL and distributes them to the FFAG arcs.

### *The functions of the Splitter/Merger*

- Below we list the most important functions of the splitter/merger.
- Transport and optically match the electron bunches from the exit/entrance of the ERL to the entrance/exit of the FFAG arcs.
- Make all the recirculating bunches isochronous by correcting for any path length differences between the electron bunches of different energies.
- Adjust the betatron phase advance to minimize the Beam Break Up (BBU) effect.
- Adjust the  $R_{56}$  Matrix Element of the orbit using Chicanes or Zig-Zag lines.
- Act as a beam-diagnostics and beam-control-lines of the electron bunches.

### *Path length difference of the splitter/merger lines.*

The various lines of the splitter/merger introduce different path lengths for the bunches with different energies. Table 2-8 lists the path length introduced by the various lines. The 2<sup>nd</sup> column in Table 2-8 is the path-length increase introduced by each line of the splitter/merger, column 3 is the half of the path-length increase introduced by the recirculating FFAG arc, column 4 is the sum of the values in columns 2 and 3. Column 5 is the path length increase to be introduced to each splitter/merger line to generate equal path lengths, and therefore isochronicity between the exit and entrance of the ERL.

**Table 2-8:** The values of the path-lengths introduced by the lines of the splitter/merger and the FFAG arcs. The last column is the path length increase to be introduced in each splitter/merger line to generate isochronicity between the exit and entrance of the ERL, for the various bunches.

KE [GeV]	Splitter/Merger Path-length [cm]	FFAG Pathlength/2 [cm]	Splitter/Merger+FFAG/2 Path-length [cm]	Compensation Path-length [cm]
20.000	1.6	4.03	5.63	9.02
18.335	2.4	2.97	5.37	9.28
16.667	3.4	2.03	5.43	9.22
15.005	4.8	1.23	6.03	8.62
13.340	6.4	0.60	7.00	7.65
11.675	8.2	0.18	8.38	6.27
10.010	10.8	0.0	10.80	3.85
8.345	14.4	0.25	14.65	0.00
6.680	13.4	0.13	13.53	1.12
5.015	22.6	3.82	26.42	10.22
3.350	24.6	0.00	24.60	12.04
1.685	36.5	0.14	36.64	0.00

### *The beam optics*

In this section we present the beam optics of two of the 12 beam lines of the splitter/merger, namely the beam optics of the high energy 20 GeV beam line, and the beam optics of the low energy 1.685 GeV beam line. Both beam lines include a chicane for path length compensation and also a chicane for  $R_{56}$  compensation.

### The 20 GeV Beam line

Figure 2-36 is a plot of the beam parameters  $\beta_x$ ,  $\beta_y$  and the  $\eta_x$ , and  $\eta_y$  dispersion functions of the 20 GeV beam line. The beam line matches the beam parameters at the exit of the ERL to those at the entrance of the FFAG arc. The yellow highlighted section is the path-length compensation section. This section includes the  $R_{56}$  section and the achromat\_1 and achromat\_2 sections.

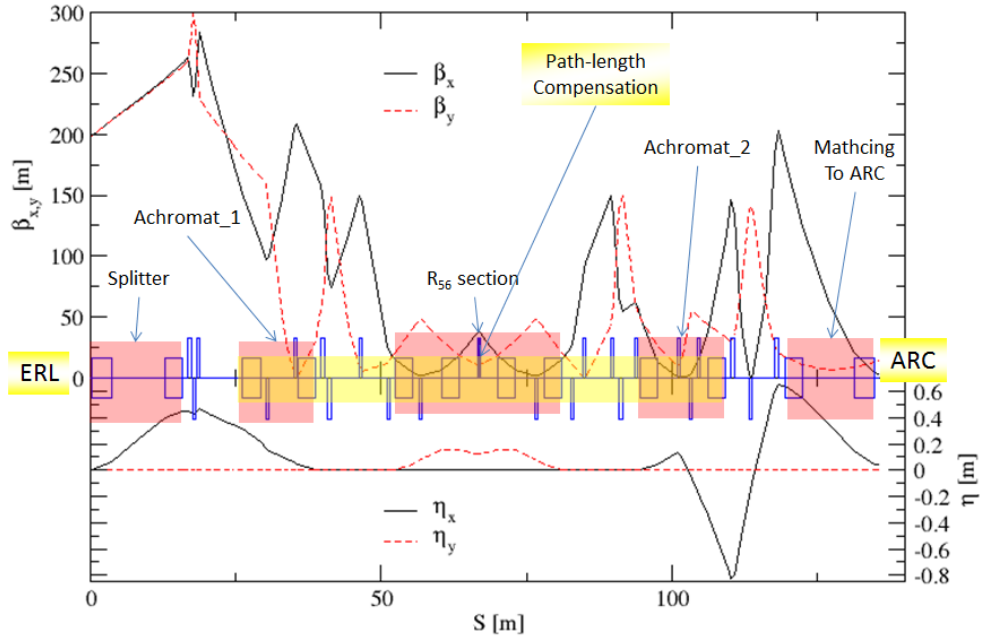


**Figure 2-36:** The  $\beta_x$ ,  $\beta_y$ ,  $\eta_x$ , and  $\eta_y$  functions of the 20 GeV beam line of the Splitter. The beam line matches the beam parameters at the exit of the ERL to those at the entrance of the FFAG arc. The yellow highlighted section is the path-length compensation section, which includes the  $R_{56}$  section and the achromat\_1 and achromat\_2 sections.

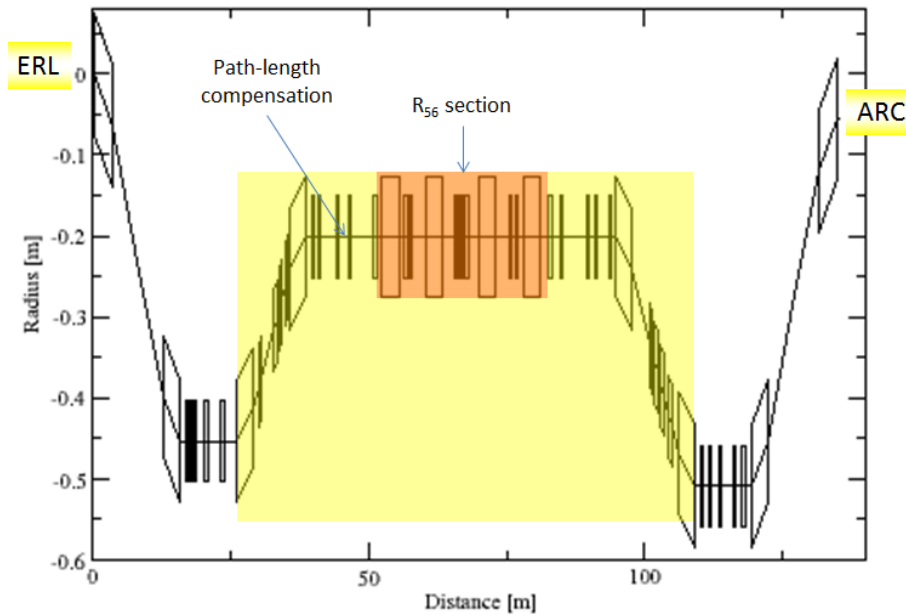


**Figure 2-37:** The layout of the magnetic elements of the 20 GeV line. The yellow highlighted region is the path-length-compensation section, and the red one is the  $R_{56}$  section. The transverse footprint of the elements

is much smaller than the width of RHIC channel.

### The 1.685 GeV Beam line

Figure 2-38 is a plot of the beam parameters  $\beta_x$ ,  $\beta_y$  and the  $\eta_x$ , and  $\eta_y$  dispersion functions of the 1.68 GeV beam line. The beam line matches the beam parameters at the exit of the ERL to those at the entrance of the low energy FFAG arc. The splitting section shown in Figure 2-38 can accommodate quadrupoles due to the larger separation of the adjacent lines as compared to the splitting section of the 20 GeV line which cannot accommodate quadrupoles. Since the three low energy lines transport the electron bunches to the low energy arc which is on top of the high energy arc, we have included in each of these lines a vertical displacement section that raise the bunches to the same level as the level of the low energy FFAG arc. This vertical section is achromatic. The chicane-path-length compensation section in Figure 2-38 is shaded by a blue strip. The  $R_{56}$  section and two achromatic sections shown in Figure 2-38 are part of the path-length compensation section.

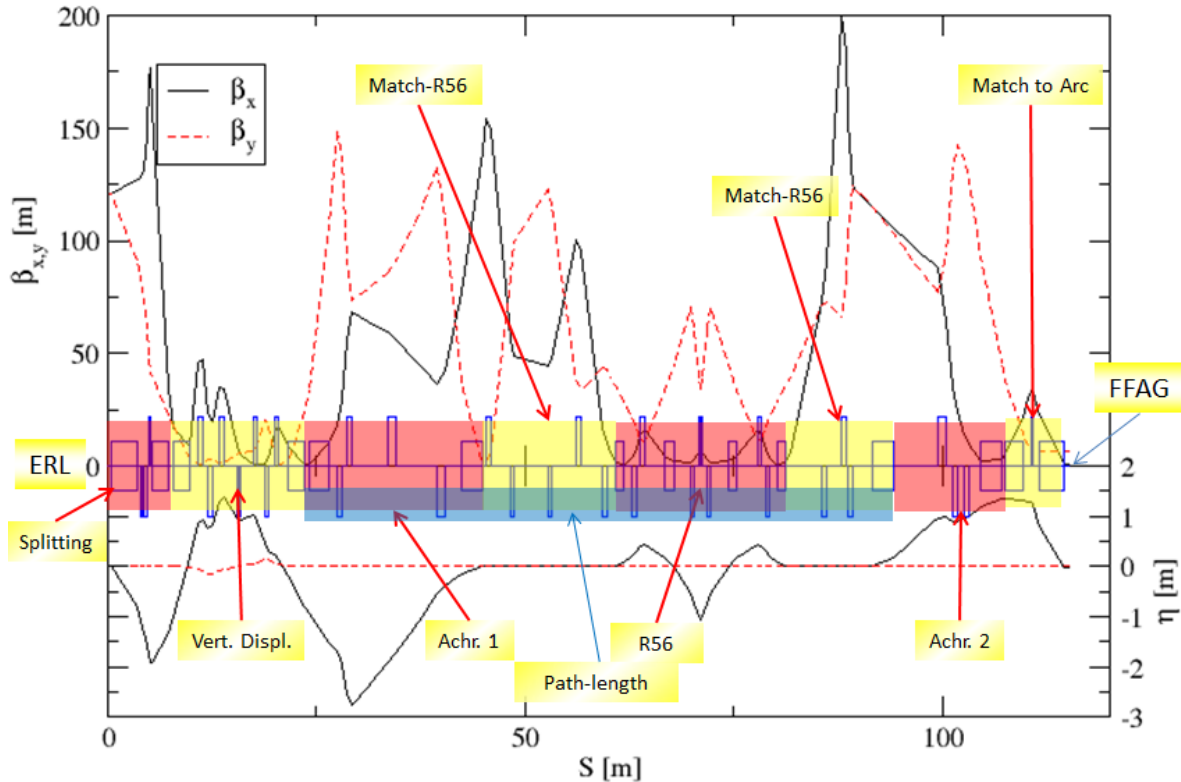


**Figure 2-38:** The  $\beta_x$ ,  $\beta_y$ ,  $\eta_x$ , and  $\eta_y$  functions of the 1.685 GeV beam line of the Splitter. The beam line matches the beam parameters at the exit of the ERL to those at the entrance of the FFAG arc. The blue highlighted section is the path-length compensation section which includes the  $R_{56}$  section and the achr.1 and achr.2 sections. The three low energy beam lines include a vertical displacement section shown in the figure. This section raises the electron bunches to the same level as the low energy FFAG arc.

Figure 2-39 is the layout of a low energy beam line. The yellow highlighted region is the path-length-compensation section, and the red one is the  $R_{56}$  section. In this layout the  $R_{56}$  section is horizontal, however it can be placed vertically to reduce the horizontal footprint of the line to  $\sim 2.5$  m. The vertical displacement section is also shown in Figure 2-39.



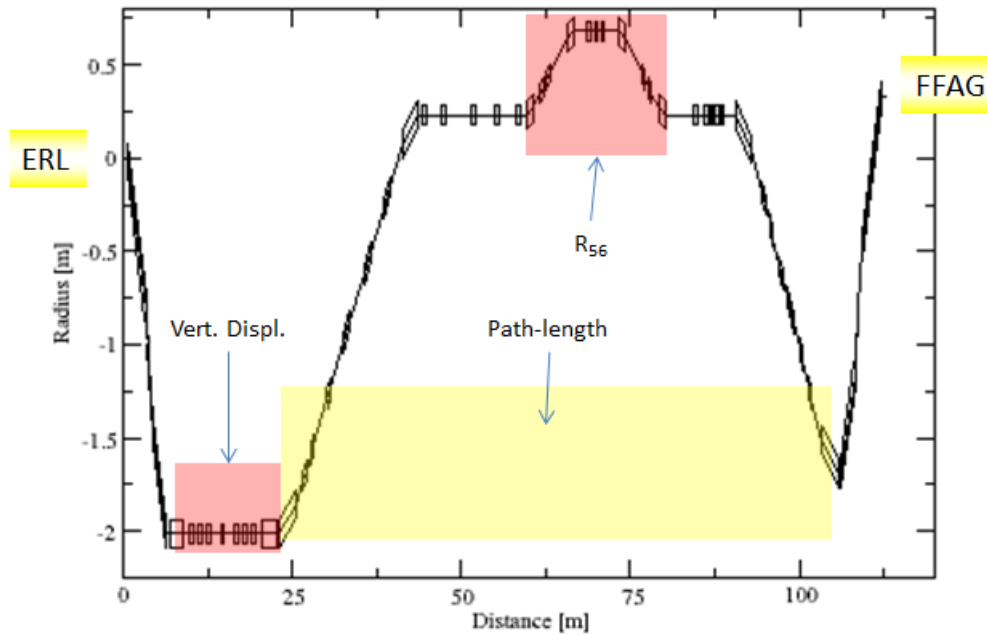


**Figure 2-39:** A representative layout of the magnetic elements for one of the three low energy beam lines. The yellow highlighted region is the path-length-compensation section, and the red one is the  $R_{56}$  section. In this layout the  $R_{56}$  section is horizontal, however it can be place vertically to reduce the horizontal footprint of the line to  $\sim 2.5$  m. The vertical displacement section is also shown in this figure.

#### *Magnet size consideration of splitter/merger*

The splitter /merger must fit in the RHIC tunnel which has an available transverse cross section of  $\sim 3$  m to accommodate the 12 beam lines. In this design of the splitter/merger we have separated the beam lines by 17 cm therefore the transverse size of the magnets cannot exceed 30 cm. Figure 2-40 is a schematic diagram of three consecutive beam lines with two magnetic elements in each of the two beam lines. The magnets of the splitter/merger should be electromagnets to provide beam control. To minimize the transverse size of the magnet one can make the electromagnet magnet longer.

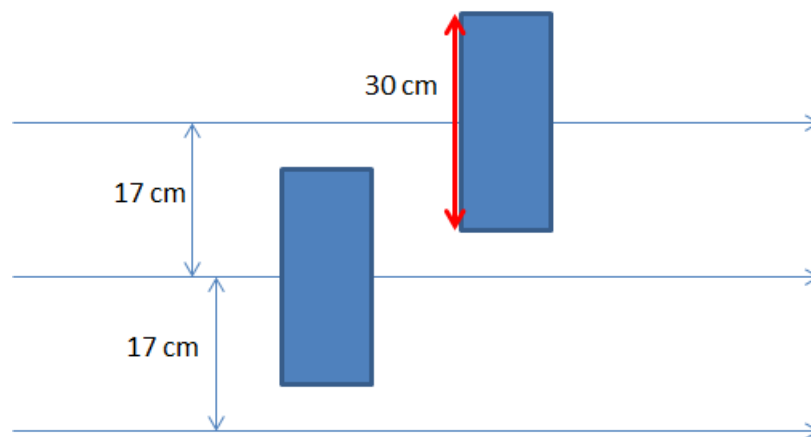


**Figure 2-40:** Schematic diagram of three consecutive lines of splitter/merger with two magnetic elements in two of the lines. The separation of the beam lines center to center is 17 cm therefore the transverse size of the magnetic elements should not exceed the 30 cm.

An alternative way of minimizing the transverse size of the magnets is to use hybrid type of magnet made of permanent magnets and electromagnets. Figure 2-41 is a schematic diagram of a hybrid dipole (blue and red rectangles on top) and a hybrid quadrupole (blue and red rectangles below), with the permanent magnets flanked by two low strength electromagnets of the same multipolarity. The cross section of a quadrupole and dipole permanent magnets is shown on the left and right side at the bottom of Figure 2-41. The cross section of such magnets is less than 15 cm including the magnetic shielding, which is the two blue rings surrounding quadrupole magnet on the bottom left. Similar magnetic shielding should exist around the dipole magnet. The red rectangles which flank the permanent magnets are low strength electromagnets of the same multipole for fine field control.

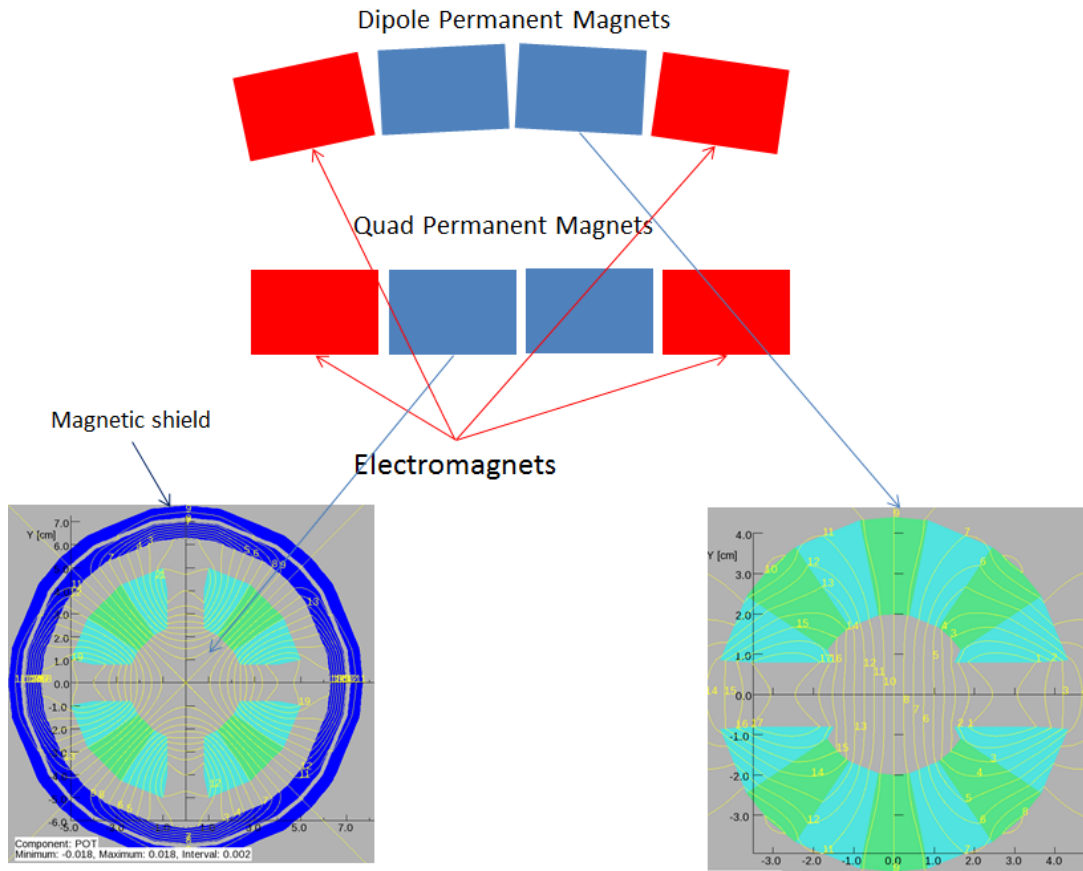


**Figure 2-41:** Schematic diagram of a hybrid dipole (blue and red rectangles on top) and a hybrid quadrupole (blue and red rectangles below), with each element flanked by two low strength electromagnets of the same multipolarity. The cross section of a quadrupole and dipole permanent magnets is shown on the left and right side at the bottom of the figure. The cross section of such magnets is less than 15 cm including the magnetic shielding, which is the two blue rings surrounding the quadrupole magnet. Similar magnetic shielding should exist around the dipole magnet. The red rectangles which flank the permanent magnets are low strength electromagnets of the same multipole for fine field control.

## 2.2.7 Correction Techniques

### Orbit Control

A unique feature of the beam trajectories in the eRHIC FFAGs is that multiple accelerating and decelerating bunches pass through the same magnetic lattice with different energy-dependent horizontal displacements (see Figure 2-22 and Figure 2-23). Since consecutive bunches are temporally spaced as close as  $\frac{1}{2} \lambda$ , a well-isolated bunch will be placed in the ion clearing gap (see Section 2.2.3) and used for time-resolved beam position measurements.

In the FFAG beamlines, since the beams of different energies respond differently to dipole correctors due to the energy-dependent tune, correction of one orbit will not improve other orbits passing through the same lattice. Therefore, dipole errors must be locally compensated to correct multiple orbits simultaneously.

The correction algorithm is based on that for a transfer line. For a single pass through the FFAG, or for any segment of that pass, assuming that the transport is linear, one needs to solve the equations  $\Delta Y = Y_0 - Y = R * \theta$ , where  $Y_0$  is the target orbit,  $Y$  is the measured orbit (or previously measured orbit),  $R$  is the response matrix, and  $\theta$  is the correction strength. This can be extended for a multi-pass correction as  $(\Delta Y_1, \Delta Y_2 \dots \Delta Y_m)^T = (R_1, R_2 \dots R_m)^T * \theta$ , where  $m$  is the number of passes. During the commissioning stage, beam may get lost at any point of the machine. In that case, the left side of the previous equation should be the measured orbit, which is a combination of any number of complete passes and a segment of one pass, and the transfer matrices on the right hand side should change accordingly.

We have done extensive studies on the effect of misalignment and magnetic field errors on the orbit position and ways to correct them with an orbit and gradient correction system. The need for correction is illustrated in Figure 2-42 which shows the rms of the simulated beam position as a function of rms random misalignment of FFAG magnets. There is a very clear magnification factor of 50-80x on the orbit errors depending linearly on the *rms* misalignment errors.

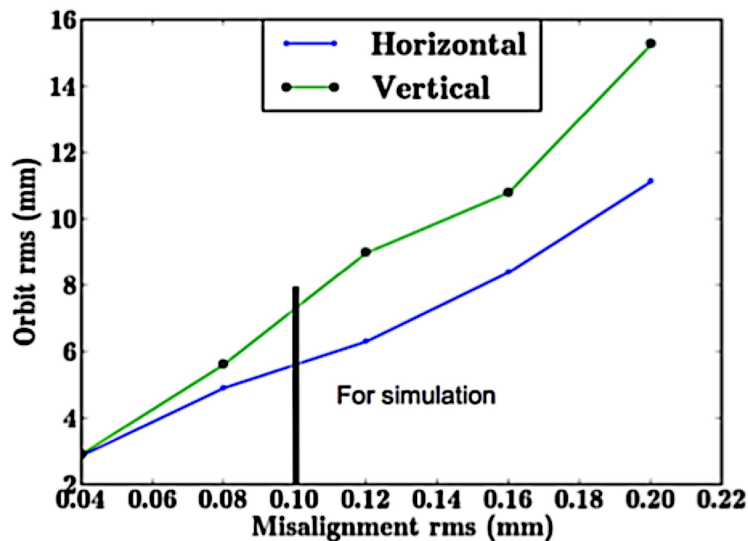
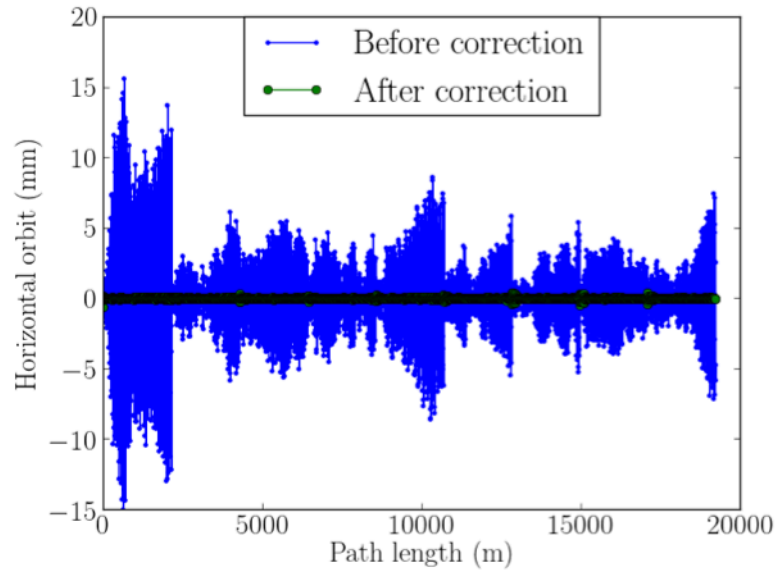


Figure 2-42: Magnification factor on the orbit due to misalignment errors.

The orbit correction method employed uses the methods developed and routinely used at RHIC. Orbit correction was simulated with reasonable estimates for the random alignment errors, gradient errors, angle errors in all the magnets, initial orbit errors and random BPM measurement errors. Two cases were simulated: (1) with the initial assumption of one horizontal, vertical, and one gradient corrector per FFAG cell and (2). one horizontal, vertical, and gradient corrector every two

FFAG cells. After the correction was performed for the lowest energy it was continued with higher energies.

The simulated initial orbits (relative to the corresponding design orbit) and the final orbits with correction are shown in Figure 2-43 for the case of 9 accelerating passes. In the simulation, the beam could be thread through the machine further with corrections applied to the existing orbit. The orbit errors at the end of every pass are corrected by the correctors in the spreaders and combiners (assuming not perfectly) so that the orbit of the next pass starts with some preset initial errors. With multiple passes, the local errors can be found and corrected better as the number of measurements increases. The final orbit rms deviations of all passes was reduced from the mm scale to  $\sim 50$   $\mu\text{m}$ .



**Figure 2-43:** The orbits of 9 accelerating passes with various errors (blue), and the orbits after beam being thread through the accelerator and correction being applied simultaneously on all passes (green).

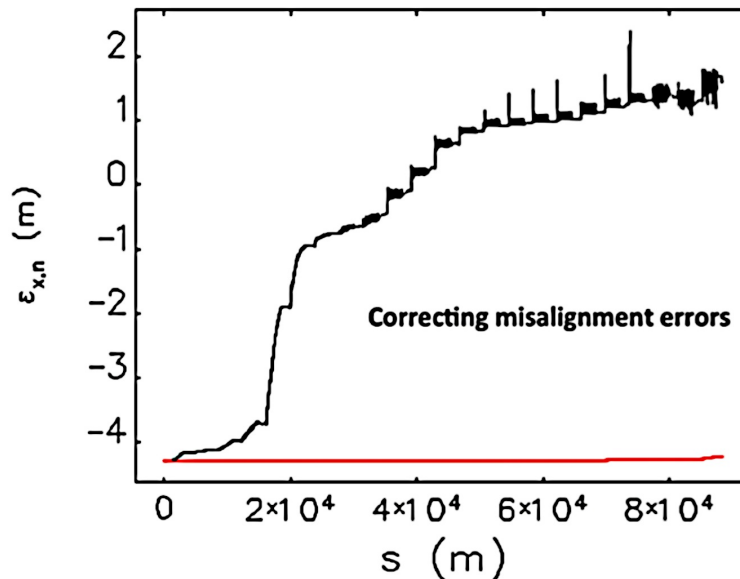


**Figure 2-44:** Emittance blow up due to misalignment and after correction. Vertical scale is logarithmic.

### Optics Measurement and Correction

In linear FFAG, orbit response deviation depends only on gradient errors linearly. The deviation of orbit response from the model can be measured by varying dipole correctors and recording the orbits. The gradient errors can be fitted with knowledge of the model. For a LINAC machine with  $m$  BPMs and  $n$  correctors, the orbit response matrix is

$$R = \begin{pmatrix} R_{1,1} & R_{1,2} & \dots & R_{1,n} \\ R_{2,1} & R_{2,2} & \dots & R_{2,n} \\ \vdots & \vdots & \ddots & \vdots \\ R_{m,1} & R_{m,2} & \dots & R_{m,n} \end{pmatrix} \quad (3-1)$$

The deviation of the orbit matrix  $R$  can be put in the form of a vector as  $V = (\Delta R_{1,1}, \Delta R_{1,2}, \Delta R_{1,3} \dots \Delta R_{2,1}, \Delta R_{2,2}, \Delta R_{2,3} \dots \Delta R_{m,n-2}, \Delta R_{m,n-1}, \Delta R_{m,n})^T$  with  $m * n$  elements. It is linearly proportional to the gradient errors.

$$V = \begin{pmatrix} M_{1,p} & M_{1,p} & \dots & M_{1,p} \\ M_{2,p} & M_{2,p} & \dots & M_{2,p} \\ \vdots & \vdots & \ddots & \vdots \\ M_{mn,p} & M_{mn,p} & \dots & M_{mn,p} \end{pmatrix} \Delta G \quad (3-2)$$

where  $\Delta G$  is a vector of the gradient errors for all quadrupoles. The number of quadrupoles is  $p$ .  $M$  is a  $m * n$  by  $p$  matrix.

The model orbit response matrix can be obtained using accelerator simulation codes. The matrix  $M$  can be simulated as well. For each quadrupole magnet, one can produce the orbit response matrix with and without some small quadrupole errors. The ratio between the difference of  $R$  and the gradient errors corresponds to one column of matrix  $M$ , which represents the coefficients to the strength of a given quadrupole. A set of linear equations will be established as Eq. 3-2, with gradient errors  $\Delta G$  as unknowns. The errors can be calculated by linear fitting techniques. In the following simulation, the singular value decomposition (SVD) is applied to solve the equations.

In multi-pass machine like eRHIC, the orbit response of all energies will be distorted by gradient errors differently. Therefore, the orbit response deviation for all passes should be measured and be used for more accurate calculation of the gradient errors.

The optics correction scheme was demonstrated using MADX-PTC code. For simplicity, there are 10 basic FODO cells, which include 20 correctors, 20 quadrupole magnets and 5 BPMs, in the lattice for simulation. In principle, dipole errors would not change the orbit responses. Therefore, no dipole errors were assigned in the simulation. There were no BPM calibration or coupling errors. During commissioning, beam may start only be able to pass once in the FFAG lattice. Therefore, we first did the simulation assuming only orbit response matrix for the first pass can be measured. We have less information for quantifying the gradient errors, even though the number of measurements (two times (dual planes) the product of the number of correctors and the number of BPMs) is larger than the number of unknowns (the number of quadrupoles). The simulation results are shown in Figure 2-45. The large assigned gradient errors can be found quite precisely (within 5%).

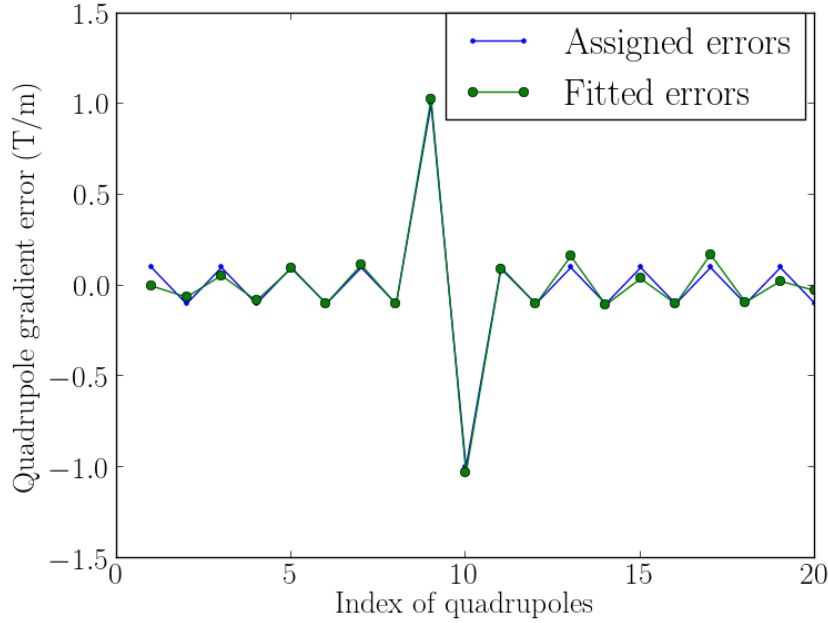


**Figure 2-45:** Comparison of the assigned and fitted gradient errors of 20 quadrupole magnets in eRHIC lattice. One the orbit response matrix of the first pass was used in the simulation.

Once the beam can be accelerated and decelerated through all passes, one could measure the orbit response deviation for beams with all energies. Then the number of measurements will increase to be two times of the product of the number of correctors, the number of BPMs and the number of passes. The simulation results for the case of all passes are shown in Figure 2-46. All errors can be found with accuracy of  $\pm 5\%$  except for the first two quadrupoles. The reason for less accuracy is that there were correctors inside (not upstream) of the first two quadrupoles, therefore, the orbit response matrix only depends on the errors of the first two quadrupoles weakly.

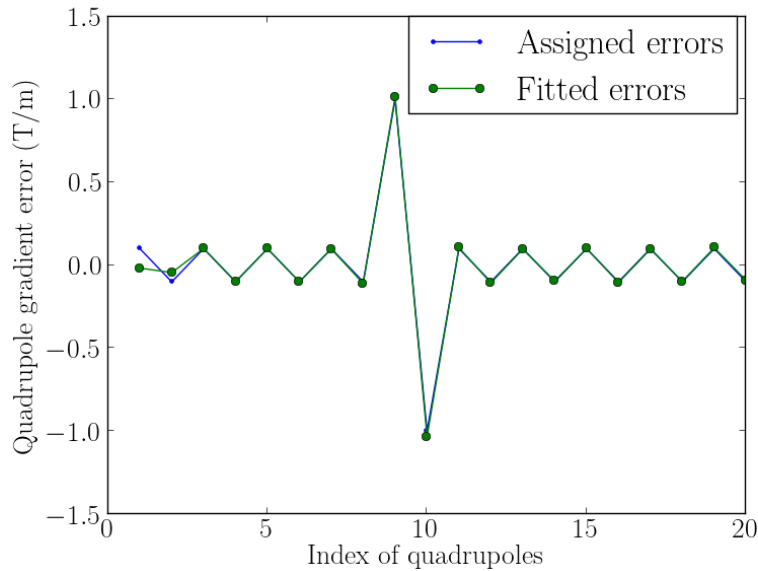


**Figure 2-46:** Comparison of the assigned and fitted gradient errors of 20 quadrupole magnets in eRHIC lattice. The orbit response matrix of all passes were used in the simulation.



Further improvement of the simulation can be made to include coupling and BPM calibration errors. The accuracy of find errors is expected to suffer with more unknowns being introduced in the simulation. However, the simulation with all possible errors included will help us better find errors in the real machine. In the simulation, only certain number of eigenvalues was kept so that we match the fitted and assigned errors the best. The method of cutting eigenvalues in the simulation would serve as guidance when we apply the technique in the experiment.

### 2.2.8 Start-to-end Simulations

The current start to end simulation of the multi-pass ERL of eRHIC starts with the injection energy 20 MeV at the entrance of the linac. The beam is accelerated many times until it reaches collision energy and then decelerated to the dump energy. The simulation includes the linac through which the beam passes multiple times, as well as the 2 FFAG beamlines that accommodates beams with all energies. The design of the spreader and combiner is on-going. They are represented by the 6-D linear transfer matrix to match the optics function, time of flight and the compaction factor. Figure 2-47 illustrates the components and sequence of the start-to-end simulation.

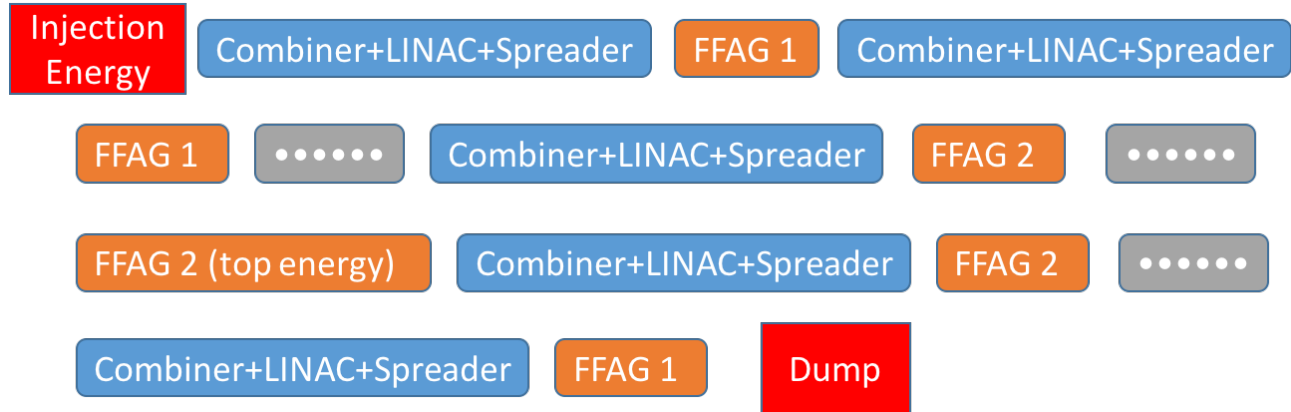


**Figure 2-47:** The components and sequence of start-to-end simulation.

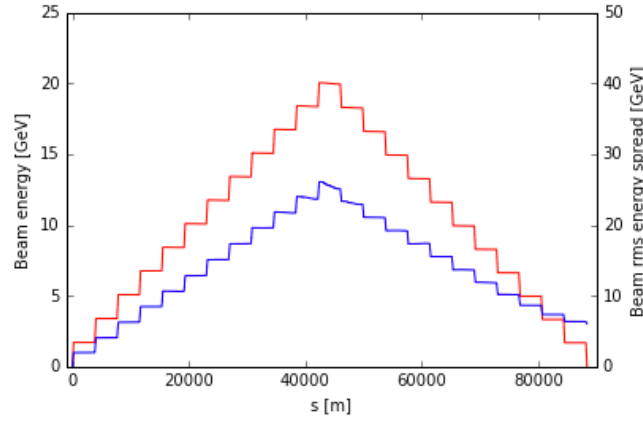
Two codes are now being used for this purpose, Elegant [11, 12] and Zgoubi. In Elegant, we use uses 4<sup>th</sup> order symplectic integrator to track the particles with large momentum deviation with wake field effects. Zgoubi is a ray-tracing code [13] uses Runge-Kutta methods to directly integrate the equation of motion to track the particle through. Zgoubi also provide the unique feature of spin tracking.

In elegant simulation, both the 650 MHz fundamental cavities and the second harmonic cavity are included in the linac. The voltage of the second harmonic cavity is determined by compensating the accumulated energy loss due to synchrotron radiation.

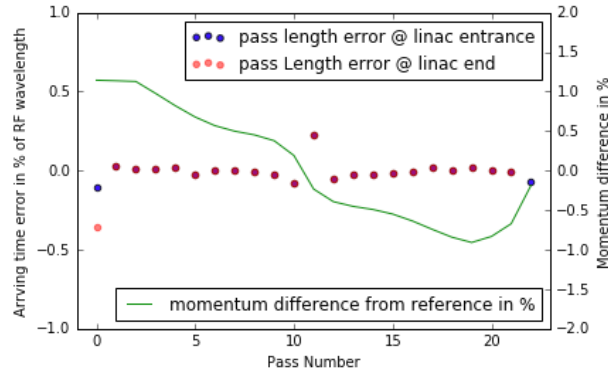
Figure 2-48 shows the energy and rms energy spread of the electron beam in the start-to-end simulation. The energy spread of the electron is contributed from the RF curvature and the synchrotron radiation. The energy spread due to the RF curvature when the beam is accelerated on-crest, can be compensated in the decelerating stage if the decelerating phase is Pi apart. The residue energy spread is dominated by the synchrotron radiation effect which can not be compensated.

Figure 2-49 shows the arriving time of the each energy pass in fraction of the wavelength of the cavity (the dots) and the energy deviation from the design energies of the electron beam. The deviation is inevitable because the beam energy compensation is evenly distributed through the cavity while the energy loss mainly locates in the high energy passes.

The simulation also determines the error tolerance of the pass length and compaction factor control, as shown in Table 2-9.



**Figure 2-48:** The beam energy(red) and rms energy spread(blue) of the electron beam through the start-to-end transport.



**Figure 2-49:** The pass length of error of each pass as function of pass number (blue and orange dots). The blue dots are measured at the linac entrance and the orange dots are measured at the linac exit. The green curve represents the momentum difference in each pass.

**Table 2-9:** Tolerance table.

	Tolerance
Pass length error (in wavelength of 650MHz cavity)	3e-4
Compaction factor (m)	0.05

The similar setup is simulated using Zgoubi. Figure 2-50 is the example of the Zgoubi simulation result, which shows emittance growth in the high energy FFAG lattice (accommodates 6.6 GeV to 21.2 GeV) with the previous electron parameters. The adoption of new FFAG parameter is undergoing.

The transverse correction scheme and error tolerance of the BPM reading is under investigation and will be included in the start-to-end simulation.

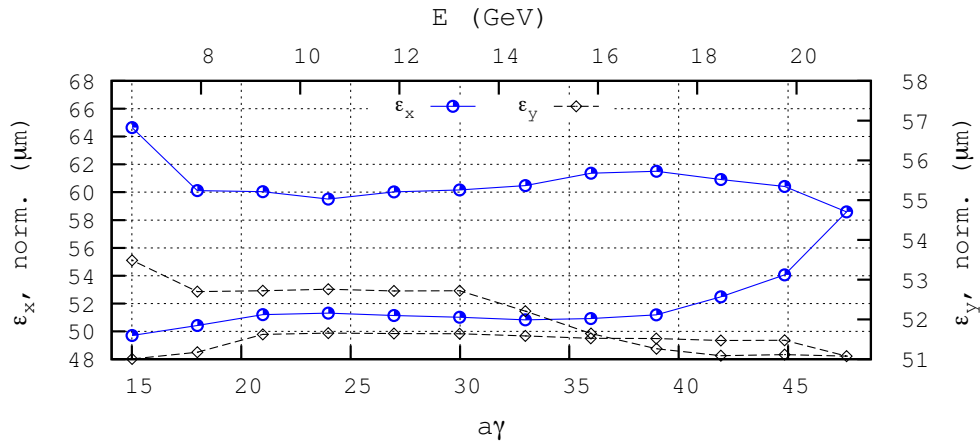


**Figure 2-50:** Markers in this figure (lines are to guide the eye) give the evolution of horizontal (left vertical axis) and vertical (right axis) bunch emittances under the effect of SR in the case of initial conditions: normalized emittance  $\sigma_x = \sigma_y = 50\pi\mu\text{m}$ , uniform random energy spread  $\delta E/E$  with rms value  $3e-4$  and  $\sigma_l = 0$ .

## 2.2.9 Beam Dynamics Effects

Various collective effects were studied and three effects have been recognized as most important: the energy losses and energy spread due to collective effects, multi-pass beam breakup instability due to high order modes of SRF cavities, and the fast beam-ion instability.

### *Energy losses and energy spread*

The following effects are investigated for potential energy losses and resulting energy spread: coherent synchrotron radiation (CSR), longitudinal resistive wall impedance, the higher order modes (HOM) of the SRF cavities, wall roughness of the beam pipe and synchrotron radiation. Table 2-10 summarizes our estimations for the current design. As shown in the table, we expect that the energy loss due to CSR will be suppressed by the shielding effects of the vacuum chamber of FFAG beamlines. Furthermore, the wall roughness of the extruded aluminum vacuum chamber can be reduced to sub-micron level<sup>1</sup> and its contribution to the energy spread is estimated to be negligible compared with other effects. The total power loss is about 2.5 MW, which has been compensated by a dedicated system of second harmonic RF cavities or by off-crest deceleration of the electron beam in main linac cavities. The full energy spread of the electron beam at its last pass through the linac is comparable or larger than its final energy going to the beam dump. The possible techniques to reduce this energy spread are under exploration.

**Table 2-10:** energy losses and energy spreads due to various collective effects with the top electron energy of 10 GeV (top) and 20 GeV (bottom).

	CSR	Machine impedances	Wall roughness	Synchrotron Radiation	Total
Energy loss, MeV	Suppressed	2.4	Negligible	67	69
		1.2		413	414

<sup>1</sup> We measured 0.2  $\mu\text{m}$  rms surface height variation from a sample aluminum beam pipe provided by ANL.

<b>Full energy spread, MeV</b>	Suppressed	3.8	Negligible	0.8	~4
		2		5.1	~6

### *Multi-pass beam breakup*

Multi-pass beam breakup (BBU) is the major limiting factor of the average current in ERL [14]. The BBU threshold for eRHIC is calculated by using the BBU code GBBU [15]. The higher order mode frequencies and the corresponding R/Q can be found in Figure 2-15. In the simulation, the HOM frequency spread is considered from no spread to 1% rms frequency spread. For non-zero frequency spread, 50 random seeds are used to get reasonable statistics. With  $10^{-3}$  rms errors, the threshold is mA. This is well beyond the planned current for 20 GeV (5 mA) and even the full current (50 mA) at 10 GeV.

**Table 2-11:** Current threshold of beam breakup of 20 GeV 12-pass ERL.

$\Delta f/f$ (rms)	Current Threshold (mA)	Standard Error (mA)
0	53	N/A
5e-4	95	7
1e-3	137	14
3e-2	225	22
1e-2	329	37

### *Fast beam-ion instability*

The fast beam-ion instability is caused by electron beams resonantly interacting with ions generated from ionizing the residual gas molecules. The instability is most pronounced when the ions are trapped in the beam passage by the periodic focusing force provided by the beam. In our current analysis, the ion is assumed to be  $\text{CO}^+$  with 1 nTorr pressure.

A weak-strong code has been developed to simulate the fast beam-ion instability in the two FFAG rings, which takes into account the non-linear space charge forces of the electron bunches and simultaneously simulates electron bunches from all energy passes. The simulation agrees with the theoretical estimation in the linear space charge limits and, in the absence of a gap between bunch trains, shows significantly slower but persistent growth with the non-linear space charge force being adopted. However, no growth of the coherent electron oscillation is observed from the simulation with a 950 ns gap introduced between two adjacent bunch trains, as shown in Figure 2-51 for 8 mA of average current and 23 passes of the FFAG arcs (for operations with 20 GeV top energy).

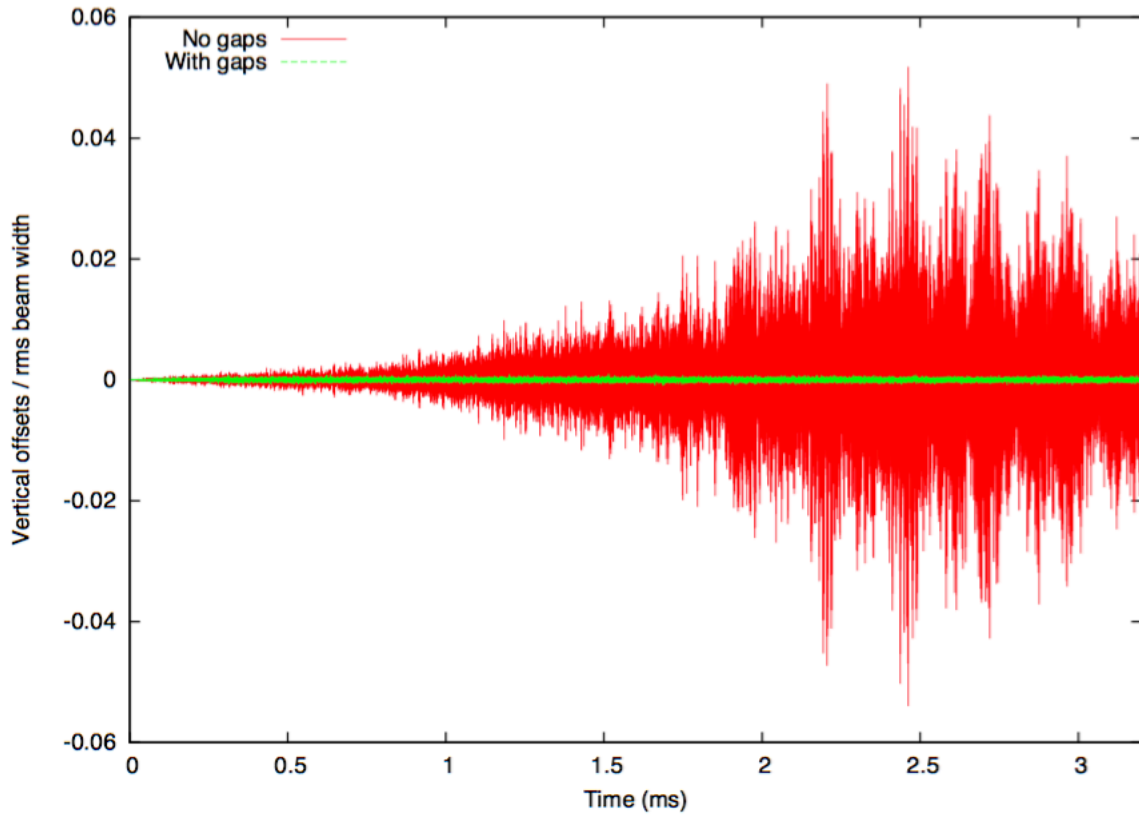


**Figure 2-51:** Simulation results of FBII in the low energy FFAG ring for the nominal linac-ring scheme of eRHIC. The abscissa is time in unit of millisecond and the ordinate is the offset of electron bunches, as observed at the exit of the ring. The red data points show the bunch offsets in case that there is no gaps between bunch trains and the green data points show the bunch offsets when clearing gaps of  $\sim 950$  ns are introduced. The simulation assumes 8 mA of average electron beam current and 23 passes of the FFAG arcs with a top energy of 20 GeV.

### 2.2.10 Beam Loss

While electrons travelling through the FFAG arcs and ERL, they interact with their neighbor electrons as well as the residue gas molecules along their passage. The interaction can cause abrupt changes in the momentum of electrons, making some of electrons fall out of the acceptance of the accelerator.

#### *Beam Losses Due To Gas Scattering*

Electrons in the beam can interact with residue gas molecules left in the vacuum chamber, leading to beam losses and formation of the beam halo. In addition, the lost high energy electrons may further induce desorption of the vacuum chamber, quenches the superconducting components and increase the background for the detectors.

Beam losses due to two types of beam-gas scattering have been analytically estimated for eRHIC FFAG rings: elastic scattering and Bremsstrahlung. The elastic scattering of the electrons in the beam off the residue gas molecules can change the trajectory of the electrons and excite betatron oscillation. If the scattering angle is larger than the deflection angle aperture set by the collimator, the electrons will get lost at the location of the collimator. In the process of Bremsstrahlung, an electron in the beam scatters off the gas nucleus and emit a photon, which results in an abrupt energy change of the electron. If the energy change is beyond the energy deviation aperture, the

electron will also be lost[2]. Using the parameters listed in Table 2-12, the beam losses due to gas scattering in eRHIC rings are analytically estimated and shown in Figure 2-52.

More accurate calculations can be carried out with the detailed lattice design and environment parameters. Further efforts on this subject involves estimation of other relevant processes such as electrons in the beam scattering with atom electrons around the residue gas nucleus and angle deviation due to Bremsstrahlung. The estimation can be further improved by simulating the losses process element by element.

**Table 2-12:** Summary of parameters used in estimation of beam losses due to beam-gas scattering.

	Arcs	Linac
<b>Electron bunch charge</b>	2.8 nC	
<b>Repetition frequency</b>	9.4 MHz	
<b>Gas species</b>	$N^{7+}$	
<b>Avg. beta function</b>	5 m	60 m
<b>Temperature</b>	300 K	2 K
<b>Pressure</b>	1 nTorr	$10^{-3}$ nTorr

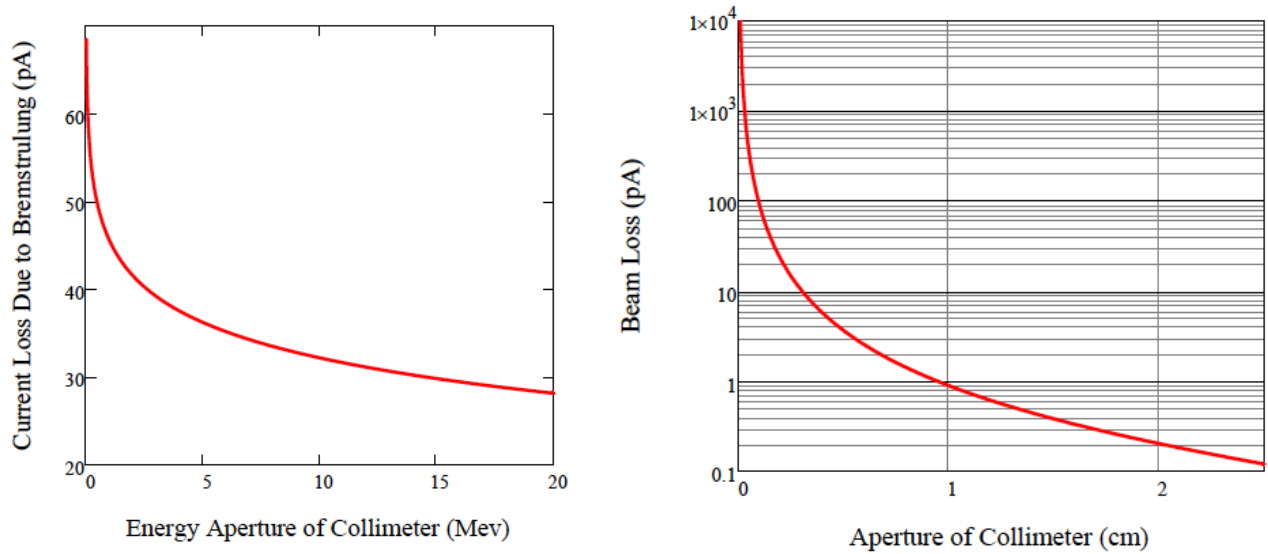


**Figure 2-52:** Analytical estimation of electron beam losses due to scattering off residue gases in eRHIC FFAG rings. Electron beam passes through the two FFAG rings for 11 times. (Left) beam losses due to Bremsstrahlung as a function of the energy aperture of a collimator located at the last pass of linac; (Right) beam losses due to elastic scattering as a function of the aperture of a collimator located at the last pass of arc. In generating the plots, we assume that the residue gas is dominated by 1 nTorr of  $N^{7+}$  and the average electron beam current is 26 mA.

#### ***Beam losses due to Touschek scattering***

While multiple small-angle scattering within charged particle beam usually degrades emittance, depending on the momentum aperture, large-angle Moller scattering among electrons can cause instant beam losses, the so-called Touschek effect. For eRHIC's analytical estimation of beam losses due to Touschek effect a round electron beam was considered. It was found that for 6MeV energy-deviation acceptance, the total beam losses due to Touschek effect are 200pA.



## 2.2.11 Beam-Beam Effects

Beam-beam effects present one of the major restrictions in achieving higher luminosities. eRHIC adopts the linac-ring scheme to remove the beam-beam effect limit of the electron beam and aims for higher luminosity than a traditional ring-ring scheme. There are several challenging effects in the linac-ring scheme, including the electron disruption effect, the pinch effect, the ion-beam kink instability and the ion beam heating due to electron beam noise.

Electron disruption effect rises due to the large beam-beam parameter of the electron beam proposed in eRHIC. The strong nonlinear beam interaction field will distort the electron beam distribution and the large linear tune shift leads to significant mismatch between the designed optics and the electron beam distribution. The effect was studied in detail in [16]. Figure 2-53 shows the beam distribution after the collision and the electron beam size and emittance evolution in the opposing ion beam. The emittance growth and beam size blow-up due to the electron beam disruption effect are in acceptable range and will not affect the beam transport and energy recovery process in the beam decelerating stage.

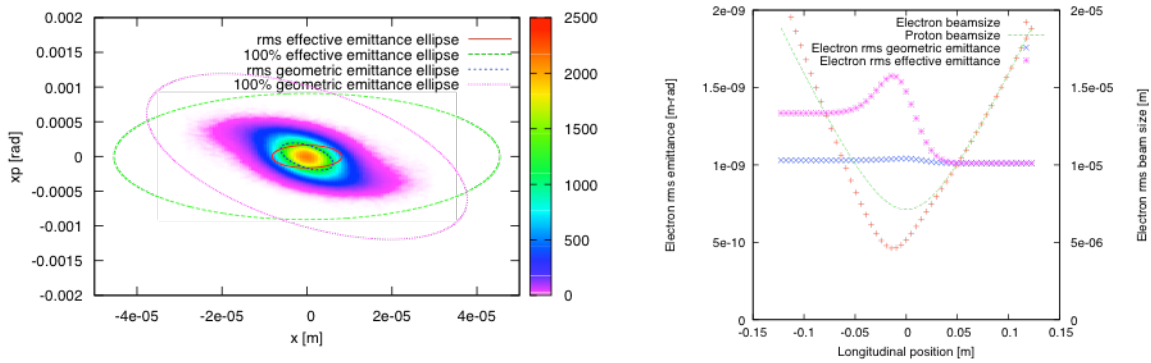


**Figure 2-53:** Left, electron beam distribution after the collision in transverse phase space ( $x$ - $p_x$ ); right, the electron beam parameter evolution in the opposing ion beam, e-beam travels from right to left.

The pinch effect describes the electron beam size shrinking in the interaction region due to the focusing beam-beam force, as shown in Figure 2-53. This effect will naturally boost the luminosity. For the design parameters, the pinch effect will boost the luminosity from  $1.1 \cdot 10^{33} \text{ cm}^{-2}\text{s}^{-1}$  to  $1.47 \cdot 10^{33} \text{ cm}^{-2}\text{s}^{-1}$ . However, this effect also enhances the local beam-beam force to the opposing ion beam, which needs careful dynamics aperture study (Figure 2-85).

For the ion beam, the largest challenge is the kink instability. The instability arises due to the effective wake field of the beam-beam interaction with the electron beam. The electron beam is affected by the head of the ion beam and passes the imperfection of the head portion to its tail. References [17] and [18] describe the instability in detail. The work in [18] predicts the threshold of the instability with two theoretical models (two-particle model and multi-particle circulant matrix model), as shown in Figure 2-54. The eRHIC parameter exceeds the threshold, therefore a fast (few thousand turns) deterioration of the ion beam is expected if no countermeasure is implemented. Simulations also indicated that the current chromaticity in RHIC cannot suppress the instability.

In reference [[18], an innovative feedback system is presented as an effective countermeasure. In this feedback system, one electron bunch will be slightly steered transversely based on the feedback information of the previous electron bunches after collision. These electron bunches interact with the same ion bunch. The feedback system can successfully suppress the kink instability in a cost effective way, since there is no RHIC modification required.

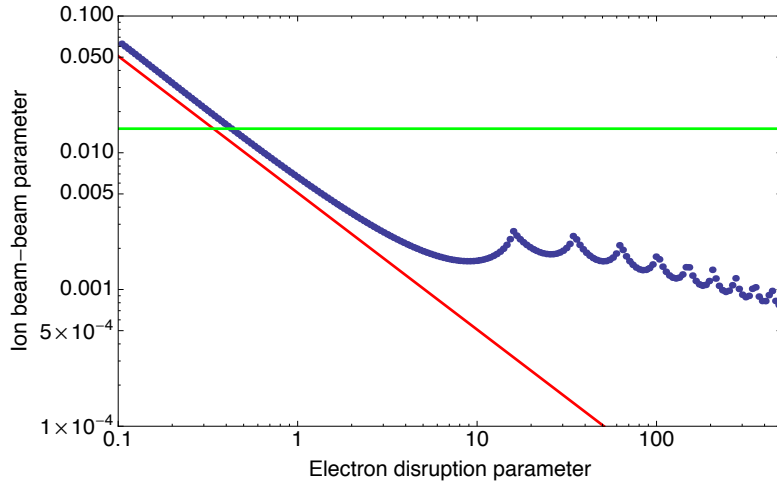


**Figure 2-54:** The threshold of kink instability, with choice of the synchrotron tune 0.004. The Blue dots denote the threshold calculated from macro-particles circulant matrix method. The red line represents the simple threshold form from simple two-particle model. The green line corresponds to the constant beam-beam parameter of 0.015, which is design beam-beam parameter of ion bunch in eRHIC.

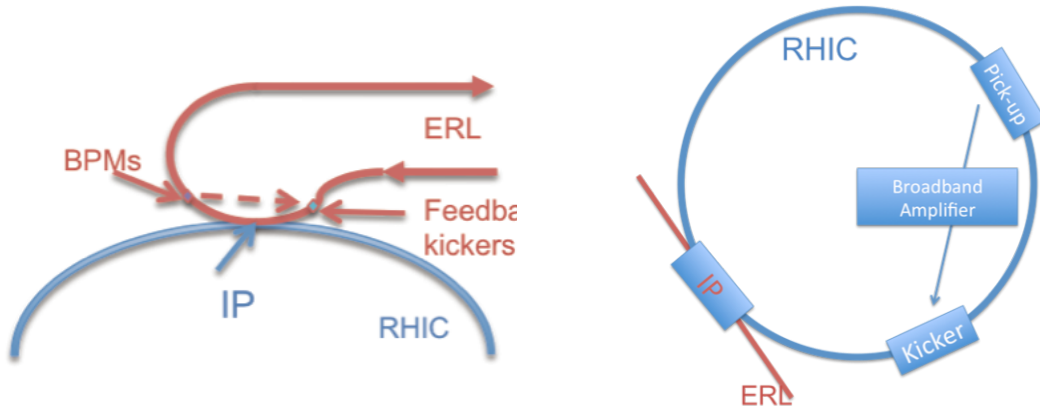


**Figure 2-55:** Left, dedicate feedback system of the electron accelerator to mitigate the kink instability; right, the pickup-kicker feedback system in RHIC for mitigating the kink instability.

An alternative traditional feedback system for the kink instability is also studied in [19]. It consists of a pickup, a kicker and the broadband amplifier between them. For the eRHIC parameters, the minimum bandwidth is determined as 50 MHz to 300 MHz from the simulation result.

The noise carried by the fresh electron beam may heat up the ion beam due to the beam-beam interaction. The random electron beam offset at the IP causes dipole-like errors for the ion beam, while the beam-size and intensity variation at the IP lead to quadrupole-like errors. The effects of both errors can be evaluated either theoretically or in simulation. The simulation shows that one-micron electron beam position offset at the IP causes an ion beam emittance growth of 20% per hour. The expected cooling time is much shorter than the emittance growth time. The same cooling time also allows the quad error of 0.1% (e-beam intensity or the beam size variation).

### 2.2.12 Beam Polarization

The polarized electron beam is produced from the polarized source, with a polarization of ~85-90%, and the task is to preserve this high polarization through the acceleration cycle up to the collision points. During the beam acceleration electron spin is oriented vertically in the recirculating passes. Since eRHIC experiments call for longitudinal polarization a spin rotator is inserted into the highest energy beam line. The spin rotator converts the vertical polarization of the

electron beam in the arcs to a longitudinal polarization at the experimental detector. The state-of-the-art electron spin rotator that was used in the electron-proton collider HERA (DESY, Germany) [20] was 56 m long. It employed a sequence of interleaved vertical and horizontal dipole magnets to transform the vertical spin of 27 GeV electrons to the required orientation in the horizontal plane. The vertical orbit excursion inside the spin rotator was quite large – about 20 cm – thus requiring some of the rotator magnets to be shifted vertically from the plane of the HERA electron ring.

**Table 2-13:** Spin rotator parameters.

Parameter		sol1	sol2
Energy range	GeV	5 – 10	10 – 20
Field integral range	Tm	26 – 53	52 – 105
Length (at 7 T)	m	7.6	15.0
Orbit angle from the IP	mrاد	92	46
Location in the RHIC tunnel		D9 – D10	D6 – Q8

The eRHIC spin rotators must operate over a large energy range, from 5 GeV to 20 GeV. Since the orbit excursion in the dipole magnets scales inversely with the beam energy, a HERA-type rotator leads to one meter orbit excursions of 5 GeV electrons. Further, the synchrotron radiation power (per meter) produced by 20 GeV eRHIC electrons is considerably larger than the 27 GeV electrons in HERA, due to the much large electron current. Reducing the linear power load requires further increasing the rotator length and, correspondingly, the vertical orbit excursion. Therefore, the only practical solution is a spin rotator based on strong solenoid magnets. Solenoidal Siberian Snakes have been used in electron accelerators operating in the 0.5 GeV to 1 GeV range [21]. The integrated longitudinal field necessary to rotate the electron spin by 90 degrees, from the vertical to the horizontal, is

$$BL [Tm] = 5.240 E [GeV]$$

A solenoid-based scheme for eRHIC using two rotators is shown in Figure 2-56. The first rotator (sol1) is used for operations in the 5 GeV to 10 GeV energy range. A second rotator (sol2) is also excited in the 10 GeV to 20 GeV energy range. The total spin rotation produced at any energy is 90 degrees. Each spin rotator contains two solenoids, and at least 5 skew quadrupoles to compensate for the betatron coupling and the vertical dispersion. Table 2-13 lists the main parameters of the rotators. The maximum field integrals of 53 Tm and 105 Tm can be realized by using superconducting magnets with fields in the 7 T to 10 T range. High-temperature superconducting technology might be used to produce even higher fields.

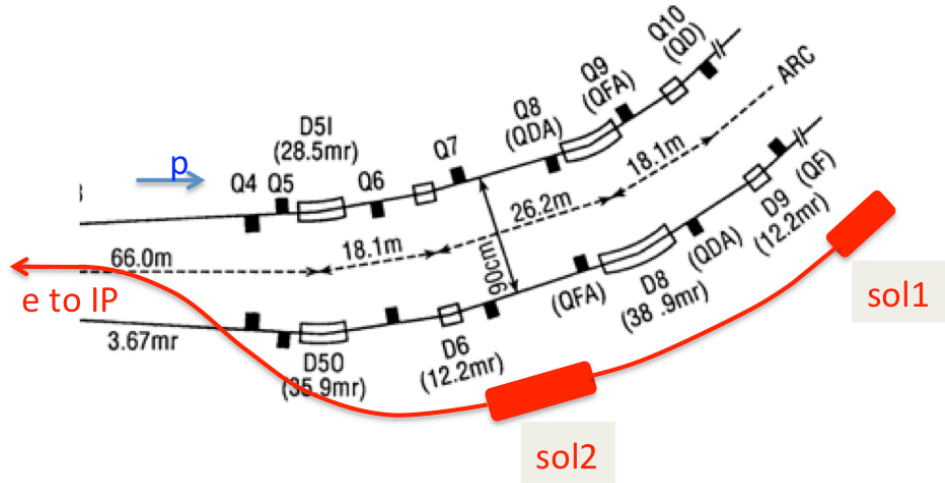


**Figure 2-56:** Layout of the electron spin rotators.

Perfect longitudinal polarization at the interaction point is only achieved at 7.5 GeV and 15 GeV, in the suggested scheme. Figure 2-57 shows the slight deviations of the polarization orientation that occur at other energies, with a worst case longitudinal spin projection reduction of 13%.

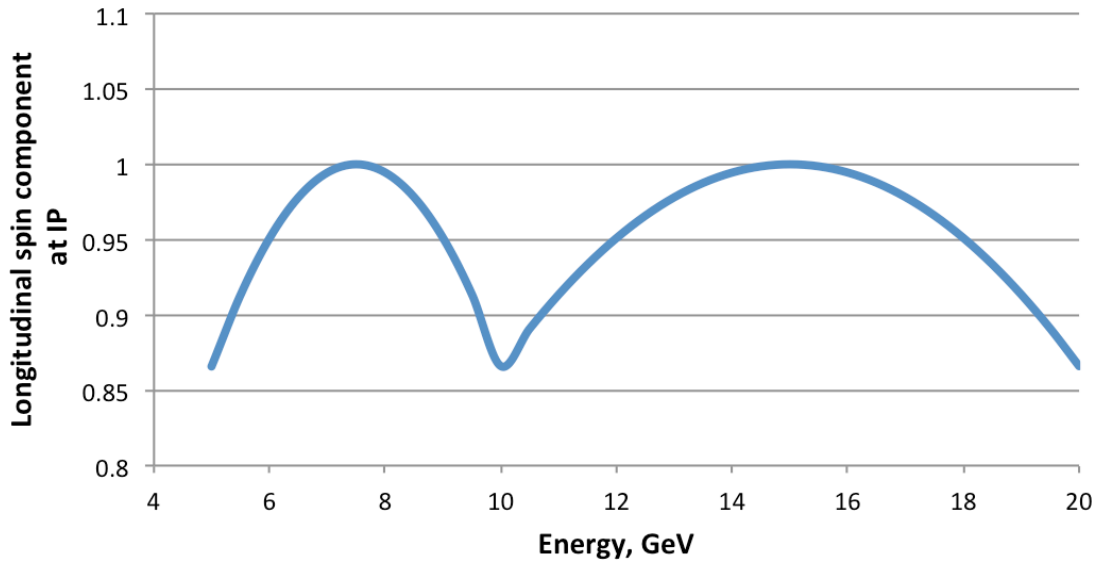


**Figure 2-57:** Deviation of the polarization orientation as a function of energy.

## 2.3 Hadron Beam Upgrades

### 2.3.1 Hadron Cooling

#### *Intrabeam scattering*

Small transverse and longitudinal beam emittances of the hadron beam in eRHIC are of critical importance, both for the attainment of high luminosity as well as for separating the products

scattered at small angles from the core of the hadron beam required for a number of golden experiments. However, these small hadron beam emittances result in limited beam lifetime of hadron beams due to the process of Intra-Beam Scattering (IBS) which result in rapid growth of transverse beam size and bunch length, as well as bunch intensity losses. To counteract growth of beam emittance due to IBS and to achieve required average per store luminosities some type of hadron cooling system is needed. The cooling techniques should assist in obtaining required initial transverse and longitudinal emittances and prevent their significant increase due to IBS.

Since for present hadron beam parameters various ratios between transverse and longitudinal temperatures of ion beam are being explored, especially with reduced transverse emittance, it is no longer accurate to use some high-energy approximation for the calculations of the IBS growth time. Thus, here we calculate the IBS rates with formulas valid for arbitrary ratio between ion beam temperatures using the Betacool code.

Table 2-14 lists beam parameters and calculated IBS growth times for nominal design parameters of protons at 50 and 250 GeV.

**Table 2-14:** Nominal parameters for eRHIC protons beams.

<b>Energy, GeV/n</b>	<b>50</b>	<b>250</b>
<b>Bunch frequency, MHz</b>	9.4	9.4
<b>Bunch intensity, <math>10^{11}</math></b>	0.5	2
<b>Rms normalized emittance, <math>10^{-6}</math> m</b>	0.5	0.5
<b>Longitudinal bunch area, eVs</b>	1.6	1.6
<b>RF frequency, MHz</b>	197	197
<b>RF voltage, MV</b>	9	6
<b>Rms momentum spread, <math>10^{-4}</math></b>	24	6.2
<b>Rms bunch length, cm</b>	21	16.4
<b>IBS growth time for longitudinal emittance (min)</b>	1462	80
<b>IBS time for horizontal and vertical emittance (min)</b>	28	22

### *Electron Cooling*

To counteract growth of beam emittance due to IBS and to achieve required average per store luminosities some type of hadron cooling system is needed. The cooling techniques should assist in obtaining required initial transverse and longitudinal emittances and prevent their significant increase due to IBS. This section discusses limitation and achievable cooling times with a well known technique known as electron cooling.

The traditional electron cooling system employed at a typical low-energy cooler is based on electron beam generated with an electrostatic electron gun in DC operating mode, immersed in a longitudinal magnetic field. The magnetic field is used for the transport of an electron beam through the cooling section from the gun to the collector. To cool protons at 250 GeV requires electron beam energy of 136 MeV. This makes the use of electrostatic acceleration unviable. RF acceleration of a bunched electron beam results in an electron transverse momentum spread which is much larger than in existing coolers. The large transverse temperature of the electron beam can be controlled with a strong magnetic field in the cooling section solenoid, making magnetized cooling an attractive approach. Another approach based on non-magnetized cooling can be also considered.

An estimate of cooling time can be obtained using simple expressions for the cooling force. For example, using the non-magnetized expression for the force, one can express cooling time in high-energy approximation for a given transverse beam emittance of hadron beam as:

$$\tau \propto \frac{A}{Z^2} \frac{\gamma^2}{4\pi r_p r_e n_e c \eta \Lambda_c} \left( \frac{\gamma \varepsilon_n}{\beta_c} \right)^{3/2}$$

where  $A$  and  $Z$  are the ion atomic and charge numbers,  $\gamma$  and  $c$  are relativistic factor and the speed of light,  $\beta_c$  is the beta-function in the cooling section,  $\eta$  is the length of the cooling region divided by the ring circumference,  $\Lambda_c$  is the Coulomb logarithm,  $r_e$  and  $r_p$  are the classical electron and proton radii,  $n_e$  is electron beam density in the laboratory frame, and  $\varepsilon_n$  is the normalized rms ion beam emittance.

A direct cooling at high energy very quickly becomes ineffective due to a very strong dependence of the cooling time on energy. Such shortcoming of electron cooling technique could be partially mitigated by pre-cooling at low-energy where cooling times are much faster. Subsequently, ions with pre-cooled small angular spread could be cooled much faster at higher energy, as can be seen from Eq. (1).

### Magnetized vs. non-magnetized cooling approach

The presence of a strong longitudinal magnetic field changes the collision kinetics significantly. The magnetic field limits transverse motion of the electrons. In the limit of a very strong magnetic field, the transverse degree of freedom does not take part in the energy exchange, because collisions are adiabatically slow relative to the Larmor oscillations. As a result, the efficiency of electron cooling is determined mainly by the longitudinal velocity spread of the electrons. Such cooling is typically referred to as “magnetized cooling”. The magnetic field value is determined by condition of electron “magnetization” – radius of the electron Larmor rotation in the transverse plane has to be much less than the beam radius.

When an rms velocity spread within electron beam is comparable or smaller than the spread within the ion beam and, and there is no requirement of getting ultra-cold ion state, the cooling can be done without the help of the strong external magnetic field. Such type of cooling is referred to as the “non-magnetized cooling”; although a weak external field can be still employed, for example, to ensure focusing and alignment of electron and ion beams. Electron cooling using the non-magnetized electron beam can significantly simplifies the cooler design. However, for non-magnetized cooling one needs to have the transverse rms velocity spread of the electron beam to be comparable to the one of the ions.

For eRHIC linac-ring parameters the emittance of hadron beam at top energy has to be about 0.5  $\mu\text{m}$ . As a result, for the non-magnetized cooling approach to be effective at top energy electron bunch emittance should not be much larger than 0.5  $\mu\text{m}$  as well. At the same time, requirement to provide cooling to compensate IBS of 22 min at 250 GeV requires electron bunch charges of about 36 nC for the non-magnetized cooling. Achieving such high charge electron bunches with emittance around 1  $\mu\text{m}$  appears to be very challenging.

Table 2-15 lists electron cooler parameter to compensate IBS growth times of 22 min at 250 GeV proton energy.

**Table 2-15:** Electron cooler parameters for non-magnetized cooling approach for 250 GeV protons.

	<b>p</b>
<b>Relativistic factor g</b>	266
<b>Length of cooling section, m</b>	120



<b>Bunch charge, nC</b>	36
<b>Rms normalized emittance, <math>10^{-6}</math> m</b>	1
<b>Rms bunch length, cm</b>	16
<b>Rms momentum spread, <math>10^{-4}</math></b>	5
<b>Cooling time longitudinal (min)</b>	13
<b>Cooling time transverse (min)</b>	23

Since cooling times are much faster at low energy, parameters of electron cooler at low energy are less demanding. For example, to maintain pre-cooled proton parameters at 50 GeV requires transverse cooling time of 45 min which can be achieved for the non-magnetized cooler:

**Table 2-16:** Electron cooler parameters for non-magnetized cooling approach for 50 GeV protons.

	<b>p</b>
<b>Relativistic factor</b>	56
<b>Length of cooling section, m</b>	120
<b>Bunch charge, nC</b>	12
<b>Rms normalized emittance, <math>10^{-6}</math> m</b>	2
<b>Rms bunch length, cm</b>	21
<b>Rms momentum spread, <math>10^{-4}</math></b>	5
<b>Cooling time transverse (min)</b>	45

The use of magnetized cooling does not have such strict requirement on transverse emittance of electron bunches. However, the disadvantage of magnetized cooling is that it requires higher than non-magnetized cooling electron bunch charge because the Coulomb logarithm for slow collisions, which determine efficiency of magnetized cooling, is relatively small. Another disadvantages of magnetized cooling are more technologically challenging electron beam transport as well as cooling section solenoids.

For example, to compensate IBS growth time of 22 min requires electron bunches with charges of 100 nC and cooling section of about 120 m covered by 3-4 T solenoids as summarized in Table 2-17.

**Table 2-17:** Electron cooler parameters for magnetized cooling approach for 250 GeV protons.

<b>Relativistic factor</b>	266
<b>Length of cooling section</b>	120
<b>Bunch charge, nC</b>	100
<b>Rms normalized emittance, <math>10^{-6}</math> m</b>	40
<b>Rms bunch length, cm</b>	16
<b>Rms momentum spread, <math>10^{-4}</math></b>	5

### Electron Cooler

We have designed an electron source, beam transport and energy recovery linac to accelerate 100 nC of charge to 147 MeV.

Figure 2-58 provides the injector layout which spans 10 m. Using an 84 MHz normal conducting RF gun submerged in a solenoidal field we accelerate 100 nC through five 84 MHz cavities which accelerate the beam to 2 MeV and leave it with a chirp for bunch compression. In addition, there are two 252 MHz 3<sup>rd</sup> Harmonic correctors.

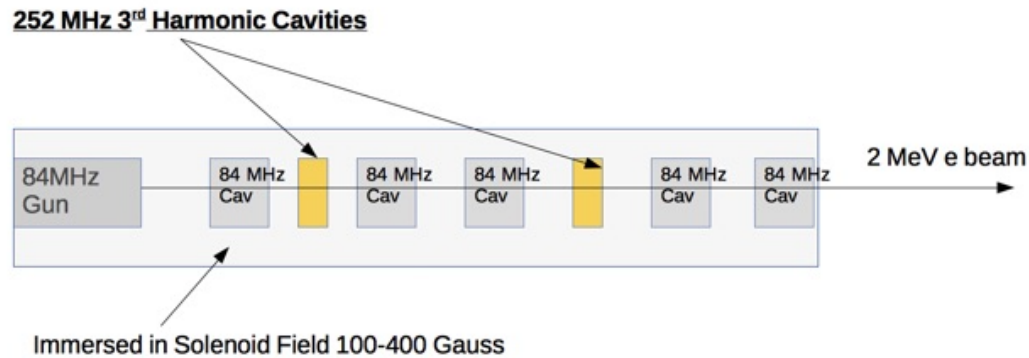


**Figure 2-58:** 2 MeV e-cooler injector layout.

This beam is then merged into an ERL line going through a four bending Chevron magnets passing two of 1 degree and two of two degree bends. After exiting the merging line the beam is de-chirped with a final 84 MHz cavity.

The beam is then accelerated through 8 sets of 3-cell 324 MHz SRF cavities, each with an energy gain of about 17 MeV. Then a second 971 MHz 3<sup>rd</sup> Harmonic cavity is used to flatten the energy distribution to achieve 70 nC of charge within fractional energy spread of about  $5 \cdot 10^{-4}$  with a bunch length of 10 cm. This line is merged into the main Hadron cooling line and propagated for 60 m 4 T solenoid field and then re-matched using three quadrupoles to a -3T over an additional 60 m. This beam distribution is held at 1.88 mm transverse rms through the solenoidal channels. At the exit of the cooling section the electrons are then taken through two 180 degree bend with a 5 m bending radius. This steers them out of the hadron beam line and returns them to the entrance of the linac to recover the energy. Figure 2-59 shows the ERL and cooling channel block diagram.

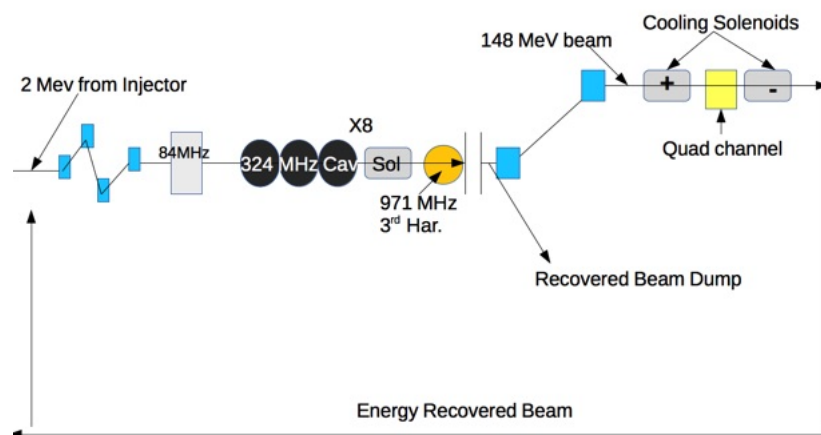


**Figure 2-59:** Layout of e-cooler ERL.

The RHIC tunnel layout allows a total of 191 m of straight section before reaching the arc bending magnets, providing sufficient space to fit the injector, 40m long ERL and 120 m long cooling section.

### Electron Cooler Solenoids

#### Requirements

The preliminary design of the solenoid required for electron cooling of eRHIC assumes that a solenoidal field of 3T is required in a bore of 100mm. The estimated good field region is about 3mm. The total length of the cooling section is estimated to be about 80m; in practice the cooling section would be made of several up to 10m long individual solenoids with matching sections in between.

The field within each of the solenoids needs to be highly parallel. In the good field region of about  $\pm 2$ cm radius the angle between transverse and longitudinal field should be smaller than 10  $\mu$ rad, which is equivalent to an axis-offset of less than 16  $\mu$ m.

To investigate the feasibility we assume a conventional NbTi solenoid with a radial thickness of about 5mm (four layers). The solenoid is supported by a steel tube with a radial thickness of 5mm as shown in Figure 2-60.

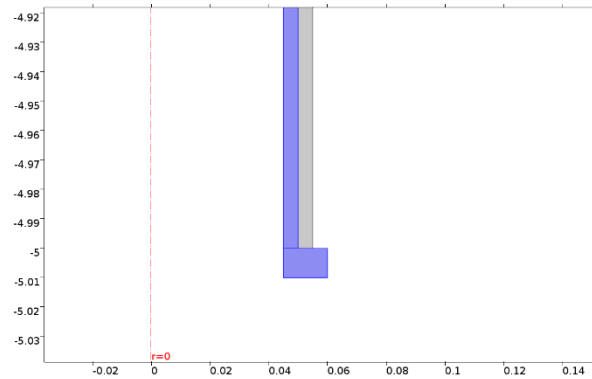


**Figure 2-60:** Preliminary design of e-cooler solenoid.

#### Field Angle

Figure 2-61 shows the angle between transverse and longitudinal field in a 10 m long solenoid. The figure shows that the requirements on field homogeneity in a perfect solenoid are met up to a length of  $\pm 4$ m.

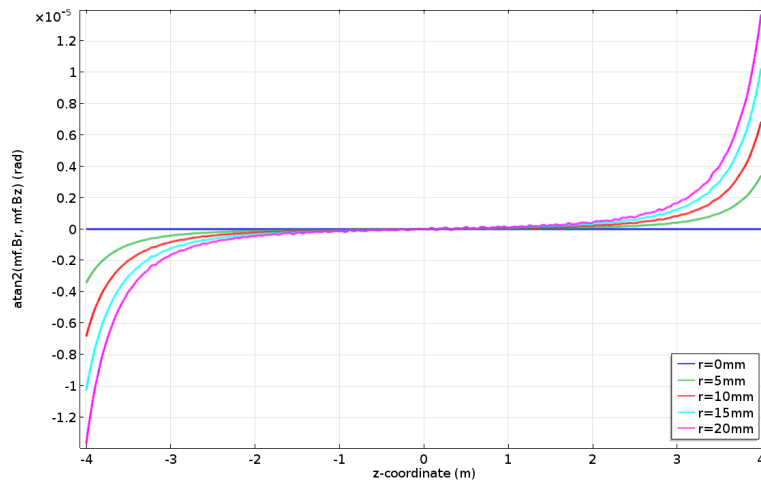


**Figure 2-61: Angle between transverse and longitudinal field in a perfect solenoid.**

### *Optimizing End Fields*

To improve the field quality of the solenoids trim coils can be added in the end region, which effectively increases the useful length of each solenoid. An example for this is shown in Figure 2-62. For this study we assume 5m long solenoidal sections with a gap of 250 mm between coils to allow for cryostats and end flanges.

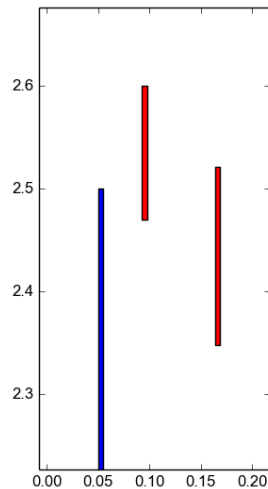


**Figure 2-62:** Trim solenoids (shown in red) can be added to improve field quality in the end region.

Using two trim solenoids at current densities of 3.19 A/mm<sup>2</sup> (outer) and 18.55 A/mm<sup>2</sup> (inner) the length of the good field region can be increased by 27% as shown in Figure 2-63 and Figure 2-64.

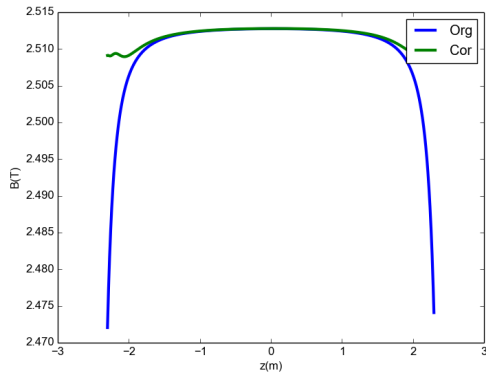


**Figure 2-63:** On-axis field of the corrected and uncorrected solenoid.

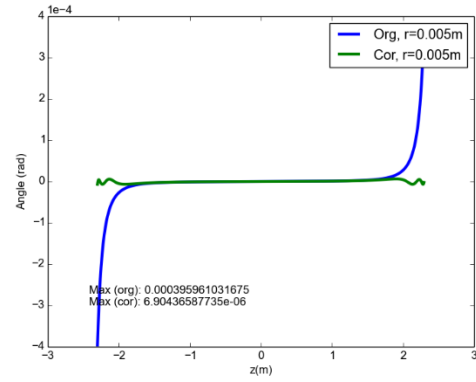


**Figure 2-64:** Angle between transverse and longitudinal field for the corrected and uncorrected solenoid.

### Matching Section

It is anticipated that the 80m long channel will consist of several 5-10m long individual solenoids for manufacturing reasons. In between two individual solenoids a matching section could be required, as the azimuthal kicks received in the end field region of two subsequent solenoids will not completely cancel. This is due to a slightly changed radius of the particle, leading to a slightly different opposing azimuthal kick.

To compensate for this a scheme [22] was developed, which consists of a single narrow end coil at the end of each solenoid. The details of the matching section will be the topic of a future study.

### Superconducting Magnet

It is anticipated that the solenoid will be made out of conventional NbTi superconductor. We assume a conductor with a cross-sectional area of  $1\text{mm}^2$  and a Cu:Sc ratio of 4:1. The stored magnetic energy in a 10m long section is 200kJ. The peak current in the conductor to achieve 2.5T is 400A. Figure 2-65 shows the loadline of the solenoid. As shown in the figure, the solenoid has an ample temperature margin of 1.8K if operated at 4.2K.

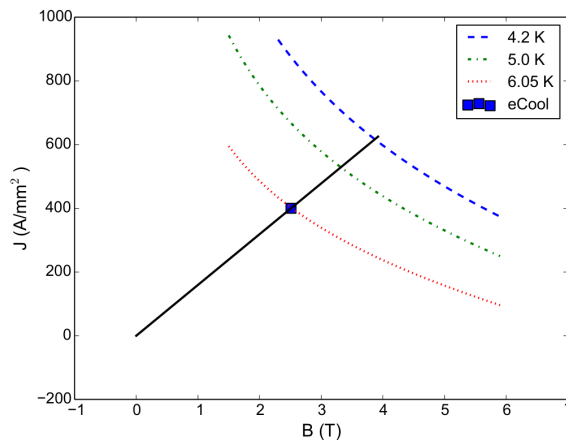


**Figure 2-65** Loadline of the eRHIC electron cooling solenoid.

The quench behaviour of the solenoid was estimated using XQuench [23]. The initial quench propagation velocity is evaluated to be 7.86 m/s. For a quench in the outermost corner of the solenoid the current is expected to decay in less than 4s. In the simulation the solenoid was protected with a  $2\Omega$  resistor. For this scenario the hotspot temperature stays below 125K, which is safe.

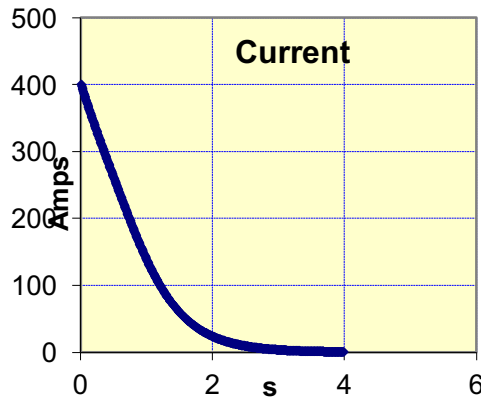


**Figure 2-66:** XQuench: Solenoid current.

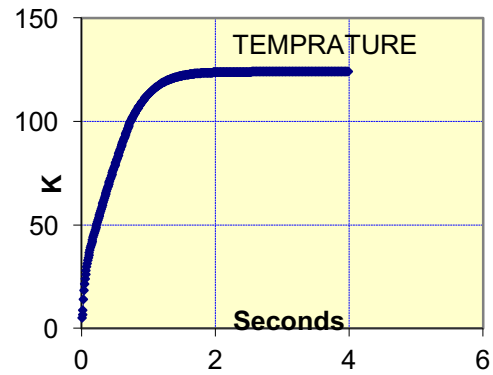


**Figure 2-67:** XQuench: Hotspot temperature.

### *Mechanical Considerations*

Based on initial finite element results (see Figure 2-68, which shows the deflection of solenoids different length if only supported by the ends) we anticipate that the solenoid will have to be supported every meter in order to meet the misalignment tolerance. A potential option to support the solenoid is the support belt system employed by MICE, which is shown in Figure 2-69. The advantage of this system is that glass fibre belts are used, which possess a very low thermal conductivity while at the same time being mechanically rigid. In principle it is possible to attach the support belts such that adjustments can be made after the cryostat has been assembled.

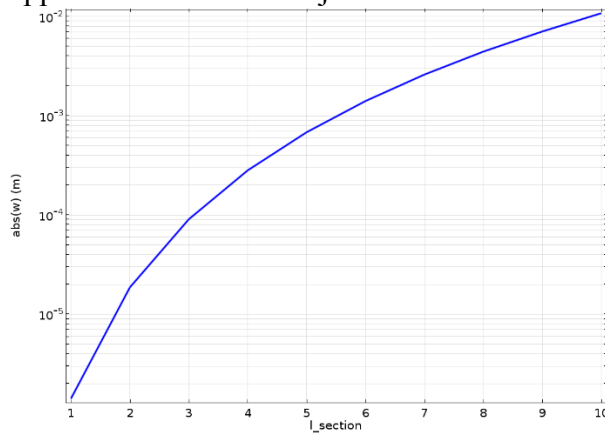


**Figure 2-68:** Deflection of a solenoid of variable length if supported only by the ends.

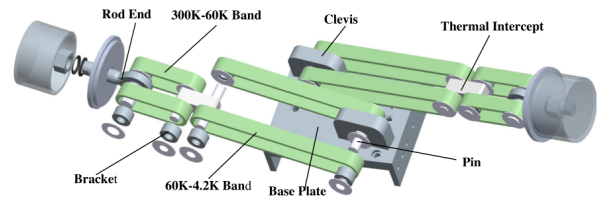


**Figure 2-69:** Double-band cold mass support assembly used in MICE [24].

An initial mechanical analysis shows that the stresses in the coil and support structure are not a concern (von-Mises stress  $< 25\text{MPa}$ ). The expected deflections of the solenoid due to the magnetic forces is likewise small (300 $\mu\text{m}$  in axial direction and 5 $\mu\text{m}$  in radial direction).

### *Summary*

The proposed electron cooling solenoid channel for eRHIC is challenging in terms of the required field quality. Existing electron lenses installed at Fermilab and BNL (see Figure 2-70 and Figure 2-71) are shorter, but have achieved similar field qualities as required for eRHIC. Notable in this respect is that the BNL eLens achieves the required field quality for RHIC ( $\pm 50\mu\text{m}$ ) without the use of corrector coils.

This is shown in Figure 2-72, which shows the achieved transverse offset in the existing BNL eLens. The figure shows that the BNL eLens possesses a good field region which is about 1.6m long, where the transverse offset is close to the eRHIC requirements. With the installed corrector coils a much better field quality can be anticipated. Solenoids longer than 3m will require modifications to existing winding equipment, but this seems feasible.

As shown in earlier sections, trim solenoids can be added to extend the good field region in the end region of each solenoid. A mechanical support system is necessary to support a solenoid which is several meters long. A support strap system can be used which can be tuned after magnet assembly. Corrector coils should be included in the design to improve the field quality.

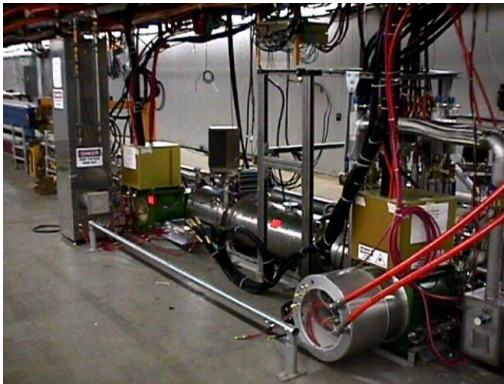


**Figure 2-70:** Fermilab eLens. The eLens is 2.7m long and can provide up to 6T.

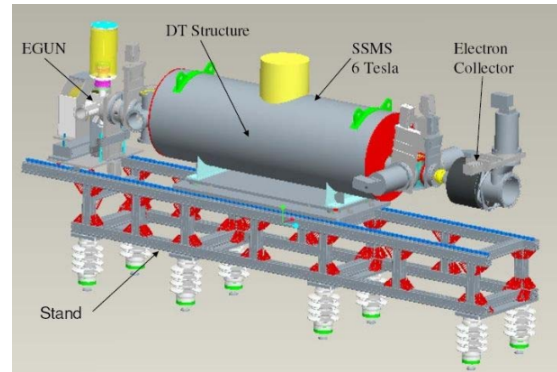


**Figure 2-71:** The 2m long BNL eLens.

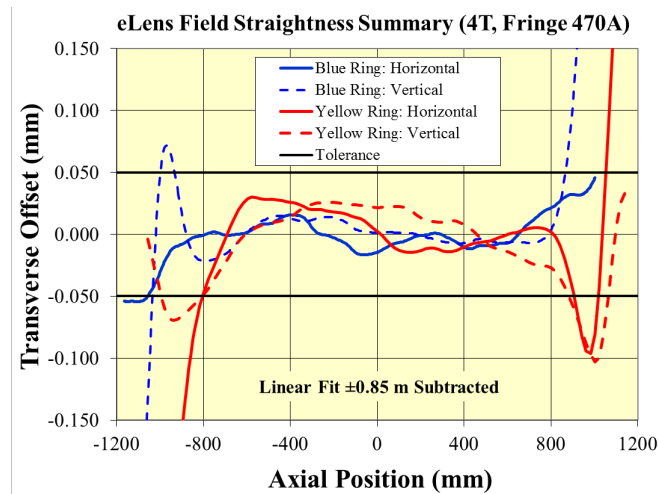


**Figure 2-72:** Transverse offset of the BNL eLens.

### **Coherent Electron Cooling**

Small transverse and longitudinal beam emittances of the hadron beam in eRHIC are of critical importance, both for the attainment of high luminosity as well as for separating the products scattered at small angles from the core of the hadron beam required for a number of golden experiments. Specifically, the eRHIC Ultimate design requires a 10-fold reduction in transverse and longitudinal emittance of the hadron beams, i.e. about a 1,000-fold increase in brightness, compared with beams currently operating in RHIC. There is no established cooling technique capable of this task. The stochastic cooling currently used at RHIC [25] falls a factor of about 100-1,000 short for



cooling ion beams to the required density and by a factor of  $\sim 10^4$  short for proton beam cooling. A detailed study of traditional electron cooling of RHIC beams [26] showed that its cooling time will also be insufficient for eRHIC Ultimate hadron beam parameters.

There are three advanced, but untested cooling methods: an optical stochastic cooling (OSC) [27], coherent electron cooling (CeC) [28] and recently suggested micro-bunching electron cooling (MBEC) [29], which in principle can satisfy the eRHIC's cooling requirements. Unfortunately OSC is incompatible with eRHIC's need to change the hadron beam energy 5-fold – it would require a 25-fold change of the undulator period in OSC. The two remaining techniques are versions of coherent electron cooling, with CeC theory developed in-depth and MBEC being a new and developing concept. Hence, we present here a CeC cooler as the main approach capable of cooling hadron beams in eRHIC to the designed emittances.

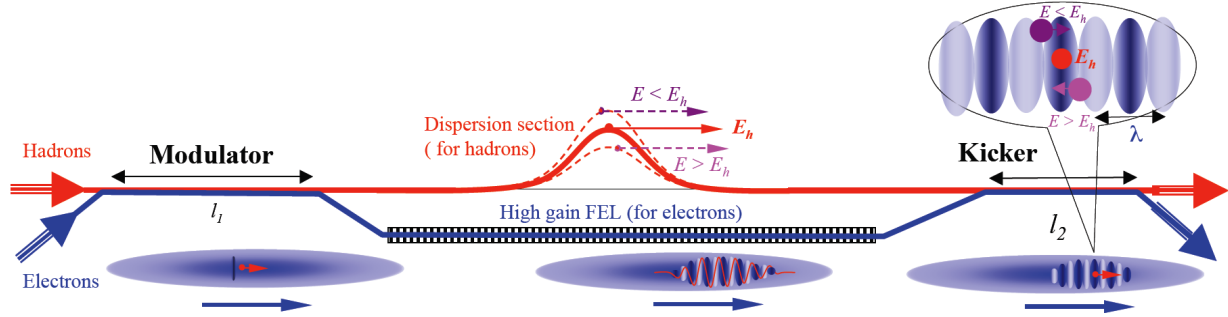


**Figure 2-73:** A general schematic of the classical Coherent Electron Cooler comprising three sections: A modulator, an FEL plus a dispersion section, and a kicker. For clarity, the size of the FEL wavelength,  $\lambda$ , is exaggerated grossly.

The CeC scheme, shown in Figure 2-73, is based on electrostatic interactions between electrons and hadrons that are amplified either in a high-gain FEL or by other means. The CeC mechanism bears some similarities to stochastic cooling, but with an enormous bandwidth of the amplifier. In CeC, the electron and hadron beams have the same velocity and co-propagate, in a vacuum, along a straight line in the modulator and the kicker; this is achieved by selecting the energy of electrons such that the relativistic factors of the two beams are identical. CeC works as follows: in the modulator, each hadron induces density modulation in the electron beam, which is amplified in the high-gain FEL; in the kicker, the hadrons interact with the beam's self-induced electric field and experience energy kicks toward their central energy. The process reduces the hadrons' energy spread, i.e. it cools the hadron beam. By coupling the longitudinal and transverse degrees of freedom, the cooling can be shared and the hadron beam cooled in three dimensions: longitudinally, horizontally and vertically.

With the eRHIC hadron beam parameters the emittance growth time caused by intra-beam-scattering (IBS growth time) is measured not in hours (as in current RHIC) but in seconds. Hence, the cooling should operate at collision energy (e.g. from 40 GeV/u to 250 GeV). Our analytical estimates show that hadron beams (both proton and ion) could be cooled to the required emittances and kept there using the CeC with the parameters listed in Table 2-18.

**Table 2-18:** CeC parameters for cooling a 250 GeV proton beam in eRHIC.

<b>Hadron beam</b>			
<b>Species</b>	p	<b>Beam energy, GeV</b>	250
<b>Particles per bunch</b>	$3 \times 10^{10}$ - $2 \times 10^{11}$	<b><math>\epsilon_n</math>, mm mrad</b>	0.2
<b>Energy spread</b>	$10^{-4}$	<b>RMS bunch length, nsec</b>	0.27
<b>Electron beam</b>			

<b>Beam energy, MeV</b>	136.2	<b>Peak current, A</b>	50
<b><math>\epsilon_n</math>, mm mrad</b>	1	<b>RMS bunch length, nsec</b>	0.27
<b>CeC</b>			
<b>Modulator length, m</b>	10	<b>Kicker length, m</b>	10
<b>FEL wiggler length, m</b>	9	<b><math>\lambda_w</math>, cm</b>	3
<b><math>\lambda_o</math>, nm</b>	422	<b><math>a_w</math></b>	1
<b>g, FEL gain used/max</b>	3/44	<b>CeC bandwidth, Hz</b>	$1.1 \times 10^{13}$
<b>Cooling time, hours</b>	0.12		

CeC theory has matured in the last 5-6 years and included all major effects in the modulator, kicker and FEL (including saturation). CeC simulations have also advanced to the stage where we can compute hadron screening and cooling by an inhomogeneous electron beam, including propagating through a modulator or a kicker with quadrupole focusing. A very detailed discussion of this progress as well as numerous references to publications about CeC can be found in [30].

### 2.3.2 Beam Dynamics

In the presence of an effective beam cooling, the RMS proton bunch length in eRHIC will be reduced from that of current RHIC runs at store. Together with the increased bunch intensity or bunch number (depending on the specific scheme), coherent instabilities could be a potential limitation for achieving desired machine performance. In this study, we use the tracking code, TRANFT, to investigate the coherent beam instabilities due to machine impedances for all three eRHIC schemes: the nominal linac-ring scheme, the ring-ring scheme and the ultimate linac-ring scheme. Table 2-19 and Table 2-20 show the beam parameters assumed in the simulations.

**Table 2-19: Proton beam parameters at injection energy (24 GeV).**

	<b>LR nominal</b>	<b>RR</b>	<b>LR ultimate</b>
<b>Bunch intensity</b>	2E11	3E11	3E11
<b>Number of bunches</b>	120	360	120
<b>Normalized emittance, RMS</b>	2.5E-6 m	2.5E-6 m	2.5E-6 m
<b>Bunch length, RMS</b>	75 cm	75 cm	75 cm
<b>RF frequency</b>	28 MHz	28 MHz	28 MHz

**Table 2-20: Proton beam parameters at storage energy (250 GeV).**

	<b>LR nominal</b>	<b>RR</b>	<b>LR ultimate</b>
<b>Bunch intensity</b>	2E11	3E11	3E11
<b>Number of bunches</b>	120	360	120
<b>Normalized emittance, RMS</b>	5E-7 m	2.5E-6 m	2.7E-7 m
<b>Bunch length, RMS</b>	16 cm	20 cm	5 cm
<b>RF frequency</b>	197 MHz	197 MHz	647 MHz

#### *Longitudinal Microwave Instabilities*

Longitudinal RHIC impedance used in the simulation include the measured 1.5 ohm inductive broad band impedance, the longitudinal space charge impedance and the resistive wall impedance

[31]. The broad-band impedance is modeled as a resonator with  $Q = 2$  and  $f_r = 2\text{GHz}$ . The low frequency formula is applied for the resistive wall impedance with the wall conductivity of  $1.7 \times 10^{-8} \Omega \cdot \text{m}$ , assuming the beam pipe is coated with copper. The longitudinal space charge impedance (negative inductance),  $|Z_{||,SC}/p|$ , is 1.5 ohm at the injection energy (24 GeV) and negligibly small at the storage energy (250 GeV).

**Table 2-21: Summary of longitudinal microwave instability thresholds at store energy (250 GeV).**

	LR nominal	RR	LR ultimate
<b>RF frequency</b>	197 MHz	197 MHz	647 MHz
<b>Required RF voltage (simulation)</b>	$\geq 0.3\text{MV}$	$\geq 0.3\text{MV}$	$\geq 5\text{MV}$
<b>Required RMS energy spread (simulation)</b>	$\geq 1.02 \times 10^{-4}$	$\geq 1.22 \times 10^{-4}$	$\geq 2.25 \times 10^{-4}$
<b>Keil-Schnell threshold (theoretical)</b>	$\geq 1.12 \times 10^{-4}$	$\geq 1.25 \times 10^{-4}$	$\geq 2.45 \times 10^{-4}$

Table 2-21 shows the simulation results of the minimal RF voltages required to avoid the longitudinal microwave instabilities at store. The energy spreads from simulations are also shown in Table 2-21, which are compared with the theoretical estimations obtained from the Keil-Schnell criteria. At injection energy, 0.4 MV from the 28 MHz RF systems are assumed and for all three eRHIC schemes, no longitudinal instabilities are observed from the simulations.

### **Transverse Instabilities**

The transverse impedances include the contributions from space charge, bellows, resistive wall, bpm's and abort kicker [32,33]. At the storage energy of 250 GeV, a slow transverse instability is observed from the simulations for both the linac-ring nominal scheme and the ring-ring scheme. As shown in Figure 2-74 for the linac-ring nominal design, the transverse coherence grows by a factor of two in the course of  $1\text{E}5$  turns (or 1.3 seconds) even if the multi-bunch kick is artificially turned off in the simulation. The transverse instability is significantly enhanced when the multi-bunch kick is turned on<sup>2</sup>. Similar results are also obtained for the ring-ring eRHIC scheme. It is also found from the simulations that increasing linear chromaticity is not effective in suppressing the observed instabilities. A possible mechanism for stabilizing the beam is by introducing amplitude dependent tune shift. In the simulation, we consider linear tune dependence of betatron amplitude, which can be introduced by octupole fields. The one turn betatron phase advance for protons reads  $\psi = \psi_0 + \xi_x \delta + J \cdot (d\psi/dJ)$ , where  $\psi_0$  is the betatron phase advance of the reference particle,  $\xi_x$  is the linear chromaticity,  $J$  is the action of the particle's betatron motion and  $d\psi/dJ$  is determined by the strength of the non-linear field. Table 2-22 shows the required amplitude dependent tune spread to suppress the transverse instability.

**Table 2-22: Required amplitude dependent tune spread to avoid transverse instabilities (250 GeV).**

<sup>2</sup> The simulation code, TRANFT, does not take into account the abort gap and hence the multi-bunch instability corresponds to the worst-case scenario.

	LR nominal	RR	LR ultimate
Required $d\psi/dJ$ , $m^{-2}$	$\geq 7000$	$\geq 500$	No instability
RMS action spread, $m^2$	$8 \times 10^{-8}$	$4 \times 10^{-7}$	No instability
Required amplitude dependent tune spread, RMS	$\geq 8.9 \times 10^{-5}$	$\geq 3.2 \times 10^{-5}$	No instability

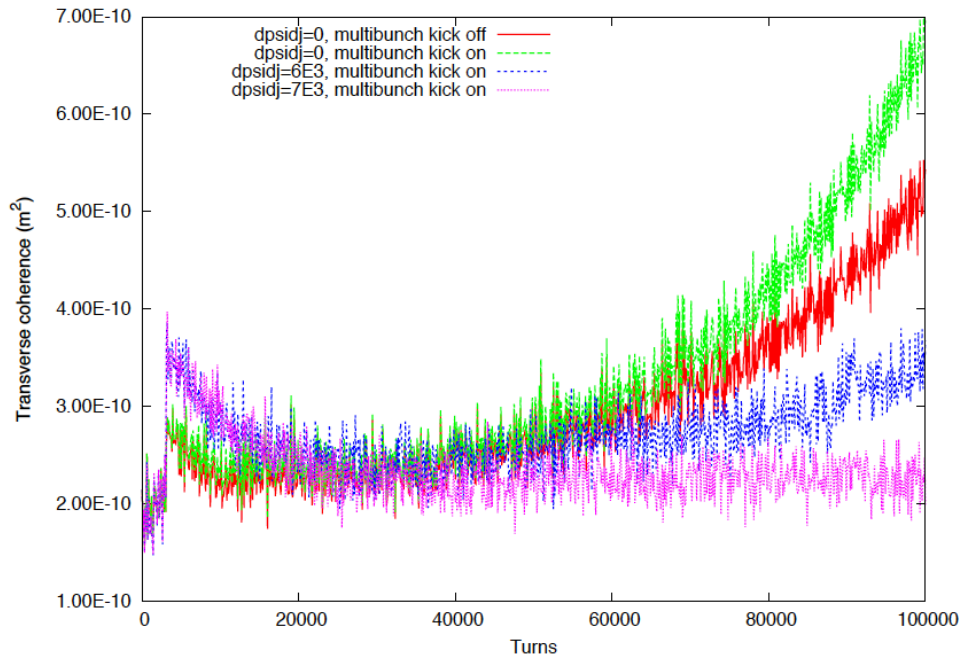


**Figure 2-74: Evolution of the transverse coherence for the linac-ring nominal design of eRHIC at store.**

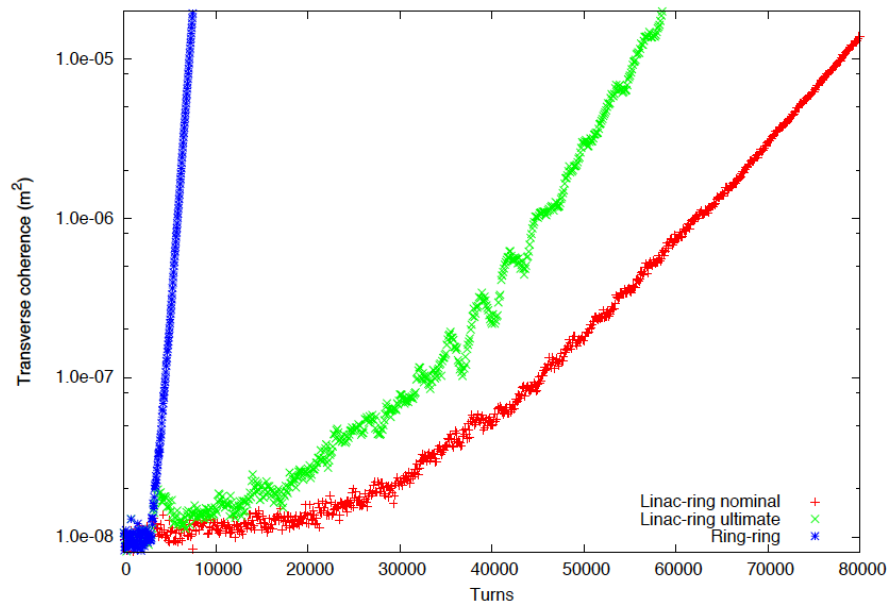


**Figure 2-75: Evolution of the transverse coherence for all three schemes of eRHIC at injection.**

For the linac-ring ultimate scheme, no transverse instability is observed from the simulation.<sup>3</sup>

At the injection energy of 24 GeV, transverse instabilities are observed from simulations for all three schemes as shown in Figure 2-75. Even after the multi-bunch kicks are artificially turned off in the simulations, the beams are still unstable. The instability can be suppressed by introducing the amplitude dependent tune spread induced by the  $d\psi/dJ$  term from octupoles. Table 2-23 shows the required RMS tune spreads in order to stabilize the transverse motion of the proton beam.

**Table 2-23: Required amplitude dependent tune spread to avoid transverse instabilities (24 GeV)**

	LR nominal	RR	LR ultimate
Required $d\psi/dJ$ , $m^{-2}$	$\geq 100$	$\geq 3000$	$\geq 2000$
RMS action spread, $m^2$	$4.2 \times 10^{-6}$	$4.2 \times 10^{-6}$	$4.2 \times 10^{-6}$
Required amplitude dependent tune spread, RMS	$\geq 6.7 \times 10^{-5}$	$\geq 2.0 \times 10^{-3}$	$\geq 1.34 \times 10^{-3}$

---

<sup>3</sup> In the previous study with similar parameters as the linac-ring ultimate scheme, the transverse coupled bunch instability (TCBI) is observed for the uncoated stainless steel vacuum chamber. With the copper coating of the beam pipe, the TCBI is sufficiently suppressed and no transverse instability is observed for the linac-ring ultimate scheme.

### 2.3.3 Beam pipe heating and copper coating

High wall resistivity in accelerators can result in unacceptable levels of resistive heating or in resistive wall induced beam instabilities [34]. This is a concern for the Relativistic Heavy Ion Collider (RHIC) machine, as its vacuum chamber in the cold arcs is made from relatively high resistivity 316LN stainless steel. This effect can be greatly reduced by coating the accelerator vacuum chamber with oxygen-free high conductivity copper (OFHC), which has conductivity that is three orders [35,36] of magnitude larger than 316LN stainless steel at 4 K. But, any coating has to prevent electron cloud formation that has been observed in many accelerators, including RHIC [37,38,39], which can act to limit machine performance through dynamical beam instabilities and/or associated vacuum pressure degradation.

Formation of electron clouds is a result of electrons bouncing back and forth between surfaces, with acceleration through the beam, which can cause emission of secondary electrons resulting in electron multipacting. Accelerator vacuum chambers and beam pipe surfaces with high enough secondary electron yield (SEY), whose typically maximum value  $SEY_{max} > 1.3$ , facilitate electron multiplication. Original plans were to add a second coating layer on top of OFHC of TiN or amorphous carbon (a-C) to reduce secondary electron yields [40,41]; but, later results [42] indicated that a-C has lower  $SEY_{max}$  than TiN in coated accelerator tubing. Nevertheless, new experimental SEY measurements indicated that there was no need to pursue a-C coating either; since well-scrubbed bare copper can have its  $SEY_{max}$  reduced [43] close to 1 ( $SEY_{max} < 1.3$  is needed to eliminate electron cloud problems). In essence copper coating can resolve the resistivity issue, and after scrubbing can reduce  $SEY_{max}$  below 1.3, i.e. detrimental effect of electron clouds can be marginalized.

Applying such coatings to an already constructed machine like RHIC without dismantling it is rather challenging task due to the small diameter bore (of 7.1 cm) with access points that are about 500 m apart. A device and technique were developed for *in-situ* coating of the RHIC cold bore vacuum tubes. Experiments proved that the device and technique could successfully be utilized to coat the RHIC cold bore vacuum tubes. But before embarking on the large task of coating RHIC, additional studies are needed to ensure that the expected benefits of coating the RHIC cold bore vacuum tubes with 10  $\mu\text{m}$  of copper are realized. In the non-cryogenic (warm) sections, of most accelerators including RHIC, where high resistivity is not an issue, the electron cloud problem was solved by using non evaporable getters [44] (NEG).

Since the RHIC geometry is very conducive to cylindrical magnetrons due to the length to radius ratio of the RHIC beam pipe, the choice of a long cylindrical magnetron, similar to that described by A.S. Penfold in reference [45]. Ideally, that cylindrical magnetron should be made as long as possible in order to coat sections as long as possible while minimizing or eliminating any need for cathode replacements. The RHIC cold section has varying curvature (with an overall curvature of approximately 1.8 mrad per meter), which does not limit magnetron length. But, mechanical constraint to prevent any sagging does limit the magnetron cathode length to 50 cm.

A 50-cm cathode magnetron mole was developed to in-situ copper coat cold bore RHIC tubes to alleviate unacceptable ohmic heating. The magnetron has a 50 cm long copper cathode, which is shown in Figure 2-76. The magnetron is mounted on a carriage with spring loaded wheels that successfully crossed bellows and adjusted for variations in vacuum tube diameter, while keeping the magnetron centered. The carriage can also be seen in Figure 2-76. Some deposition experiments were performed with spring loaded wheels on both sides of the magnetron, such that a set of wheels rolls over coated areas. No indentation in or damage to coating was observed, i.e. a train like assembly option for coating 500 meter RHIC sections without any interruptions is viable.



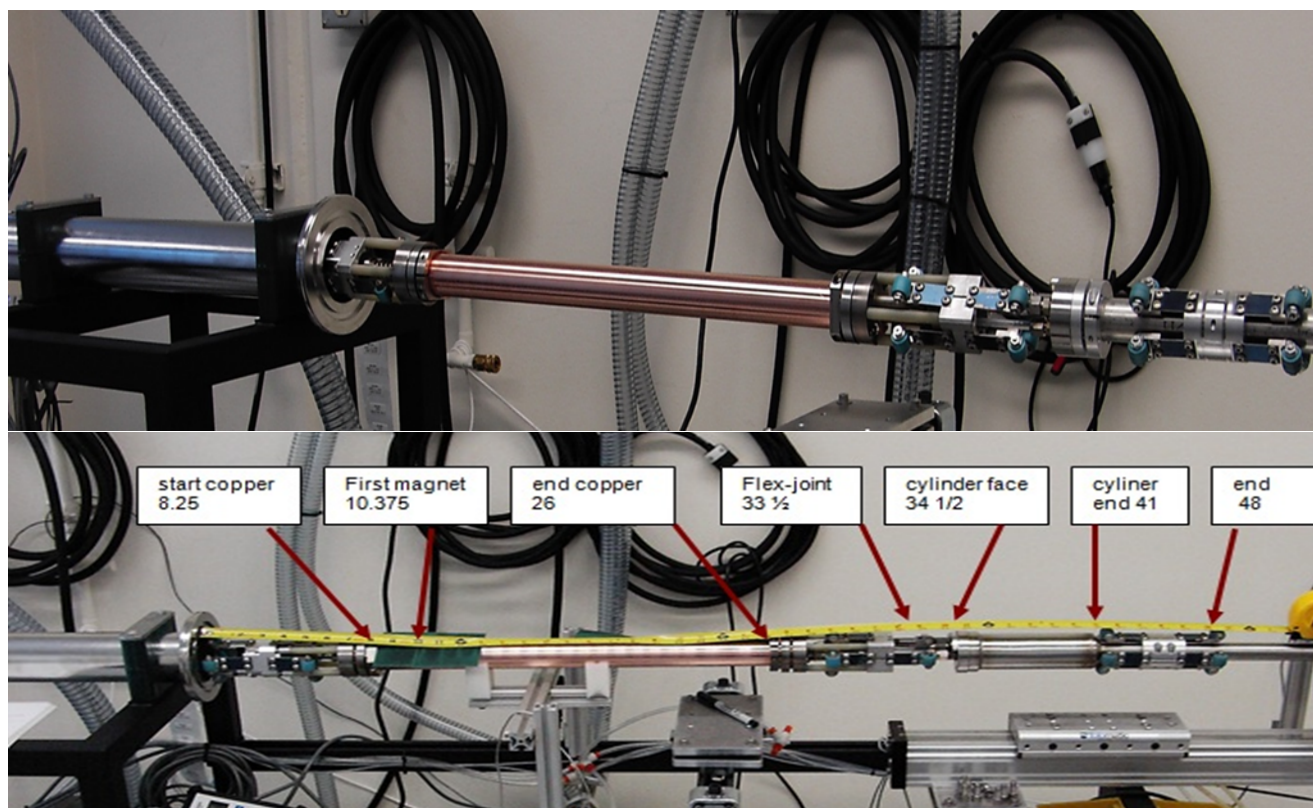


**Figure 2-76: Magnetron Coating Mole:** Top: 50-cm long cathode magnetron, spring loaded guide wheels that crossed bellows; adjusted for diameter variations keeping magnetron centered. Bottom: the 50-cm long cathode magnetron assembly.

Problems that needed to be overcome were developing deposition procedures that result in consistently good adhesion, and maximizing copper utilization. A procedure was formulated for achieving copper coating with excellent adhesion: first is application of a positive voltage (about 1 kV) to the magnetron or a separate cleaning anode and to move the discharge down the tube with a pressure of nearly 2 Torr. Second is a conventional deposition process at a pressure of about 5 mTorr.

To maximize copper utilization and minimize reloading needs, magnetron with moving magnets & thickest possible cathode is used, which reduces the target to substrate distance to less than 1.5 cm (unprecedented). Best moving magnetron magnet package moving mechanism was achieved by a miniaturized internal motor.

With the above magnetron mole and procedures, consistent coatings with excellent adhesion are achieved routinely. The optimized results yielded *adhesion strength of over 12 kg* (maximum capability pull test fixture) or at least  $2.9 \times 10^6 \text{ N/m}^2$ ; and copper utilization reached a remarkable 85%. An assembly of a RHIC magnet tube sandwiched between two types of RHIC bellows including a shielded bellow with additional sections of RHIC tubing were connected to each bellow for a total length of about 20 meters was successfully copper coated. Routine magnetron operation has coating rate  $0.0125''/\text{sec}$  or  $3.175 \times 10^{-4} \text{ meter/sec}$  in 500 W DC operation. Therefore, it would take  $1.57 \times 10^6$  seconds or 18.22 days of magnetron sputtering operation to coat a 500 meter long section of RHIC.

The magnetron assembly was mounted on a carriage (mole) pulled by a cable assembly driven by an external motor. The cable bundle, which is enclosed in 1 inch diameter stranded SS (or braided copper), contains electric power and water cooling feeds, as well as some instrumentation wires. Umbilical spool chamber and the cable assembly are under vacuum. Scaling the umbilical



motorized spool drive system to a 500 m cable bundle yields a system that is 3 meters or less in any dimension (plenty room in the RHIC tunnel). Pull cable will be  $\frac{1}{4}$ " diameter stranded SS, is typically used in aircraft for flexible linkage with the various airfoil surfaces; very strong (20K tensile) with low elongation.

Room temperature RF resistivity measurements were performed on 32 cm long RHIC stainless steel tubes coated with 2  $\mu\text{m}$ , 5  $\mu\text{m}$ , and 10  $\mu\text{m}$ , thick OFHC with a folded quarter wave resonator structure. Those measurements indicated that for the later 2 coatings conductivity was about 84% of pure copper. *Since joints and connectors reduce the experimentally measured  $Q$ , the conductivity value of coatings may be even closer to pure solid copper.* Computations indicate that 10  $\mu\text{m}$  of copper should be acceptable for even the most extreme future scenarios.

Nevertheless, the deposition technique must be modified, since at low temperatures, electrical conductivity is strongly affected by lattice imperfections and impurities. Room temperature conductivity is dominated by conduction band electrons, while at cryogenic temperatures, lattice defects and impurities scatter-off electrons causing large conductivity reduction. Ion assisted deposition (IAD) has been known to produce deposition with far superior qualities by establishing gradual transition between the substrate and deposited material resulting in denser more adherent film eliminating microstructure and increasing packing densities of optical coatings by an order magnitude. However, IAD requires simultaneous use of an evaporator and an ion beam source (too large for use in RHIC).

Future plans are to modify current deposition system to incorporate IAD; based on recent breakthrough IAD can be done with *End-Hall ion source*, which can be *miniaturized*; adapted for the mole. To minimize impurities, many of the deposition source components will be fabricated from the metal to be deposited. More details can be found in [46,47].

### 2.3.4 Space Charge Compensation

The electro-magnetic interactions among charged particles, the so-called space charge forces, play a significant role in modern accelerators. Although the space-charge force does not affect the frequency of the coherent dipolar motion of charged particle bunches as they circulate around the accelerator, it shifts higher order coherent motion frequencies, and may adversely affect the beam's stability. More importantly, this force usually is nonlinear, so introducing an additional tune spread to the circulating particles, and thereby increasing the beam losses due to the machine's non-linear resonances. The space-charge force falls quadratically with the beam's energy, and thus other nonlinear effects, such as beam-beam interactions, usually dominate high-energy colliders. However, future electron-ion colliders, such as eRHIC, are designed to operate with a range of energies. To avoid a significant reduction of the beam's lifetime at lower hadron energies, the bunch intensity must be reduced for low-energy operations.

It would be rewarding to reduce the effects of space charge without sacrificing the bunch's intensity; thus accelerator scientists are motivated to develop novel techniques for compensating for space charge. Techniques based on nonlinear compensating magnets, or the applications of neutralizing charge in an electron column (or electron lenses) have been investigated. However, these approaches face the common difficulty of over-compensation when applied to a bunched beam. In a charged-particle bunch, the space-charge force varies along the bunch, and consequently, without matching the compensation strength with the bunch's longitudinal profile, proper compensation to the bunch's center causes overcompensation at its tail. Recently, a scheme based on a bunched electron beam was proposed to compensate for space-charge effects for positively charged ion-bunches [48].

In this scheme, the electron bunches are launched in the same direction as the ion beam, while mismatching the energy of the compensating electron bunches from that of the circulating ion

bunches. This approach significantly lowers the electron beam's current required for space-charge compensation compared to that of the ion beam. In addition, for a given energy of the electron beam, the longitudinal profile of the electron bunches is tailored specifically so that space-charge compensation is optimized for the entire ion bunch.

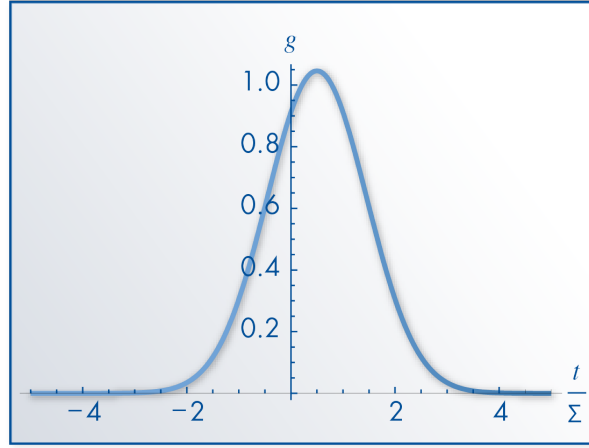


**Figure 2-77:** Longitudinal profile of the electron bunch required for compensating a positively charged ion bunch with a Gaussian distribution. The abscissa is the longitudinal location along the bunch in unit of R.M.S. bunch length, and the ordinate is the normalized electron instantaneous current.

### 2.3.5 Proton Polarization

The parameters for eRHIC proton beam is 70% polarization with  $3 \times 10^{11}$ /bunch and 0.2  $\pi$ mm-mrad normalized rms emittance. This emittance is at store and is expected to be cooled down by electron cooling. On the ramp, the emittance will be larger as delivered by AGS. The resonance strength associated with the larger emittance will be stronger. This section describes how the 70% polarization can be achieved based on current status of RHIC polarized proton operation and possible snake configuration changes.

#### *Current Status*

The current proton acceleration chain is shown in Figure 2-78. High intensity and high polarization  $H^-$  is produced from the polarized proton source. The  $H^-$  beam polarization is measured at the end of 200 MeV linac as 80-82%. The beam is then strip-injected into AGS Booster. The Booster vertical tune is set high so that  $0 + \nu_y$  intrinsic resonance is avoided. Two imperfection resonances are corrected by orbit harmonic correction. In the AGS, two partial Siberian snakes separated by 1/3 of the ring are used to overcome the imperfection and vertical intrinsic resonances [49]. The vertical tune on the energy ramp is mostly above 8.98, so that it is in the spin tune gap and away from the high order snake resonances. To avoid the horizontal intrinsic resonances driven by the partial snakes, a pair of pulsed quadrupoles are employed to jump cross the many weak horizontal intrinsic resonances on the ramp [50]. Two full Siberian snakes are used in each of the two RHIC rings to maintain polarization [51]. The betatron tune, coupling and orbit feedback on the energy ramp are also crucial for polarization preservation.

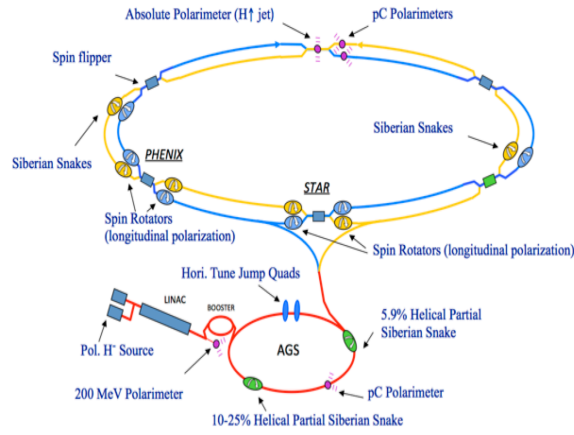


**Figure 2-78:** Layout of current RHIC complex for polarized protons.

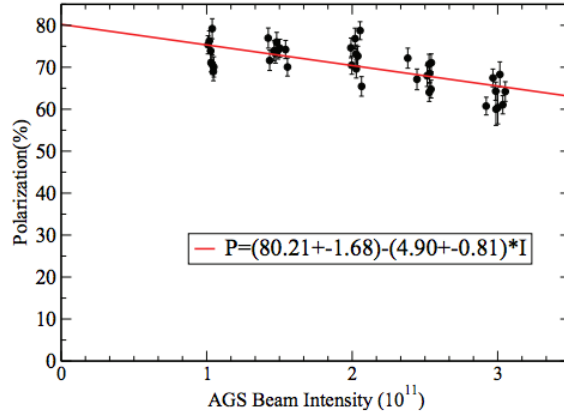


**Figure 2-79:** AGS polarization at extraction as function of bunch intensity. The polarized proton source can deliver intensity of  $9 \times 10^{11}$  at the Booster input. Booster scraping (both horizontal and vertical) is used to reduce the beam emittance for AGS injection. The intensity is changed by varying the Booster scraping level.

The polarization measured at the AGS extraction is shown in Figure 2-79 as function of beam intensity. The intensity was reduced by Booster scraping. The polarization dependence on intensity is really dependence on emittance. As higher intensity is always associated with larger emittance, and consequently stronger depolarizing resonance resonance strength, lower polarization is expected for higher intensity. As shown in Figure 2-79, the polarization at  $3 \times 10^{11}$  is about 65%. The AGS Ionization Profile Monitor (IPM) can measure beam emittance but the measured beam size is affected by space charge force. To mitigate the effect, the RF is turned off at flattop. The emittance reported by IPM with RF off is plotted in Figure 2-80. Since there is possible emittance growth in the Booster and mismatch in the transfer line, the projected emittance with zero intensity is not zero.

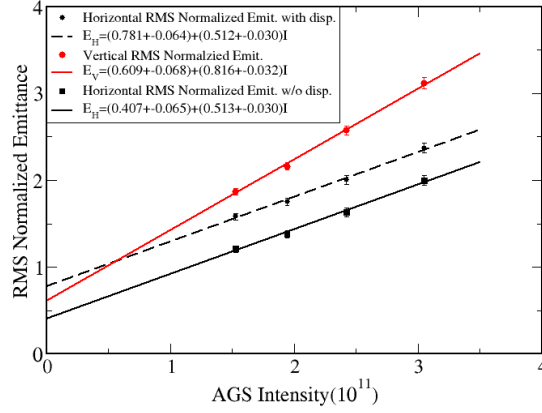


**Figure 2-80:** AGS emittance measured by IPM vs. intensity at the AGS extraction. The dispersion is not zero at the location of IPM. The horizontal emittance without dispersion contribution is derived based on measured dp/p and model dispersion.

At  $3 \times 10^{11}$ , rms normalized vertical emittance is about  $3\pi$ , rms normalized horizontal emittance is about  $1.8\pi$ . These are emittances we are going to deal with on the energy ramp. As the running experience shows, the polarization transmission efficiency up to 100 GeV in RHIC is close to 100% but about 85% for 250 GeV and  $1.8 \times 10^{11}$  bunch intensity, due to stronger intrinsic resonances. The intrinsic resonance strength can be calculated from DEPOL [52]. The results are shown in Fig. 4.

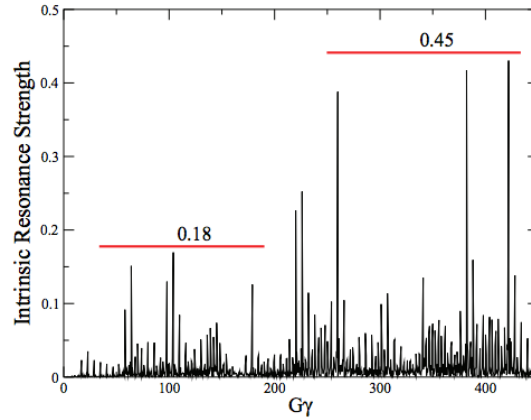


**Figure 2-81:** The intrinsic resonance strength of RHIC lattice for a particle on a  $10\pi$  normalized emittance invariant. Below 100 GeV, the resonance strength is less than 0.18. To accelerate proton beam to 250 GeV, the stronger resonance strength of 0.45 has to be overcome.

As Figure 2-81 shows, the highest resonance strength for particle on  $10\pi$  normalized emittance invariant is about 0.18 below 100 GeV and is about 0.45 beyond 100 GeV. The resonance strength threshold for full polarization preservation with two snakes may lie between 0.18 and 0.45. In the electron-ion collider stage, only one hadron ring is needed. In this case, the spin manipulating devices in both hadron rings can be used in one ring. Six snakes can be made from combining four existing snakes into one hadron ring, and reconstructing additional two snakes from spin rotators. In this case, six snakes will be available in the hadron ring. As a rule of thumb, the resonance strength threshold should increase by the same factor as number of snakes. Since the real resonance threshold is unknown, simulations are needed to see if polarization can be preserved for six-snake case.

## Spin Simulations

To estimate the polarization transmission efficiency on the ramp, spin tracking was done for one of three strongest resonances  $411 - \nu_y$  with ZGOUBI code [53]. The tracking were done for 8 particles on  $\sigma = 2.5\pi$  vertical emittance ellipse. To speed up the tracking, the acceleration is 7 times of normal acceleration rate. It should be noted that with snake inserted, polarization loss is not sensitive to resonance crossing speed. Only vertical betatron motion is included in the simulation. For comparison purpose, the simulations are also done for 2-snake case. The results are shown in Figure 2-82. As shown inFigure 2-82, the 2-snake is not enough to preserve polarization for beam particles outside normalized rms emittance  $2.5\pi$ .

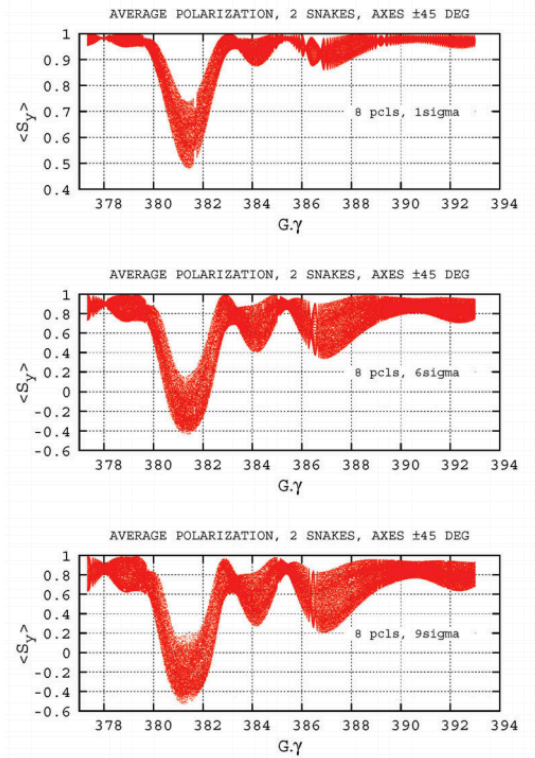


**Figure 2-82:** Spin simulation results for 2 snakes, snake axis as  $\pm 45$  degrees. From top to bottom, the vertical invariant is  $\epsilon_y = 1, 6, 9\sigma$ , with  $\sigma = 2.5\pi\text{mm.mrad}$  normalized emittance. Each plot shows the average vertical projection of the spin, computed from the tracking of 8 particles evenly distributed on the invariant. The horizontal invariant is negligible. The polarization is preserved for the  $2.5\pi\text{mm.mrad}$  case, but not the realistic large emittance case.

For multiple snakes scenario, the snake arrangement has to satisfy the condition for energy independent spin tune, namely

$$\sum_{k=1,3,5} \theta_{k,k+1} = \pi, \quad \sum_{k=2,4,6} \theta_{k,k+1} = \pi.$$

The axis angles are at  $\phi = \pm 45^\circ$  from longitudinal axis in the local Serret-Frenet frame, so ensuring respectively  $Q_s = 3/2$ , following

$$Q_s = \frac{1}{\pi} \left| \sum_{k=1}^{N_s=6} (-)^k \phi_k \right|.$$

Not all snake arrangements satisfying above conditions will preserve polarization. However, a simple arrangement with the six snakes equally spaced by  $2\pi/6$  can preserve polarization. The simulations with ZGOUBI are also done for 6-snake configuration and the results are shown in Figure 2-83. It shows that the polarization is preserved for the small and large emittance cases.

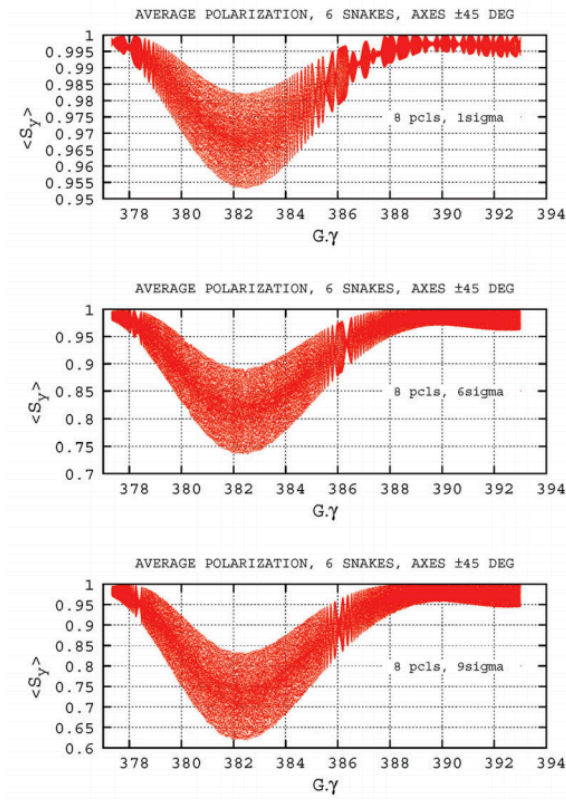


**Figure 2-83:** The simulation results for 6 snakes, snake axis as  $\pm 45$  degrees. From top to bottom, the vertical invariant is  $\varepsilon_y = 1, 6, 9\sigma$ , with  $\sigma = 2.5\pi\text{mm.mrad}$  normalized emittance. Each plot shows the average vertical projection of the spin, computed from the tracking of 8 particles evenly distributed on the invariant. The horizontal invariant is negligible. The polarization is preserved for all cases.

### Summary

In run13, proton beam reached 60% polarization for experiments at 250 GeV for collisions with  $1.8 \times 10^{11}$  bunch intensity [54]. Currently, AGS can deliver 65% polarization with  $3 \times 10^{11}$ . The additional gain in AGS polarization will come from vertical emittance preservation in AGS, so that the resonance strength can be reduced. A new electron collecting IPM has been added to measure emittance in the AGS, in particular to measure the injection turn-by-turn emittance for possible emittance growth due to injection mismatch. At 250 GeV, with 6-snake configuration, the polarization transmission efficiency is close to 100% in RHIC. Spin simulations with multi-particles and 6-D distribution for real acceleration rate will follow. The optics in RHIC is also important to control possible emittance growth at injection and on the ramp. All of these then can lead to smaller emittance and higher polarization required by eRHIC. The additional emittance reduction will be done by electron cooling.

## 2.4 Interaction Region Design

### 2.4.1 Interaction Region Overview

The main features of eRHIC interaction regions (Figure 2-84) are:

- Low  $\beta^*$ : 5 cm in the Ultimate design and 12.5 cm in the Nominal design



- 10 mrad crossing angle and the crab-crossing scheme
- Magnets of hadron IR focusing triplets are large aperture superconducting magnets
- First magnet (the hadron quadrupole) is located at 4.5 m from the collision point, outside the detector.
- Detector components for registration of neutral and charged particles are placed near the forward hadron beamline.
- Arranged free-field electron pass through the hadron triplet magnets
- Gentle bending of the electrons to avoid the synchrotron radiation impact on the detector

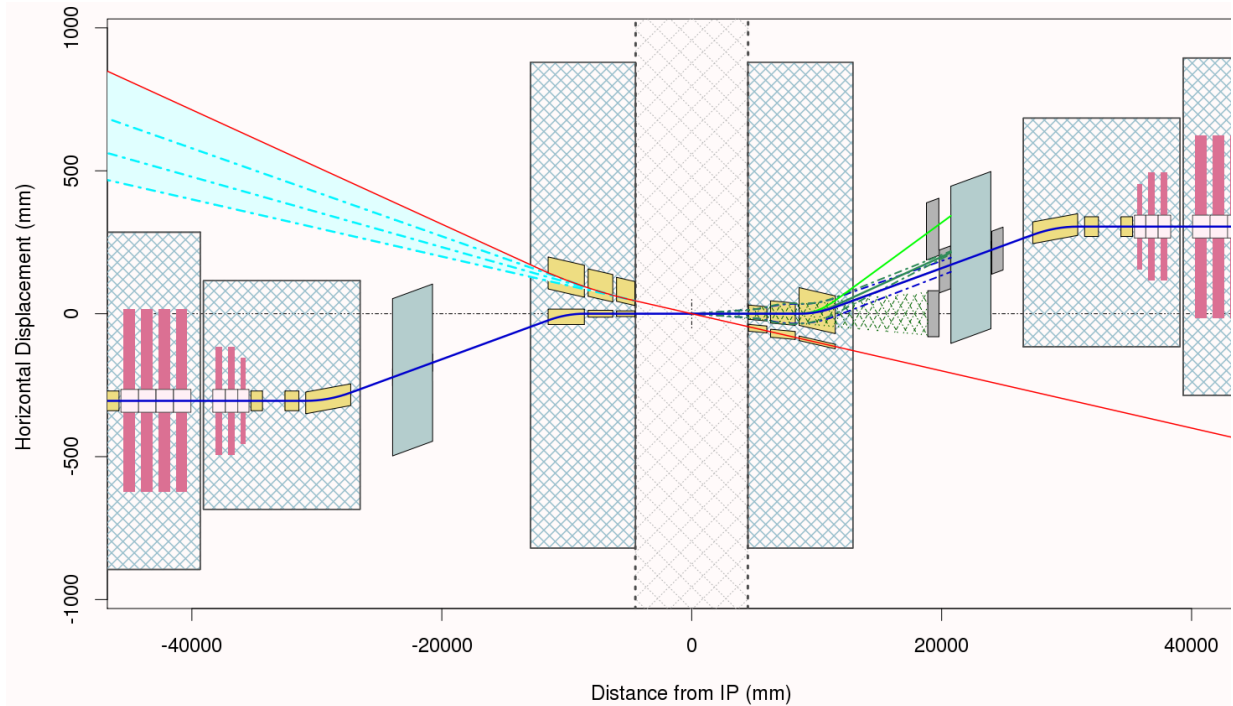


**Figure 2-84:** eRHIC interaction region layout. (the view from above)

The experimental requirements for the detection of forward propagating products of the collisions impact the IR design significantly. In the outgoing hadron beam direction, the IR magnets have to have enough aperture to pass the forward neutrons and forward scattered protons with a typical angle spread on the scale of  $\pm 10$  mrad. In the outgoing electron beam direction arrangements have to be done to tag the scattered electrons with small scattering angles (25-35 mrad).

### 2.4.2 Hadron IR Beamline

$\beta^* = 5$  cm is required for the high design luminosity in the Ultimate design. In the IR lattice design this small  $\beta^*$  is realized in two steps. First, the interaction region quadrupoles are designed to provide a strong focusing which allows to achieve  $\beta^*$  as low as 10 cm. Then, the squeeze from 10 cm to 5 cm is realized by introducing betatron waves in both planes, using the Achromatic Telescope Squeezing technique [55]. The eRHIC hadron lattice has a phase difference of  $90^\circ$  per cell in the arcs. The betatron wave is created by changing the quadrupole gradients ( $\Delta G = 7\%$  with



respect to the regular arc quadrupole gradients) in two quadrupole pairs at the beginning of the arc before the IP.

24 families of sextupoles in the 90° degree lattice are able to correct the first and higher orders of chromaticities in the eRHIC lattice. The sextupole strength can be optimized also to minimize the lower order resonance driving terms. The resulting dynamic aperture (for the IR lattice variant with  $\beta_{max} \sim 2200$ ) obtained in the presence of the machine errors as well as beam-beam interactions is shown in Figure 2-85. Machine errors include 0.2% quadrupole and sextupole field errors and 100 microns magnet misalignments. At the momentum spread of the cooled hadron beam of  $\sim 2 \cdot 10^{-4}$ , the sufficient dynamic aperture of  $10\sigma$  has been demonstrated. Further improvement may be expected from careful choice of the machine working point.

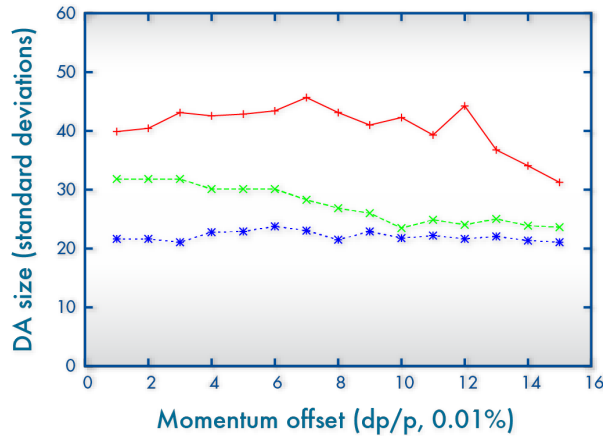


**Figure 2-85:** A plot of the optimized off-momentum dynamic aperture for eRHIC. The top curve (red, +) is the bare lattice, the middle curve (green, x) is with a beam-beam parameter of 0.015, and the bottom curve (blue, \*) is with beam-beam and gradient errors

The main features of the IR superconducting magnets, forming the hadron IR triplet, include the large aperture, needed to pass through the forward momentum collision products, and near field-free region arranged for the electron beam passage through the magnets. Figure 2-86 shows how the electron passage is arranged through the magnet area between the coils of hadron IR magnet. The extended low field “sweet spot” is made by combination of fields produced by main, middle and outer coil structures and passive shielding.

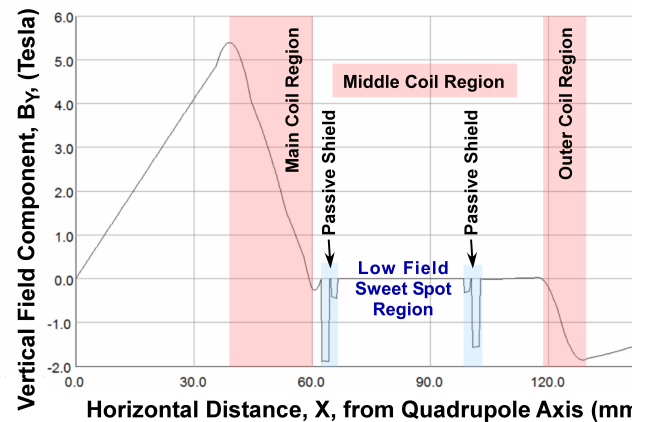
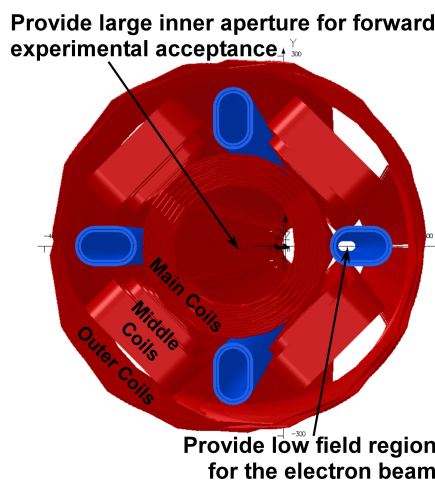


**Figure 2-86:** Left plot: the 3d coil profile with the various coil windings and apertures identified; Right plot: the field profile generated at the middle of the magnet.

### 2.4.3 Electron Beamline

The beam is extracted into the highest energy beamline in the spreader area. This beam line runs around all RHIC tunnel circumference. In the interaction region area the highest energy beamline brings the electrons to the experimental detector along its axis and focuses the beam to small  $\beta^*=5$  cm (in Ultimate design) at the collision point. The beamlines upstream and downstream of the detector have a similar magnet and lattice structure.

The top energy beamline consists of two parts, determined by their functions. The first part, the vertical shift beamline transports the top energy electron beam over the hadron ring magnet line and down to the level of the detector center axis. This beamline is ~55m long and the bending is done with relatively strong magnetic field (0.081 T at 20 GeV).

The second part of the top energy beamline, the IR beamline, that is ~60m long, provides the final weak bending to put the electron beam exactly on the detector axis. The focusing magnets, including the final focusing triplet, provide  $\beta^*=5$  cm at the collision point. This beamline contains the bending magnets with the field from 105 to 16 Gs at 20 GeV beam energy. Using the 16 Gs dipole magnets for the final bending produces a very low intensity soft synchrotron radiation, which does not create problems at the detector. The optical functions of the IR beamline are shown in Figure 2-87.

Since there are no strong bending magnets within 60 m from eRHIC detector, there are no strong synchrotron radiation sources near the experimental detector. The forward radiation coming from the upstream hard bend is completely masked and no hard radiation passes through the detector. Only soft bending is present in the vicinity of the detector. The forward radiation from the upstream soft bend passes through the detector but cannot penetrate through the beam pipe. The secondary backward radiation induced by the forward radiation generated in downstream bends can be mostly masked from entering the detector area.

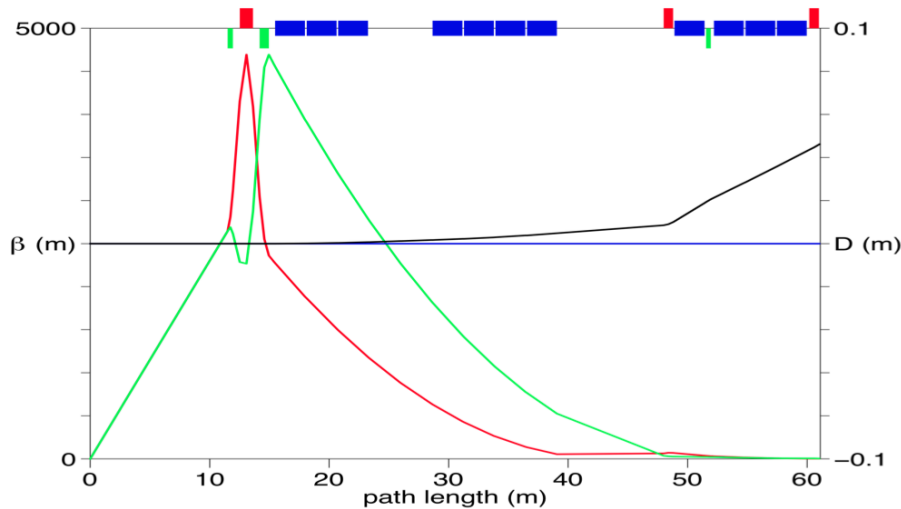


**Figure 2-87:** The horizontal (red) and vertical (green) beta-functions, and the horizontal (blue) and vertical (black) dispersion functions of the electron IR beamline. The collision point is located at 0 of the horizontal axis.

### 2.4.4 Crab-Crossing

Since the interaction region employs 10 mrad crossing angle between electron and hadron beams, the crab-crossing scheme is required to avoid more than an order of magnitude of luminosity loss. Crab cavity is required to establish crab crossing scheme in eRHIC. Ideally it should provide transverse kick which is linearly proportional to its relative longitudinal position within the bunch and form a tilting angle of half of the crossing angle on both colliding beams to compensate crossing angle. As a result, the two beam will collide equivalently to the head-on collision. The crab cavities are placed on both sides of the interaction region area to ensure that the beam rotation does not propagate to the outside of the interaction region.

If the bunch length is comparable with the wavelength of the crab cavity, the sinusoidal form of the crab-cavity voltage leads to the transverse deviation of particle at the head and tail of the bunch from the perfect linear x-s correlation. This nonlinearity not only leads to the luminosity loss, but also induces transverse kicks to the both beams which depend on the longitudinal position. The longitudinal dependent kicks together with the beam-beam interaction may reduce the dynamic aperture of the ion beam as well as induce emittance growth. The effect is more pronounced in the Nominal Design since the bunch length of the ion beam is longer.

Before detailed simulation with the crab cavity, we use luminosity degradation parameter to quantitate the effect of the nonlinear kick from the the crab cavity, and determine the frequency of the crab cavities for both Nominal and Ultimate design.

The luminosity degradation parameter  $H = L_{head-on} / L_{crab-crossing}$  characterizes the integral effect of the nonlinear crab cavity. An ideal crab cavity will recover the luminosity from the crossing angle and make this parameter 1. We set the criteria that the degradation is not larger than the value of the LHC High Luminosity upgrade.

We propose to use two frequencies, a fundamental frequency 140.7 MHz and its 3<sup>rd</sup> harmonic frequency 422.2MHz. The voltage ratio of the harmonic cavity is determined by minimizing the luminosity degradation factor. We found that the optimum ratio is 0.16. The detailed parameter is listed in Table 2-24. The 422.2 MHz cavity will also serve as the crab cavity of the electron beam.

eRHIC crab cavity design will be based on the same geometry as the cavity for the LHC high-lumi upgrade, with necessary scaling and optimizations accordingly. The LHC Accelerator Research Program in the Collider Accelerator Department of Brookhaven National Lab has delivered a successful compact crab cavity design for the Hi-Lumi upgrade of LHC, shown in the left of Figure 2-88. This 400 MHz crab cavity is based on a double quarter wave (DQW) geometry with push-pull tuning system, three higher order mode couplers, and a 50 kW fundamental power coupler, as shown in the right of Figure 2-88. The Proof of Principle DQW crab cavity has reached 4.6 MV in deflecting voltage at 2 K cold test. The compactness of the DQW crab cavity ensures the size in all three dimensions to keep within an economical value even at low frequencies, such as the 140.7 MHz for the fundamental crab cavity for ion/proton. The high frequency cavities for electron crabbing and 3rd harmonic correction for ion/proton should be very close to the LHC cavity design, which maximized the reuse of the experience gained previously.

**Table 2-24: Crab cavity parameters.**

Parameters	Nominal Design		Ultimate Design	
	Electron	Ion (p)	Electron	Ion (p)
Crossing angle (Full, mrad)	10		10	
Beam energy (GeV)	20	250	20	250
Beta function at IP ( $\beta^*$ , cm)	12.5	12.5	5	5
Transverse beam size at IP ( $\mu\text{m}$ )	15.3	15.3	7.1	7.1
Bunch length (cm)	0.3	15	0.3	5

Piwinski angle (rad)	0.98	49.0	2.14	35.7
Beta function at crab cavity	115	~1000	270	2500
Frequency of fundamental crab cavity (MHz)	422.2	140.7	422.2	140.7
Voltage of fundamental crab cavity (MV)	3	~44	3	38
Frequency of 3 <sup>rd</sup> harmonic crab cavity (MHz)	N/A	422.2	N/A	N/A
Voltage of 3 <sup>rd</sup> harmonic crab cavity (MV)	N/A	~-2	N/A	N/A

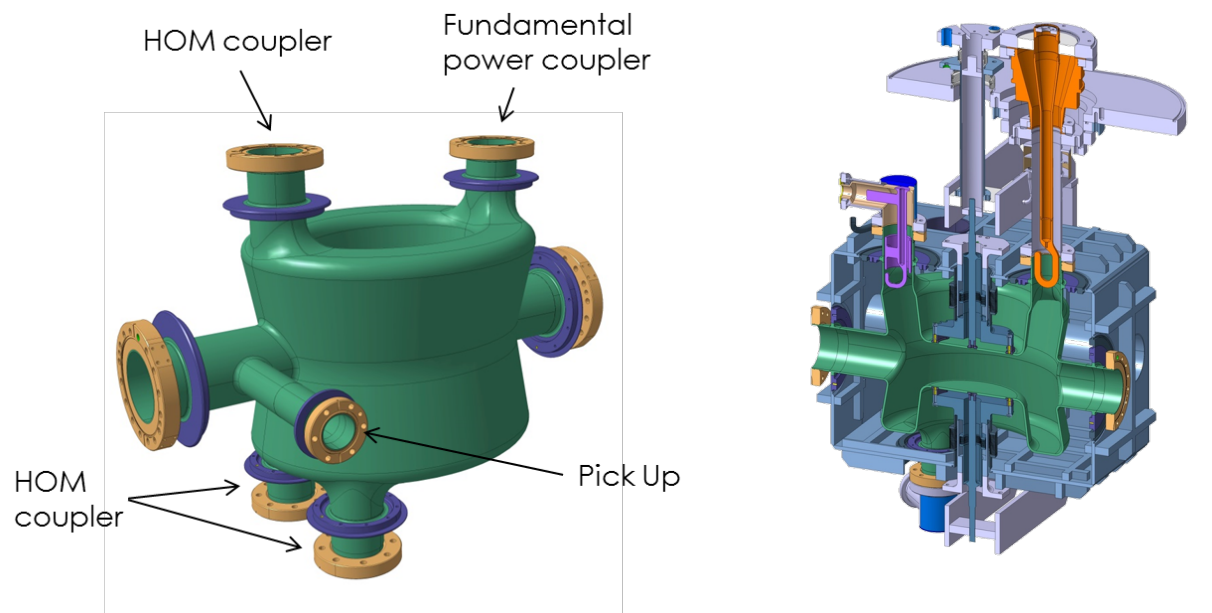


**Figure 2-88:** Left: DQW crab cavity for Hi-Lumi LHC; right: Cross-section view of the DQW crab cavity in helium vessel with HOM coupler (purple), 50kW FPC (orange), and tuner

End of the chapter.

## ***Bibliography:***

- [1] B. Dunham, et al., "First Test of the Cornell University ERL Injector", LINAC08, WE104, Victoria, BC, Canada, (2008).
- [2] K. R. Symon, D.W. Kerst, L.W. Jones, L. J. Laslett, and K. M. Terwilliger, Phys. Rev., 103, 1837 (1956).
- [3] T. Ohkawa, University of Tokyo, Tokyo, Japan, FFAG structure suggested earlier at a Symposium on Nuclear Physics of the Physical Society of Japan in 1953 (private communication).
- [4] A. Kolomensky et al., Zh. Eksp. Teor. Fiz. 33, 298(1975).
- [5] D. Trbojevic, E. D. Courant, A.A. Garren. 1999-Presented at the High Energy Muon Colliders workshop in Montauk HEMC, published by AIP, Woodbury, New York, USA (2000).
- [6] C. Johnstone, et al., "Fixed Field Circular Accelerator Designs", PAC'99, New York, P. 3068.
- [7] D. Trbojevic and E. Courant, Proc. of the European Particle Accelerator Conference, 1994, p. 1000.
- [8] ["Acceleration in the linear non-scaling fixed-field alternating-gradient accelerator EMMA"](#), Machida, S. et al. Nature Phys. 8 (2012) 243-247 FERMILAB-PUB-12-308-AD.
- [9] Dejan Trbojevic, RLA with FFAG arcs, Muon Collider Design Workshop, Dec 1-3, 2009. Racetrack NS-FFAG with Halbach permanent magnets.
- [10] James Volk, "Permanent Magnet Work at Fermilab 1995 to present", Fermilab Internal note.
- [11] M. Borland, "elegant: A Flexible SDDS-Compliant Code for Accelerator Simulation," Advanced Photon Source LS-287, September 2000.
- [12] Y. Wang and M. Borland, "Pelegant: A Parallel Accelerator Simulation Code for Electron Generation and Tracking", Proceedings of the 12th Advanced Accelerator Concepts Workshop, AIP Conf. Proc. 877, 241 (2006).
- [13] F. Meot, The ray-tracing code Zgoubi - Status, NIM A 767 (2014) 112125; F. Meot, Zgoubi users' guide, <http://www.osti.gov/scitech/biblio/1062013>.
- [14] G.H. Hoffstaetter and I.V. Bazarov, Phys. Rev. ST-AB 7, 054401, (2004).
- [15] E. Pozdeyev, Phys. Rev. ST-AB 8, 054401, (2005).
- [16] Y. Hao, and V. Ptitsyn, Phys. Rev. ST-AB, 13, 071003 (2010).
- [17] R. Li, B.C. Yunn, V. Lebedev, J.J. Bisognano, "Analysis of Beam-beam Kink Instability in a Linac-Ring Electron-Ion Collider", PAC'01, Chicago, IL, (2001).
- [18] Y. Hao, V. N. Litvinenko, and V. Ptitsyn. Phys. Rev. ST-AB, 16, 101001 (2013).
- [19] Y. Hao, M. Blaskiewicz, V. N. Litvinenko, and V. Ptitsyn., "Kink Instability Suppression With Stochastic Cooling Pickup And Kicker", IPAC'12, New Orleans, Louisiana, USA, (2012).
- [20] D.P. Barber, et al., Phys. Lett. 343A 436 (1995).
- [21] T. Zwart, et al., Proceedings of PAC, Chicago, p.3597 (2001).
- [22] V. Parkhomchuk and I. Ben-Zvi, Electron Cooling for RHIC. C-A/AP/47 April 2001.
- [23] Wilson, M. N., Rutherford Appleton Laboratory Report, RHEL/M151, 1968.
- [24] M. A. Green et al. Progress on the Superconducting Magnets for the MICE Cooling Channel, Journal of Physics Conf. Series (SuST) 234, 032017 (2010).
- [25] M. Blaskiewicz, J.M. Brennan, F. Severino, Physical Review Letters **100**, 174802 (2008).
- [26] A.V. Fedotov, I. Ben-Zvi, D.L. Bruhwiler, V.N. Litvinenko and A.O. Sidorin, New Journal of Physics **8**, 283, (2002).
- [27] A. Mikhailichenko, M. Zolotarev, Physical Review Letters **71**, p.4146 (1993).
- [28] V.N. Litvinenko, Y.S. Derbenev, Physical Review Letters **102**, 114801 (2009).
- [29] D. Ratner, Physical Review Letters **111**, 084802 (2013).
- [30] V.N. Litvinenko, "Advances in CeC", COOL'13 workshop, Murren, Switzerland, (2013).
- [31] M. Blaskiewicz, J.M. Brennan, K. Mernick, in the 6rd International Particle Accelerator Conference – IPAC'16, Richmond, VA, USA, 2015, pp. 746.

---

<http://accelconf.web.cern.ch/accelconf/IPAC2012/papers/tuppp093.pdf>

- [32] G. Wang, and M. Blaskiewicz, in *2007 Particle Accelerator Conference – PAC’07* (Albuquerque, New Mexico, USA, 2007), p. 3726.
- [33] S. Peggs, and W. Mackay, in *RHIC/AP/36*, (1994).
- [34] Covered in many textbooks, e.g. A.W. Chao, “Physics of Collective Beam Instabilities in High Energy accelerators”, John Wiley & sons Inc. N. Y. (1993).
- [35] R.P. Reed and A.F. Clark, Editors “Materials at Low Temperatures” American Society of Materials (1983).
- [36] N.J. Simon, E.S. Drexler, and R.P. Reed, “Properties of Copper and Copper Alloys at Low Temperatures”, NIST monograph 177, Government Printing Office (1992).
- [37] U. Iriso and S. Peggs, Phys. Rev. ST Accel. Beams **8**, 024403 (2005).
- [38] U. Iriso and S. Peggs, Phys. Rev. ST Accel. Beams **9**, 071002 (2006).
- [39] W. Fischer M. Blaskiewicz, J. M. Brennan, H. Huang, H.-C. Hseuh, V. Ptitsyn, T. Roser, P. Thieberger, D. Trbojevic, J. Wei, S. Y. Zhang, and U. Iriso, Phys. Rev. ST Accel. Beams **11**, 041002 (2008).
- [40] E.L. Garwin, F.K. King, R.E. Kirby, and O. Aita, J. Appl. Phys. **61**, 1145 (1987).
- [41] P. Chiggiato, "*Surface treatments and coatings for the mitigation of electron clouds*", presentation to the 23rd LHC Machine Advisory Committee Meeting, 16 June 2008.
- [42] C. Yin Vallgren, G. Arduini, J. Bauche, S. Calatroni, P. Chiggiato, K. Cornelis, P. Costa Pinto, B. Henrist, E. Métral, H. Neupert, and G. Rumolo, Phys. Rev. ST Accel. Beams **14**, 071001 (2011).
- [43] A. Kuzucan, H. Neupert, M. Taborrelli, and H. Stori, J. Vac. Sci. Technol. A **30**, 051401 (2012). Mauro Taborrelli, private communication 2012; M. Furman, private communication 2012.
- [44] C. Benvenuti, P. Chiggiato, F. Cicoira, and Y. L’Aminot, J. Vac. Sci. Technol. A **16**, 148 (1998).
- [45] John L. Vossen and Werner Kern Editors, “Thin Film Processes” Academic Press, New York (1978).
- [46] A. Herscovitch, M. Blaskiewicz, J. M. Brennan, A. Custer, A. Dingus, M. Erickson, W. Fischer, N. Jamshidi, R. Laping, C. J. Liaw, W. Meng, H.J. Poole, R. Todd, “Plasma sputtering robotic device for in-situ thick coatings of long, small diameter vacuum tubes,” Physics of Plasmas **22**, 057101 (2015).
- [47] A. Herscovitch, M. Blaskiewicz, J.M. Brennan, W. Fischer, C-J Liaw, W. Meng, R. Todd. A. Custer, A. Dingus, M. Erickson, N. Jamshidi, and H. J. Poole, “Novel techniques and devices for in-situ film coatings of long, small diameter tubes or elliptical and other surface contours”, J. Vac. Sci. Technol. B **33**, 052601 (2015).
- [48] V.N. Litvinenko and G. Wang, “On Compensating Tune Spread Induced by Space Charge in Bunched Beams”, Phys. Rev. ST-AB **17**, 114401, (2014).
- [49] H. Huang, et al., Phys. Rev. Lett. **99**, 154801 (2007)
- [50] H. Huang, et al., Phys. Rev. STAB. **17**, 081001 (2014).
- [51] M. Bai, et al., Phys. Rev. Lett. **96**, 174801 (2006).
- [52] E. Courant and R. Ruth, BNL report, BNL-51270 (1980).
- [53] F. Meot, et al., Proc. of IPAC12, 181 (2012).
- [54] A. Zelenski, H. Huang, T. Roser, Proc. of PSTP 2013, 056 (2013).
- [55] S.Fartoukh, “An Acromatic Telescope Squeezing Scheme for the LHC Upgrade”, IPAC’11, WEPC037, (2011).